VOLUME 2 NUMBER 1 2015 ISSN 2409-6121

Physical Sciences and Technology

National Nano Laboratory of Open Type
Research Institute of Experimental and Theoretical Physics

Physical Sciences and Technology is publishing two numbers in a year by al-Farabi Kazakh National University, al-Farabi ave., 71, 050040, Almaty, the Republic of Kazakhstan
website: http://phst.kaznu.kz/

Any inquiry for subscriptions should be send to:
Abdiadil Askaruly, al-Farabi Kazakh National University
al-Farabi ave., 71, 050040, Almaty, the Republic of Kazakhstan
e-mail: Abdiadil.Askaruly@kaznu.kz

SCOPE AND AIM

Physical Sciences and Technology provides an original paperback for the publication of peer-reviewed research and review articles in all fields of Physics and related Technology. The topics, included in the scope, especially emphasize understanding of the physics underlying modern technology.

Subject areas may include, but are not limited to the following fields: Astronomy and Space Research, Theoretical Physics and Astrophysics, Plasma Physics and Related Technology, Chemical Physics and Radio Physics, Condensed Matter Physics and Related Technology, Thermal physics and Related Technology, Nuclear Physics and Related Technology, Nanomaterials and Nanotechnology, Applied Atomic and Molecular Physics, Material Sciences and Related Technology, Electronics and Related Technology, Instrumentation, Photonics and Quantum Electronics, Signal processing.

The Journal is issued under the auspices of the National Nano Laboratory of Open Type and the Research Institute of Experimental and Theoretical Physics and is published two times a year by the "Kazakh University" Publishing House. The International Editorial Board of the Journal consists of leading researchers from different countries of the world. The Journal is wide open for contributions that both lie at the far frontiers of contemporary physics and are particularly aimed at applications of the scientific principles of physics to modern technological problems.

UDC 621.382.822

Investigation of the physical properties of nanoscale porous silicon films

S.M. Manakov[1], Ye. Sagidolda[1,2,*]
[1]Al-Farabi Kazakh National University, NNLOT, al-Farabi 71, 050040 Almaty, Kazakhstan,
[2]Al-Farabi Kazakh National University, Laboratory of Engineering, al-Farabi 71, 050040 Almaty, Kazakhstan
[*]e-mail: erulan.sagidolda@kaznu.kz

The structure and physical properties of porous silicon obtained by electrochemical etching of monocrystalline silicon with n-type conductivity in a mixture of hydrofluoric acid and ethyl alcohol were investigated. Experimental layers were formed by varying the etching parameters. Samples were studied using the methods of atomic force microscopy (AFM),scanning electron microscopy (SEM), Raman spectroscopy (RS) and photoluminescence spectrometry (PL). It was found that the PL intensity increased with increasing etching time.It was demonstrated that by varying of technological parameters and conditions of the etching process we can control the size of nanocrystals and manufacture nanostructuresof porous silicon film with improved properties.

Key words: porous silicon, electrochemical etching, photoluminescence, nanocrystals.
PACS numbers: 82.45.Vp, 78.55.Mb, 71.24.+q.

1 Introduction

Porous silicon (PS) attracted the attention of researchers for the most part due to its luminescent properties [1]. In addition, the extensive study of various properties of the PS has opened prospects for its numerous alternative applications in areas such as solar cells, biotechnology, sensors [2,3]. Well-developed method of electrochemical etching of silicon allows controllable vary parameters of porous layer in order to optimize its physical properties. The surface morphology of the PS film and its structural and optical properties depend on the such parameters like the concentration and type of impurity in the initial silicon substrate, the magnitude of the anodizing current and the duration of etching, the composition and temperature of the electrolyte, and other factors [4].

Using of Raman spectroscopy allows us to estimate the characteristic dimensions in PS nanocrystals and their dependence on technological regimes for producing PS with different properties. More information about the morphology of the surface of semiconductor films can be obtained using the method of atomic force microscopy [5,6].

This paper presents the results of studies of the structure, morphology and photoluminescence properties of porous silicon films grown on n-type crystalline Si substrates for different values of the duration and magnitude of the anodizing current.

2 Experimental Details

N-type silicon wafers with a phosphorus concentration 10^{18} cm^{-3} and the crystallographic orientation (100) were used for manufacturing PS. Before anodization a silicon wafers were placed to trichloroethylene for degreasing, were rinsed in deionized water, then after treatment in a solution of H_2SO_4: H_2O_2 (4: 1) at temperature 90^0C for 10 minutes silicon wafers were etched in a mixture of HF and H_2O (1: 50) for 10 seconds and thoroughly washed in deionized water. Etching occurred in the electrolyte containing hydrofluoric acid and ethyl alcohol in a ratio of 1: 1.5.

To determine the differences in the structure and properties of PS three groups of samples were prepared at different anodizing current densities and with different anodization time: 1 – J = 1 mA/cm^2, t = 20 min; 2 – J = 15 mA/cm^2, t = 2 min and 3 – J = 25 mA/cm^2, t = 1 min. The power supply voltage for all groups of samples remained unchanged at 10 V. These modes provide approximately the same ~1 micron thickness of PS. Measurements of the structure and properties of the PS samples were performed after 10 days storage in the air.

3 Results and discussion

The morphology of the films was studied using atomic force microscope NT-MDT NtegraTherma.

The study of PS surface morphology using the method of AFM has revealed its dependence on etching modes. Figure 1 shows the 3D image (1a, 2a, 3a) and the 2D image (1c, 2c, 3c) surface of PS films grown under the above conditions. Profile section along the center line shown in Fig. 1b, 2b, 3b for the three groups of samples.

Figure 1 shows that the prolonged etching under low current density of 1 mA/cm^2 (Fig. 1b) results in developed surface having a smaller size of structural heterogeneities than typical structures with less etching time, but with large current densities of 15 mA/cm^2 and 25 mA/cm^2 (Fig. 2b and 3b, respectively).

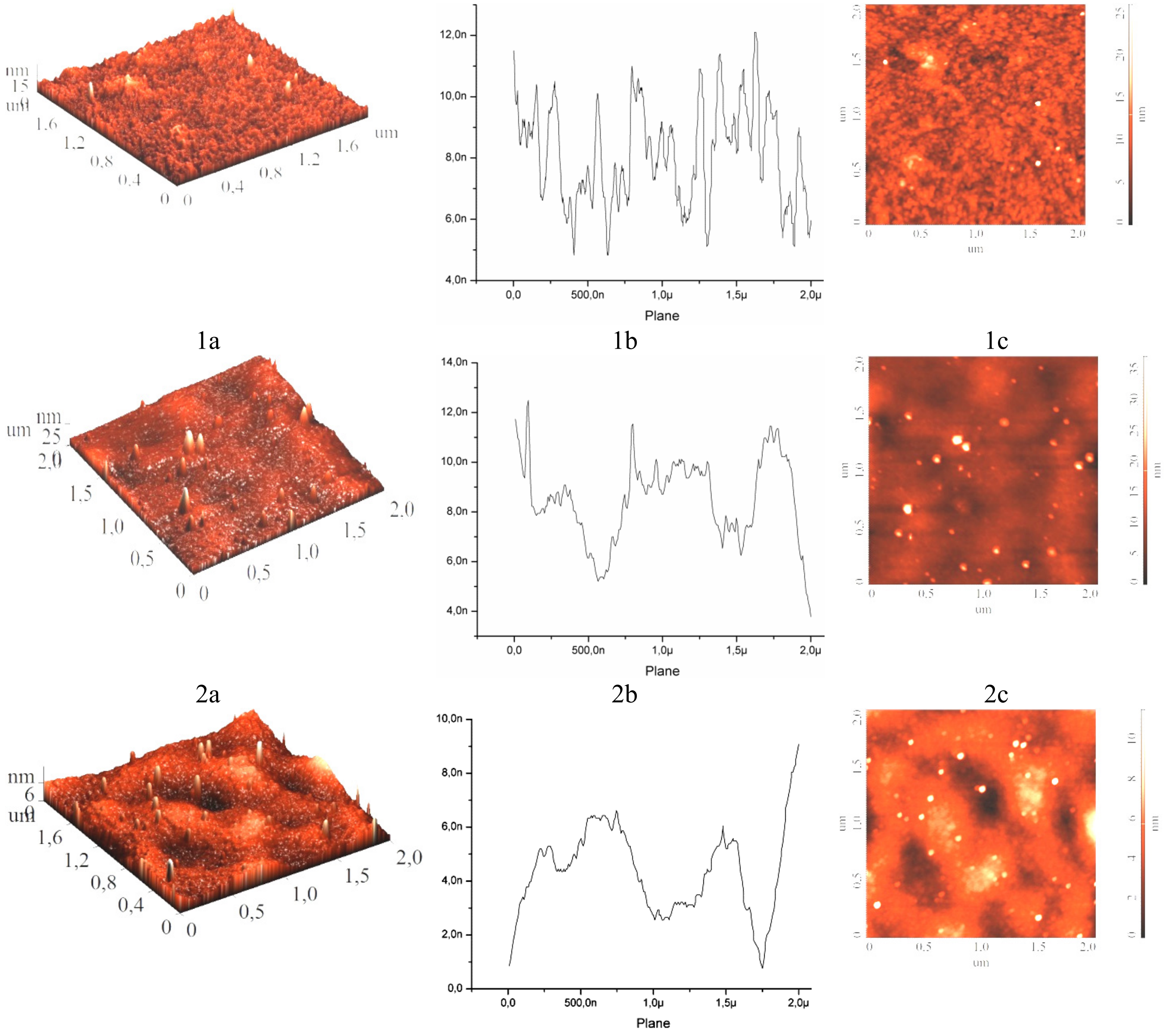

1a 1b 1c

2a 2b 2c

3a 3b 3c

Figure 1 – AFM image of PS samples grown under different conditions for the three groups of samples:
1 – J = 1 mA/cm^2, t = 20 min.;
2 – J = 15 mA/cm^2, t = 2 min.;
3 – J = 25 mA/cm^2, t = 1 min.

For the mathematical characterization of the surface roughness we used the root-mean-square roughness S_q, defined as:

$$S_q = \sqrt{\frac{\sum_{i=1}^{N}\left(H_i - \hat{H}\right)^2}{N}}, \qquad (1)$$

where N is the number of measured points, $\hat{H}$ is the average height (zero level), $(H_i - \hat{H})$ is the relative height *of i* point.

The measurement results showed that the mean square roughness $S_q$for the sample groups 1,2 and 3 were 2.96 nm, 1.85 nm, and 1.63 nm, respectively.

Using image processing module of AFM height distribution functions for the investigated films were calculated for surface area of 2x2 μm^2 (Fig. 2).

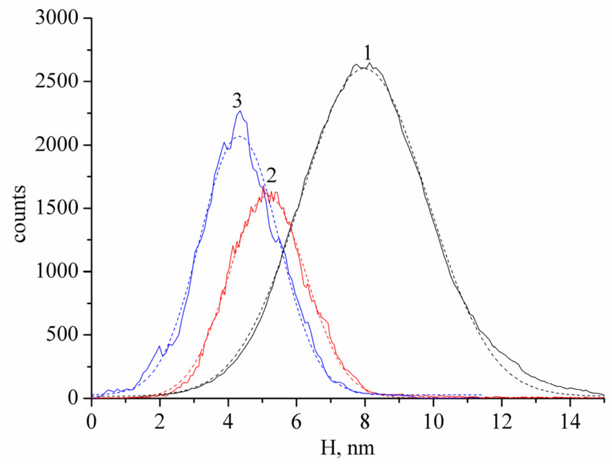

Figure 2 – Height distribution function of PS films for samples 1, 2, 3. Dashed lines are results of approximation with Gaussian functions

The distribution function for PS layers is well approximated by a Gaussian function centered at H_1 = 8.4 nm, H_2=4.8 nm, H_3 = 4.2 nm for samples 1, 2, 3, respectively. For sample 3 with the shortest etching time characteristic size of heterogeneity was minimal.

AFM images of the PS surface demonstrated that with increasing current density film surface becomes more smooth as compared with the PS produced at a current J = 1 mA/cm^2. Similarly to [7] the calibration experiments of porosity determination showed that when current density increases from J = 1 mA/cm^2 to J = 25 mA/cm^{2}porosity decreases from 50% to 30%, and typical dimensions are reduced from 8.4 nm to 4.2 nm.

Using an electron microscope FEI Quanta 200 FEG SEM-images of PS surface and cross-sectional samples were obtained. Figure 3 shows a cross-sectional view (a) and the surface of a PS (b), grown at a low current density. As seen in Fig. 3 the PS layers have sponge-like structure. The surface concentration of pores is uniform, and the sizes of pores were ranging from 7 nm to 9 nm. Samples obtained at high current densities characterized by a lower concentration of pores on the surface.

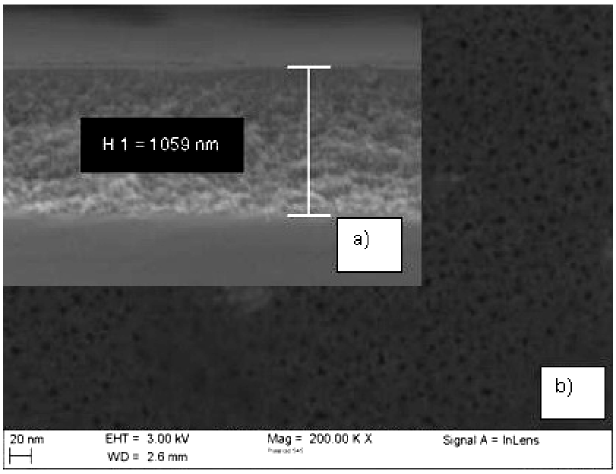

Figure 3 – SEM-images of cleaved facet (a) and surface (b) of PS sample grown at J = 1 mA/cm^2 for 20 min

Photoluminescence (PL) in PS is the evidence of PS band gap broadening due to the presence of nanoscale silicon clusters formed near the walls of the pores. Photoluminescence spectra were measured at room temperature using a spectrometer NT-MDT Ntegra Spectra, the incident laser power was about 25 mW at a wavelength of 477 nm. The diameter of the laser spot on the sample was about 2 microns.

Figure 4 shows the PL spectra for the three types of PS layers. For all samples, the shape of the PL spectrum is close to a Gaussian curve, maxima of the curves are in the range 650-680 nm, which corresponds to photon energy of 1.82 – 1.91 eV.

These peaks correspond to radiation in the red region of the spectrum and are explained on the basis of quantum confinement model [8].

The PL intensity of the peaks correlated with the duration of the etching, the maximum intensity was observed in the samples of group 1, which can be explained more porous, more advanced surface morphology and an increase in the concentration of nanocrystals.

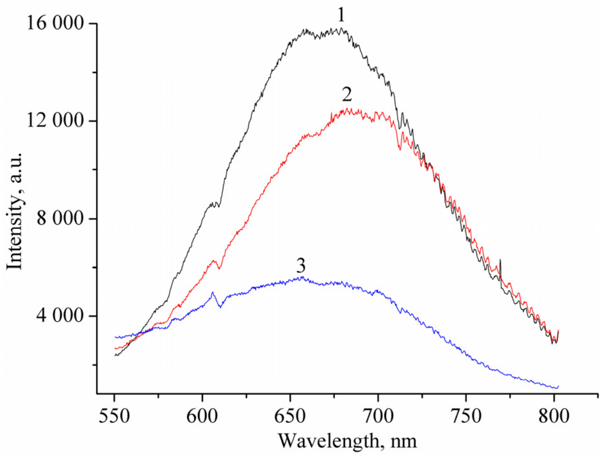

Figure 4 – Photoluminescence spectra of thePor-Si samples grown at different conditions:
1 – J = 1 mA/cm^2, t = 20 min.;
2 – J = 15 mA/cm^2, t = 2 min.;
3 – J = 25 mA/cm^2, t = 1 min

Reflectance spectra for all three groups of samples were recorded on a spectrophotometer Shimadzu UV-3600 and are presented in Figure 5.

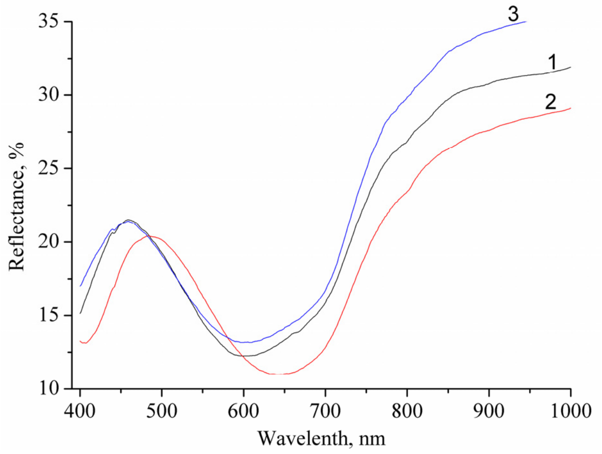

Figure 5 – Wavelength dependence of reflectance ofPS samples grown at different conditions:
1 – J = 1 mA/cm^2, t = 20 min .;
2 – J = 15 mA/cm^2, t = 2 min .;
3 – J = 25 mA/cm^2, t = 1 min

Position of the interference maxima and minima are in good agreement for all samples, indicating that their thicknesses are equal.

The Raman spectra of PS films is a good diagnostic tool for the study of structural phases and allows to evaluate the characteristic dimensions of the nanocrystals. The Raman peak from pure single-crystalline silicon was at 520 cm-1, and its shape was nearly Lorentz an. This peak is associated with longitudinal optical (LO) modes [7]. For porous silicon, the broadening and downshift of Raman peak towards lower energy are connected with the presence of nanoscale features of the crystalline structures. The Raman scattering experiments are performed in the range of 400-600 cm^{-1} at room temperature using the spectrometer NT-MDT Ntegra Spectra and are shown in Figure 6. The peak at 514-518 cm^{-1} (instead of 520 cm^{-1}) appears after etching the monocrystalline silicon and connected with nanoporous structure. Region 465-485 cm^{-1} is associated with the transverse optical (TO)modes in the amorphous silicon [9].

For all samples of the PSshift in the position of the peaks in the Raman spectra to lower energy was observed. The greatest shift to 514 cm^{-1} was observed for the PS layers with etching time of 20 minutes, for the samples with etching time of 1-2 minutes the peak shifts to 518 cm^{-1}.

Information on the average size of nanocrystallites in the PS can be obtained from the Cardona equation [10]

$$d = 2\pi\sqrt{\frac{B}{\Delta\omega}}\ \text{(nm)}, \tag{2}$$

where B = 2.24 cm^{-1} for silicon, $\Delta\omega$ – the peak shift of Raman scattering in the PS relative to the peak of crystalline silicon. In accordance with (2) the PS crystallite sizes of the samples decreased from 6.6 nm to 3.8 nm with increasing etching duration of from 1 minute to 20 minutes.

Figure 6 shows that a decrease in the size of nanocrystals is accompanied with crystal imperfection, an expansion of the spectral line, which becomes more asymmetric and its maximum shifts to the lower energy. The broadening of the Raman spectra with increasing etching time indicates the violation of the crystal structure of silicon source, the appearance of the amorphous phase and nanocrystalline clusters on the surface of the pores.

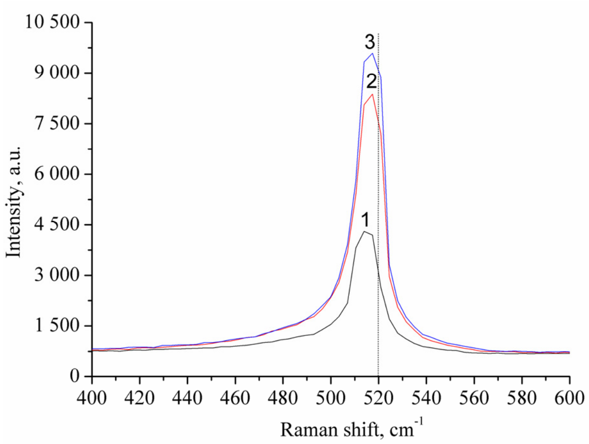

Figure 6 – Raman spectra of Por-Si samples grown at different conditions:
1 – J = 1 mA/cm^2, t = 20 min .;
2 – J = 15 mA/cm^2, t = 2 min .;
3 – J = 25 mA/cm^2, t = 1 min

4 Conclusions

In this work the dependence of structural and photoluminescent properties of PS layers on technological parameters of its fabrication were studied. Analysis of PS layers with the same thickness showed that increasing the etching time leads to a more advanced surface morphology and increased porosity. The films produced during the etching 1-2 minutes characterized by mean square roughness S_q = 1.63-1.85 nm and for specimen obtained within 20 minutes S_q = 2.96 nm; the characteristic size of the heterogeneity on the surface of the PS films increased from 4.2 nm to 8.4 nm. Scanning electron microscopy confirmed that the concentration distribution of pores was uniformly over the surface, and pore size ranges from 7 nm to 9 nm.

Applying Raman measurements, crystallite size was found to be 3.8 – 6.6nm; with increasing etching time from 1 minute to 20 minutes crystallite size was increased. It was found that the photoluminescence intensity is higher in samples with crystallite size of 3.8 nm, and the maximum was shifted to shorter wavelengths and was localized at 650 nm.

Acknowledgements

The authors express immense thanks to staff and management of National Nanotechnology Open Laboratory of Kazakhstan for assistance in the measurements. This work was supported by the Ministry of Education and Science Republic of Kazakhstan (contract no. 1569/GF3).

References

[1] M.V. Wolkin, J. Jorne, M. Fauchet, G. Allan, C Delerue. Electronic States and Luminescence in Porous Silicon Quantum Dots // Phys. Rev. Letters. – 1999. – Vol. 82. – P. 197-200.

[2] R.S. Dubey, D.K. Gautam. Synthesis and Characterization of Nanocrystalline Porous Silicon Layer for Solar Cells Applications // Journal of Optoelectronics and Biomedical Materials. – 2009. – Vol.1. – P. 8-14.

[3] E.A. Tutov, A.Yu. Andryukov, S.V. Ryabtsev. Non-equilibrium processes in capacitive sensors based on porous silicon // Pis'ma v ZhTF. – 2000. –Vol. 26. – P. 53-58 (in Russian).

[4] M. Das, D. Sarkar. Structural and Optical Properties of n-type Porous Silicon Fabricated in Dark // Indian Journal of Pure & Applied Physics. – 2013. – Vol. 51. – P.724-727.

[5] N. Di Nardo. John. Nanoscale characterization of surfaces and interfaces. – New York: John Wiley & Sons, 1994. – P. 173.

[6] S.M. Manakov, T.I. Taurbayev. Morphology and Structural Properties of a-Si:H and a-SiC:H Films Controlled in Nanoscale // J. Nanoelectron. Optoelectron. – 2012. – Vol.7. – P. 619-622.

[7] A. Halimaoui. Properties of Porous Silicon / edited by L.T. Canham. – London: IEE INSPEC, The Institution of Electrical Engineers, 1997. – P. 12.

[8] C. Delerue, G. Allan, M. Lannoo. Theoretical Aspects of the Luminescence of Porous Silicon // Phys. Rev. B. – 1993.– Vol. 15. – P. 11024-11036.

[9] B. Bulakh, N. Korsunska, L. Khomenkova, T. Stara, Ye. Venger, T. Krystab, A Kryvko. Structural and Luminescent Characteristics of Macroporous Silicon // J. Mater. Sci. Mater. Electron. – 2009. – Vol. 20. – P. 226-229.

[10] Z.C. Feng, A.T.S. Wee. Multi-technique study of porous silicon membranes by Raman scattering, FTIR, XPS, ARS and SIMS/ Porous Silicon: eds. Z.C. Feng, R. Tsu. Singapore: World Scientific, 1994. – P. 175-192.

UDC 537.523/.527;533.9.08;

Investigation of electrical and optical properties of dielectric barrier discharge

Y.A. Ussenov[1,2], T.S. Ramazanov[1], M.T. Gabdullin[1,*],
M.K. Dosbolayev[1], T.T. Daniyarov[1]

[1]Al-Farabi Kazakh National University, IETP, al-Farabi 71, 050040 Almaty, Kazakhstan
[2]Institute of applied sciences and information technologies, 40 Shashkin ast., Almaty 050040, Kazakhstan
[*]e-mail: Maratbek.Gabdulin@kaznu.kz

In this paper the results of optical and electrical characteristics of dielectric barrier discharge are presented where used “plane to plane” and “pin to plane” electrode configurations. The dynamic current-voltage characteristics of discharge at different electrode configurations were investigated. The plasma spectrum of air of dielectric barrier discharge was obtained by optical emission spectroscopy method. The results of measurement of the discharge current showed that the barrier discharge generated in the streamer mode, and the used pin electrode reduces the streamer channels and micro discharges. The plasma spectrum of air showed active components and radicals which can be used for treatment of living tissues and materials.

Key words: dielectric barrier discharge, dynamic current-voltage characteristics,plasma spectrum
PACS numbers: 52.80.Tn, 52.25.-b

1 Introduction

The dielectric barrier discharge (DBD) is a discharge that is producedat atmospheric pressure between two metal electrodes, one of which is coated with a dielectric [1]. In recent decades, low temperature barrier discharge plasma is widely used for treatment of living tissues and destroy cancer cells [2, 3], for sterilizing instruments, packaging and seeds of various crops [4], to improve the surface properties of polymeric materials and textiles, as well as for deposition of various thin-films [5]. An important role in the generation of plasma at atmospheric pressure in dielectric barrier discharge plays a form of dielectric and metal electrodes. There are different geometric configurations of electrodes as "plane-to-plane", "pin-to-plane", "surface electrodes (surface DBD)", "co-axial arrangement of the electrodes," and etc. The electrode system determines the basic electrical, optical and energetic properties of the barrier discharge. In work [6] the AC corona discharge with barrier electrode was investigated experimentally. One of the electrodes had a flat geometry, which was covered with an insulator whereas the second electrode had the shape of the tip. Experiments were carried out at atmospheric pressure in air, helium, argon and nitrogen. The results showed that with pin like electrodes the breakdown voltage decreases in comparison with the plane to plane barrier discharge, but the current is considerably increase. Different modes of discharge at the pin-to-plane geometry of the electrodes were investigated in [7]. Various modes of discharge were obtained at an applied voltage of 3 kV and 6 kV and at the positive and negative half-cycles. It was shown that micro-glow discharges have a hierarchical structure like in a low-pressure glow discharge. In work [8] the characteristics of modified dielectric barrier discharge (i.e., pin-to-plane electrodes) in helium was studied in dependence on the applied AC voltage, the distance between two electrodes and the type of pin electrodes. The power consumption of the discharge was investigated at different densities of high voltage pin electrodes. In [9] the static current-voltage characteristics of the barrier discharge at pin-to-plane electrode configuration were studied and had been shown that the discharge current decreases with increasing the distance between the electrodes. In [10], the two-dimensional model of the barrier discharge in nitrogen for pin–to–plane geometry is made up based on the continuity equation and the Poisson’s equation for the electric field. The results of numerical analysis shown that the characteristics of the discharge determine by the distribution of variable electric field, which is more near from the pin electrode due to its curvature. For dissociation of carbon dioxide molecules the different geometry of electrodes of the barrier discharge reactor was used by authors in [11]. Application of pin-to-plane electrodes showed significant energy efficiency in comparison with the plane-to-plane electrodes.

2 Experimental setup

During development of the experimental setup based on a dielectric barrier discharge were collected two types of electrode system configurations. The first electrode system consists of two planar electrodes; one of them is coated with a dielectric material. In the second configuration, the ground electrode is replaced by a metal rod with a sharp tip, which gives the corona effect. The Figure 1 shows the general scheme of the experimental setup and the concept of a barrier discharge electrode systems.

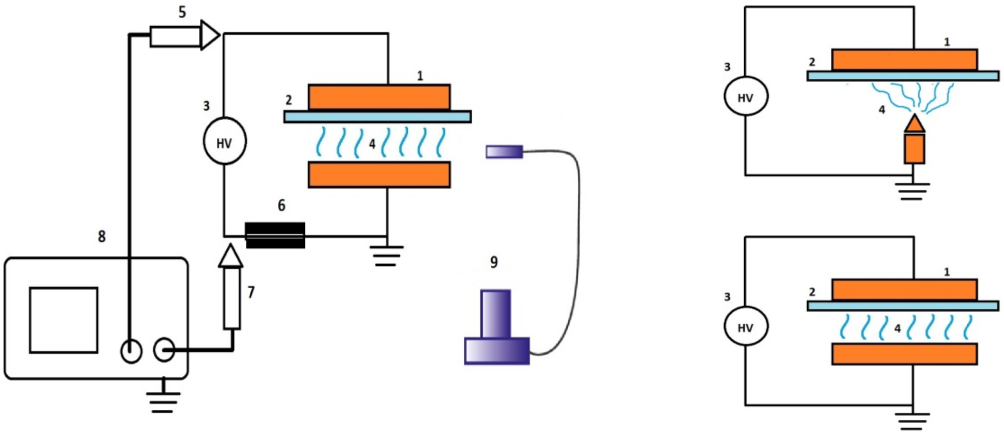

Figure 1 – The experimental setup and configuration of the electrodes of DBD

The copper cylinder (1) with a diameter *d* = 45 mm, and the thickness *l* = 4,5 mm used as planar electrodes. On a surface of a planar electrode the quartz glass (2) with a diameter *d* = 75 mm, thickness *l* =6 mm and a dielectric constant ε = 3,5 was disposed. In the case of the pin-to-plane configuration the sharp metal rod with length *l* = 28 mm and diameter *d* = 8 mm was used as ground electrode. In all experiments the interelectrode distance (4) was 2 mm. For generation of plasma we used the high voltage power supply (3), which generated the high voltage sinusoidal signal with amplitude 15 kV and frequency 20 kHz from. The applied voltage is measured using a high-voltage probe (5) Tektronix P6015 and a digital oscilloscope LeCroy (8). The current is detected by low-voltage LeCroy probe (7) and measuring resistor with resistance 100 Ohms (6). The optical characteristics were measured by optical emission spectrometer Solar Systems. The spectrometer consists of an optical system, an optical fiber for transmitting radiation from the spectrometer itself. Further, the resulting signal is processed by a personal computer. For visual observation of the discharge CCD camera was used with 25 frames / second.

3 Results and discussion

After applying a high-voltage sinusoidal signal, the barrier discharge at the filamentary mode formed between the electrodes on the flat dielectric surface and the metal. As shown in Figure 2, discharge consists of a set of microchannels (or streamers), which carries the discharge current.

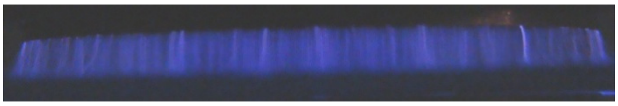

Figure 2 – DBD in operation at the "plane-to- plane" electrodes

Typically, in the case when one of the metal electrodes covered with a dielectric the width of microdischarge on the dielectric barrier surface were greater than on the surface on the metal electrode. Figure 3 presents the dynamic current-voltage characteristics of the discharge in a constant voltage 15 kV and at different electrode geometry. The left figure corresponds to the geometry of the "plane-to-plane" electrodes and the right corresponds to the geometry of the "pin-to-plane” electrodes.

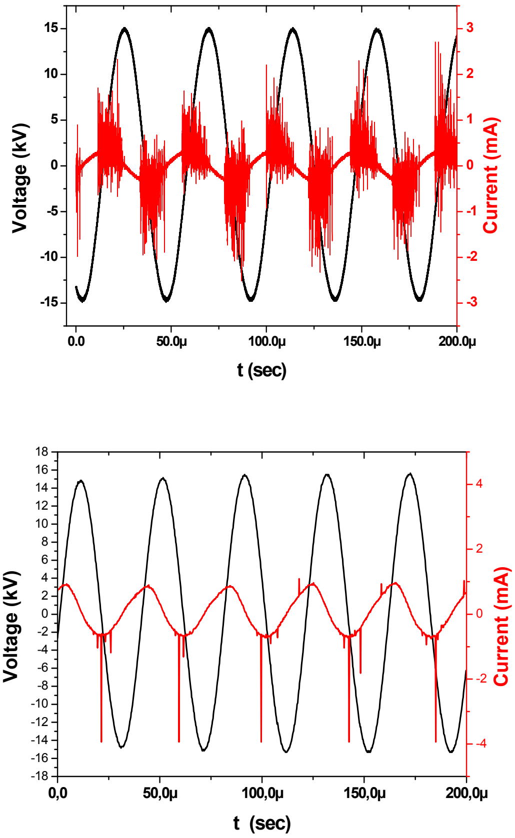

Figure 3 – The dynamic current-voltage characteristics of dielectric barrier discharge: the top –"plane-to-plane", the bottom – "pin-to-plane"

From the current waveform, it can be seen that in the case of “plane-to-plane” electrode geometry set of peaks observed at the start of each half-cycle of applied voltage. These peaks correspond to a plurality of multi microdischarge (streamer) in the discharge gap. In the case when a ground plane was replaced by a sharp metal electrode on the current waveform only single pulses can be seen. They correspond to a single streamer channel. It should be noted that the current through this channel is relatively high about 4 mA, whereas in the case of flat electrodesand the plurality of microdischarges current does not exceed 2.5 mA. Also it can be seen that at the “pin-to-plane” electrode geometry the current flows through the discharge gap only in the negative half-cycle voltage. This means the accumulation of charges on the plane electrode surface.

For determination of the active chemical species of barrier discharge the plasma spectrum of air was measured in the range from 200 nm to 1200 nm under an applied dc voltage of 15 kV and atmospheric pressure. The results showed the presence of nitrogen and oxygen lines. The main active components of the plasma are N^2 and N^{2+} and atomic oxygen. Also, there is a compounds of NO and OH. These spices are basis for treatment of living tissues, cells, and they have the disinfection effects. Figure 4 shows the plasma spectrum obtained at the “plane-to-plane" electrode geometry.

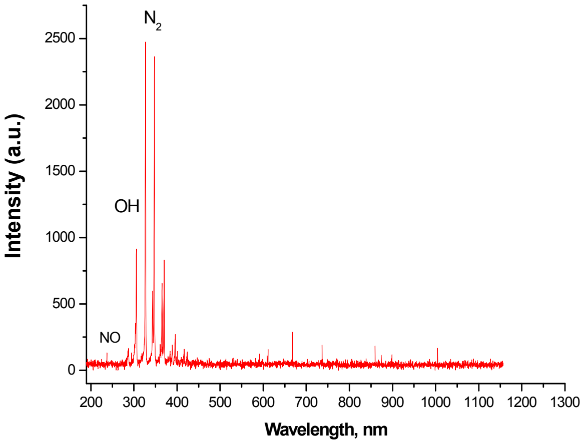

Figure 4 – The plasma spectrum of air at an applied voltage of 15 kVat “plane-to-plane” electrodes.

4 Conclusion

The dynamic current-voltage characteristics of dielectric barrier discharge and the plasma spectrum of at “plane to plane” and “pin to plane” electrode configurations were obtained. It is shown that the applied pin electrode reduces the number of streamer channels and the flow of the main current is only in the negative half-cycle of the voltage. The results of optical emission spectroscopy showed a decrease of the plasma intensity at the “pin-to-plane” electrodes. The experimental results can be useful in the study of the physical processes in varying combination with DBD electrode geometry.

Acknowledgments

This work has been supported by Ministry of Education and Science of the Republic of Kazakhstan under the Grant 3220/GF4/2015.

References

[1] U. Kogelschatz, B. Eliasson, W. Egli. From ozone generators to flat television screens: history and future potential of dielectric-barrier discharges // Pure Appl. Chem. – 1999. – Vol.71. – P.1819-1828.

[2] G.Y. Park, S.J. Park, M.Y. Choi, I.G. Koo, J.H. Byun, J.W. Hong, J.Y. Sim, G.J. Collins, J.K. Lee. Atmospheric-pressure plasma sources for biomedical applications // Plasma Sources Sci. Technol. – 2012. – Vol. 21. – P. 043001.

[3] K. Michael. Plasma for cancer treatment // Plasma Sources Sci. Technol. – 2015. – Vol. 24. – P. 033001.

[4] K.R. Lakshman, J.J.B. Gerard. Non-Thermal Plasma Treatment of Agricultural Seeds for Stimulation of Germination, Removal ofsurface Contamination and Other Benefits: A Review // Plasma Process. Polym. – 2015. – Vol. 12. – P. 608–623.

[5] P. Zhao, W. Zheng, J. Watanabe, Y.D. Meng, M. Nagatsu. Highly Conductive Cu Thin Film Deposition on Polyimide by RF-Driven Atmospheric Pressure Plasma Jets under Nitrogen Atmosphere // Plasma Process. Polym. – 2014. – Vol. 12 – P.431–438.

[6] Yu.S. Akishev, A.V. Dem'yanov, V.B. Karal'nik, A.E. Monich, and N.I. Trushkin. Comparison of the AC Barrier Corona with DC Positive and Negative Coronas and Barrier Discharge // Plasma Physics Reports. – 2002. – Vol. 29. – P. 82–91.

[7] ZheYu, Zhang Zhi-Tao, Yu Qing-Xuan, Xu Shao-Jie, Yao Jing, Bai Min-Dong, Tian Yi-Ping, Liu Kai-Ying.Atmospheric pressure streamer and glow-discharge generated alternately by pin-to-plane dielectric barrier discharge in air // Acta Phys. Sin. – 2012. – Vol. 61. – P. 195202.

[8] Yong-Hyuk Lee, Geun-Young Yeom. Characteristics of a Pin-to-Plate Dielectric Barrier Discharge in Helium / /Journal of the Korean Physical Society. – 2005. – Vol. 47. – P. 74-78.

[9] DineffP, and Gospodinova D. Electrode Configurations and Non-uniform Dielectric Barrier Discharge Properties // Factauniversitatis, ser.: elec. energ. – 2009. – Vol. 22. – P. 217-226.

[10] S.K. Kodanova, A.I. Kenzhebekova. Mathematical modeling of the barrier discharge point-plane geometry in nitrogen // Vestnik of KazNU. – 2014. – Vol. 51. – P. 90-95. (in Russian)

[11] O. Guaitella, C. Douat, S. Ponduri, F. Brehmer, S. Welzel, M.C.M. van de Sanden, R. Engeln. Role of surfaces in CO2 conversion with dielectric barrier discharges // 42nd European Physical Society Conference on Plasma Physics, Lisbon, Portugal. – 2015. – Vol. 22. – P. 303.

UDC 539.23, 539.216.1

R&d of cvd technique for graphene production

N.R. Guseinov, V.V. Kudryashov, G.A. Baigarinova, A.M. Ilyin

Al-Farabi Kazakh National University, IETP, al-Farabi 71, 050040 Almaty, Kazakhstan
e-mail: ilyinar@mail.ru

Currently production of large-sized graphene samples is of great importance due to the broad potential applications of this material with high physical performance. In this paper we consider one of the widely used methods of graphene production - chemical vapor deposition (CVD), which was worked out by our team. We used as a catalyst of Ni foil and carbon source were benzene vapor. Also, we show results of computer simulation by DFT methods that demonstrate possibility and effectiveness of graphene production by CVD method. The characteristics of graphene have been studied by optical microscopy and Raman spectroscopy. The results show high quality and homogeneity of the obtained graphene.

Key words: graphene, CVD, optical microscopy, Raman spectroscopy.
PACS numbers: 68.65.Pq

1 Introduction

Graphene is a crystal system consisting of a single layer of graphite, which elementary structural unit is a hexagonal cell, with its geometry resembling a honeycomb. Graphene causes a great interest because of its unique electronic, optical properties as well as chemical, thermal and mechanical characteristics [1]. The maximum electron mobility in graphene, as compared with all other known materials, making it promising for use in various applications, such as a future basis for nanoelectronics and possible replacement of silicon integrated circuits. The electronic properties of graphene depend to a large extent on the number of layers of graphene.

The famous “Scotch tape method” is a pioneer laboratory graphene production technique for basic research. But recently there was developed a variety of methods of controllable large-sized-graphene production. The two of these methods are the method of chemical vapor deposition (CVD) [2] and diffusion-based method. These techniques allow to control the number of graphene layers precisely.

Typical CVD graphene growth uses gaseous hydrocarbons at elevated temperatures as the carbon source, such as methane, ethylene, and acetylene [3,4]. While carbon nanotube growth has been demonstrated using liquid precursors, there have been only a few, recent attempts at graphene growth with liquid precursors. Single-layer graphene were synthesized from ethanol on Ni foils in an Ar atmosphere under atmospheric pressure by flash cooling after chemical vapor deposition, but a wide variation in graphene layer number was observed over the metal surface [5-7].

In this study single and few-layer graphene were successfully grown on nickel substrate using benzene as a precursor.

2 CVD graphene

2.1 Mechanism of graphene growth from benzene molecules on Ni

To produce graphene samples by CVD method we use benzene as precursor due to the similarity of benzene molecule with elementary hexagonal cell of graphene. The idea is not to decompose the whole molecule of precursor, as it commonly occurs in CVD processes, but just to dehydrogenate the benzene molecule, as it require less energy. Thereforecomputer simulation of graphene fragment formation from benzene molecules was performed using DFT method.

Figure 1a demonstrates the model of benzene molecule on nickel surface optimized by energy. Due to the probability of catalytic dehydrogenation on Ni substrate hydrogen atoms can be torn off the benzene molecule and adsorbed on the nickel surface (Fig.1 b). Fig.1c demonstrates two of the benzene molecules after the separation and adsorption of hydrogen atoms on nickel in the starting position at the distance between the nearest atoms of the carbon is 1.9 Å after energy optimization.

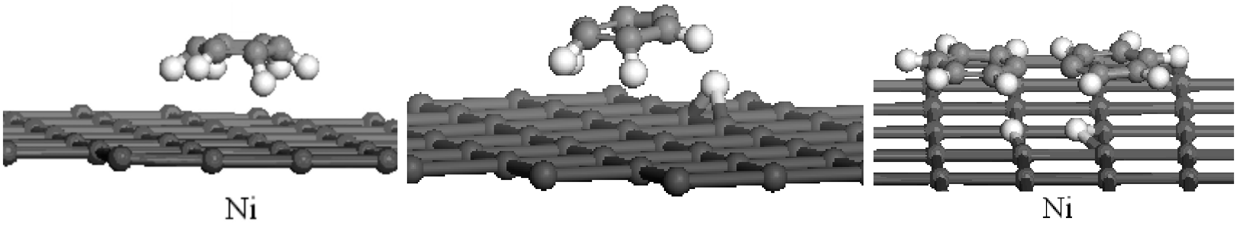

a b c

a – benzene molecule after optimization by energy on Ni surface;
b – benzene molecule after the separation and adsorption of H atom on Ni;
c – two partly dehydrogenated benzene molecules

Figure 1–Modeling of graphene formation from benzene molecules.

For more detailed study of this process computer simulation was conducted to predict possible stable states of benzene molecules (relative to each other) using optimization by energy. Figure 2a shows the two initial molecules of benzene, and then one molecule of benzene was once dehydrogenated. Figure2c shows both ionized (partial dehydrogenated) molecules of benzene, calculated distance between the nearest carbon atoms (1 and 2) is 1.43 Å, which is close to the bond length in graphene. Figure 2d demonstrates possible fragment of graphene formed due to the dehydrogenation of benzene molecules.

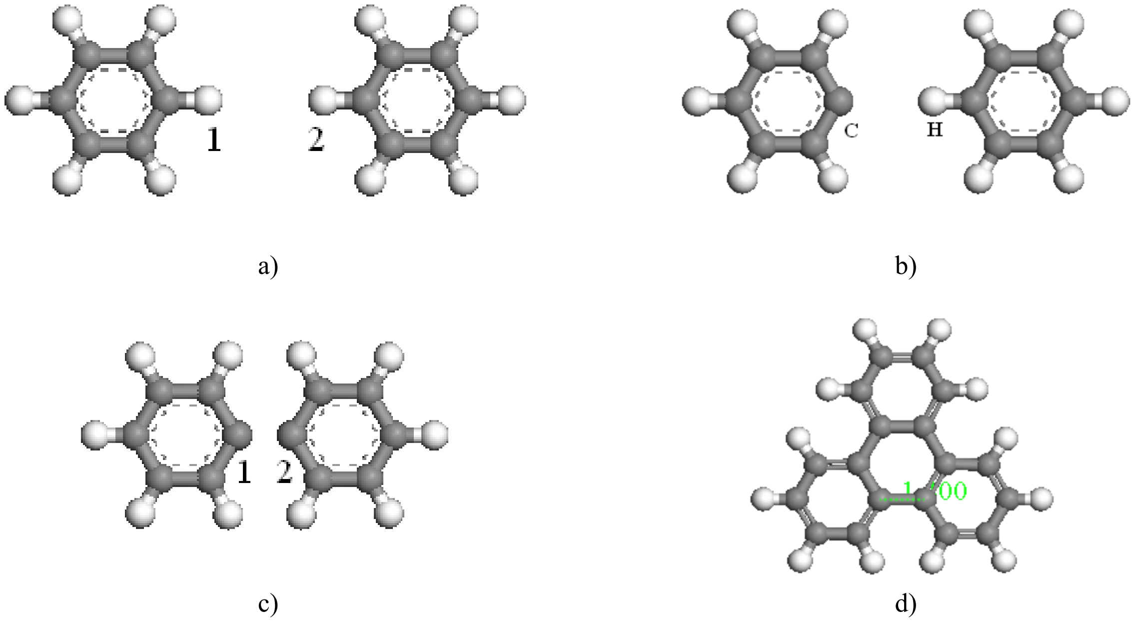

a) b)

c) d)

a – initial benzene molecules (equilibrium distance 1-2 is 2.91 Å);
b – one of benzene molecules is once dehydrogenated;
c – two partly dehydrogenated benzene molecules (equilibrium distance 1-2 is 1.43 Å);
d – fragment of graphene formed out of 3 partly dehydrogenated benzene molecules

Figure 2– Possible stable states of partly dehydrogenated benzene molecules.

2.2 Experimental setup

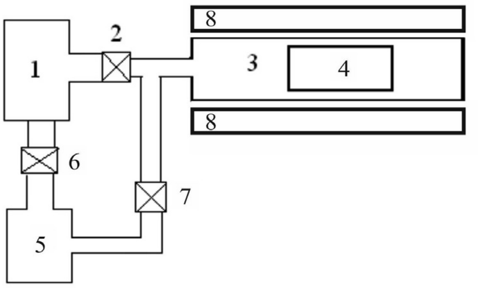

Figure 3–Scheme of experimental setup of CVD system

Source of benzene vapor - vessel 1, valve 2 separated from the reaction chamber 3. First of all argon from the vessel 5 is used for disposing the reaction chamber of an air, and then nickel substrate 4 is heated by resistive method. After that argon through the valve 6 is pulled into chamber 1 in order to press out of benzene vapor into reaction chamber. During this process nickel substrate is being covered by products of benzene dehydrogenation which results in graphene layers. All this process is accompanied by ultraviolet (λ≈ 365 nm) activation 8 of reactive medium.

Figure 4 demonstrates developed experimental setup of CVD system. It is built of the quartz tube (indicated by arrow 1), which is also mentioned as reaction chamber on the schematics; ultraviolet lamps (2); clamp terminals (3) and substrate holder situated within the tube.

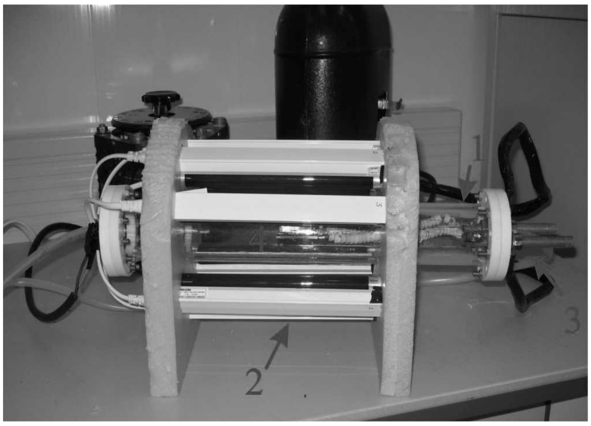

1 – Quartz tube (reaction chamber); 2 – source of ultraviolet irradiation; 3 – clamp terminals, 4– sample (substrate holder)

Figure 4–Experimental setup of CVD system

3 Results and discussion

Series of experiments were conducted varying such parameters as intensity of benzene inlet into reaction chamber and the temperature of the heated substrate.

Figure 5a is an optical image of single and few-layer graphene samples, obtained at t = 810^{o}C, during the inflow of benzene for 40 seconds. It was observed rather wide variation in graphene layer number on the Ni surface. In Fig. 5b it is shown the Raman spectrum of graphene, detected on the several areas of Ni substrate. The largest graphene sample is 8x6 μm^{2}.

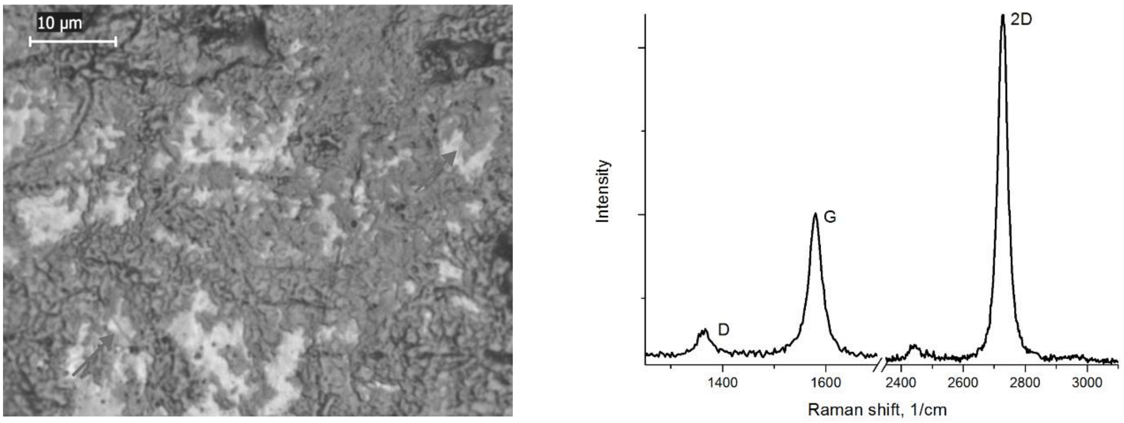

a) b)

Figure 5 – Optical image (a) and Raman spectrum of graphene (b), formed during the benzene inflow for 40 seconds

Further experiments were directed towards the varying of time of benzene inflow. Figure 6 is an optical image of the few-layer graphene sample, obtained at the same temperature - t = 810^{o}C, but during the benzene inflow for 30 seconds. Raman spectroscopy analysis of this sample showed that the variation in graphene layer number is still rather wide. The largest graphene sample is 5x5 μm^2.

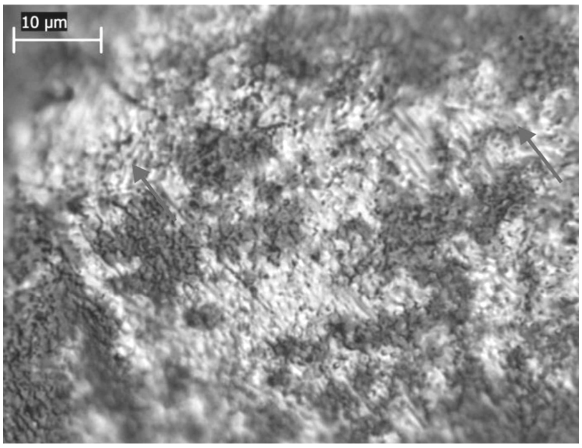

Figure 6 – Optical microphoto of single and few-layer graphene structure obtained during the benzene inflow for 30 seconds

After different variations of temperature and time of benzene inflow it were found out the optimal parameters of the process for production of homogeneous (by the number of layers) few-layer graphene samples on Ni substrate.

The Fig.7a is a typical microphotograph of few-layer graphene sample, obtained at t = 710^{o}C and during the lapping of benzene for 40 seconds. The Fig. 7b gives the Raman spectrum that corresponds to the most part of sample's surface. Intensity ratio of 2D and G peaks allows to attribute this sample to four-layer graphene. The largest grain of FLG is 50x65 μm^2.

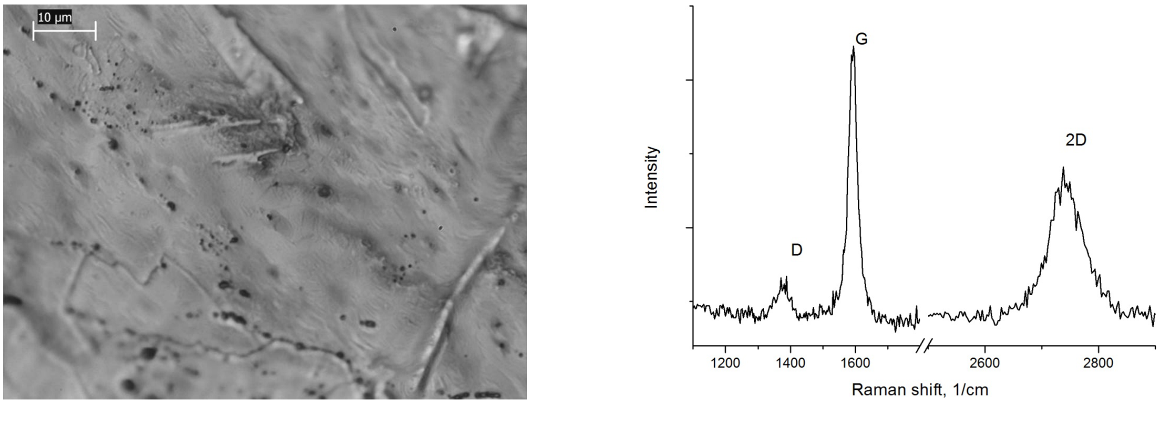

a) b)

Figure 7 – Optical microphoto (a) and Raman spectrum (b) of FLG structure obtained during the benzene inflow for 40 seconds

4 Conclusion

In the paper, relatively new developed method of high quality graphene mass production is presented. Possibility and effectiveness of graphene production by CVD method based on benzene was considered theoretically (computer simulation) and proved experimentally. Samples were investigated by optical microscopy and Raman spectroscopy. Performed analysis revealed a high quality of obtained FLG structures. Thus, we can say that presented in this study method of graphene production are notable for possibility of controllable production of rather large single and few-layer graphene samples of high quality.

References

[1] A.K. Geim, K.S. Novoselov. The rise of graphene // Nat Mater. – 2007. – Vol. 6. – P. 183-191.

[2] H.J. Park, J. Meyer, S. Roth, V. Skakalova. Growth and properties of few-layer graphene prepared by chemical vapor deposition // Carbon. – 2010. – Vol. 48. – P.1088-1094.

[3] Wei Liu, Hong Li, *et al.* Synthesis of high-quality monolayer and bilayer graphene on copper using chemical vapor deposition // Carbon. – 2011. – Vol.49. – P. 4122-4130.

[4] G. Nandamuri, S. Roumimov, R. Solanki. Chemical vapor deposition of graphene films // Nanotechnology. – 2010. – Vol. 21(14). – P. 145604.

[5] Y. Miyata, K. Kamon, K. Ohashi, R. Kitaura, M. Yoshimura, H. Shinohara. A simple alcohol-chemical vapor deposition synthesis of single-layer graphenes using flash cooling // Appl. Phys Lett. – 2010. – Vol. 96. – P. 2631053.

[6] X. Dong, P. Wang, W. Fang, C-Y. Su, Y-H. Chen, L-J. Li, *et al.* Growth of large-sized graphene thin-films by liquid precursor-based chemical vapor deposition under atmospheric pressure // Carbon. – 2011. – Vol. 49. – P. 3672-3678.

[7] A. Guermoune, T. Chari, F. Popescu, *et al.* Chemical vapor deposition synthesis of graphene on copper with methanol // Carbon. – 2011. – Vol. 49. – P. 4204-4210.

UDC 539.231, 538.9

Aluminum doped zinc oxide layers by atomic layer deposition and magnetron sputtering: formation and comparison of optoelectronic properties

G.K. Mussabek[1*], K.K. Dikhanbayev[1], V. Sivakov[2], F. Talkenberg[2],
S. Sailaubek[1], A.S. Djunusbekov[1], G.Ye. Ukenova[1], A.Ye. Kemelbekova[1]

[1]Al-Farabi Kazakh National University, IETP, al-Farabi 71, 050040 Almaty, Kazakhstan
[2]Leibniz Institute of Photonic Technologies, Jena, Germany
[*]e-mail: gauhar-mussabek@mail.ru

Thin films of aluminum-doped zinc oxide (AZO) were prepared using magnetron sputtering and atomic layer deposition (ALD) techniques. Atomic force microscopy (AFM) studies of AZO films surface morphology show that the surface of produced by ALDfilms is a smoother in comparison with films formed by magnetron sputtering.According to comparative analysis of optical transmittance spectra in the visible range of 300 - 800 nm, films formed by ALD technique demonstrates 10% higher transparency than those that obtained by magnetron sputtering. Investigation of samples electrical properties show that the conductivity of AZO films obtained by ALD technique actually two orders of magnitude higher than analogues obtained by magnetron sputtering.

Key words: zinc oxide, thin films, morphology, optical properties, electrical properties.
PACS numbers: 81.15.Gh, 73.61.-r.

1 Introduction

Al-doped Zinc oxide thin films have gained much attention due to their high light transmission and potential applications in the field of sensors [1], photovoltaics [2], electronics [3], biomedicine [4], as alternative for indium-tin oxide (ITO)[5]. There are several basic physical [6-8] and chemical [9, 10] methods of obtaining AZO, each of which has its advantages and disadvantages. One of the most novel and effective methods thin semiconductor films formation is an atomic layer deposition [11]. Another, widespread and well-known technique for producing semiconductor thin films with different elemental composition is a magnetron sputtering method [12, 13]. The main objectives of this work were a comparison of the AZO growth techniques such as atomic layer deposition and magnetron sputtering, study optical and electrical properties of obtained films and compare results.

2 Experimental details

The first group of test AZO samples prepared by atomic layer deposition, based on the sequential use of cyclic gas - solid-state transition reactions. ALD is a modified type of chemical vapor deposition (CVD) which enables very homogeneous film thicknesses on complex 3D geometries. The process of film growth in an ALD reactor is self-limited and based on surface reactions, which makes it possible to control the deposition at the atomic level. Keeping precursors separate from each other throughout the deposition process allows controlling the growth of atomic thickness of the film and obtaining the most accurate result for the atomic / molecular monolayer.

In all our experiments we used as a substrates laboratory borosilicate glass and p-type (100) monocrystalline silicon wafers with a specific resistivity of 10 Ω*cm. The native silicon oxide removal carried out by a 1 min dip in 2% HF.Deposition of films was performed by thermal ALD with a deposited doping of 1:10, 1:20, 1:30 and none doping in a commercial ALD reactor (OpAl, Oxford Instruments). Range of deposition temperature was 150°C to 300°C. Trim ethylaluminum (TMA), diethyl zinc (DEZ) and deionized water (H_2O) used as precursors of reactions. In the Fig.1,one can see a cycle repetition scheme of ALD- reactor according to the selected mode: complete film deposition cycle consists of alternating cycles of deposition of oxides of zinc and aluminum. The layers alternated in following mode: 20 cycles of ZnO and 1 cycle of Al_2O_3 deposition. Total cycle consisted of 21 monolayer deposition cycle and repeated 120 times, resulting in an AZO layer consisted of 2520 ALD deposition cycles. The scheme also shows the data for the duration of each constituent processes. The average thickness of resulting AZO films was 400 ± 20 nm. The deposition was conducted at 2 m Torr pressure in the reactor chamber.

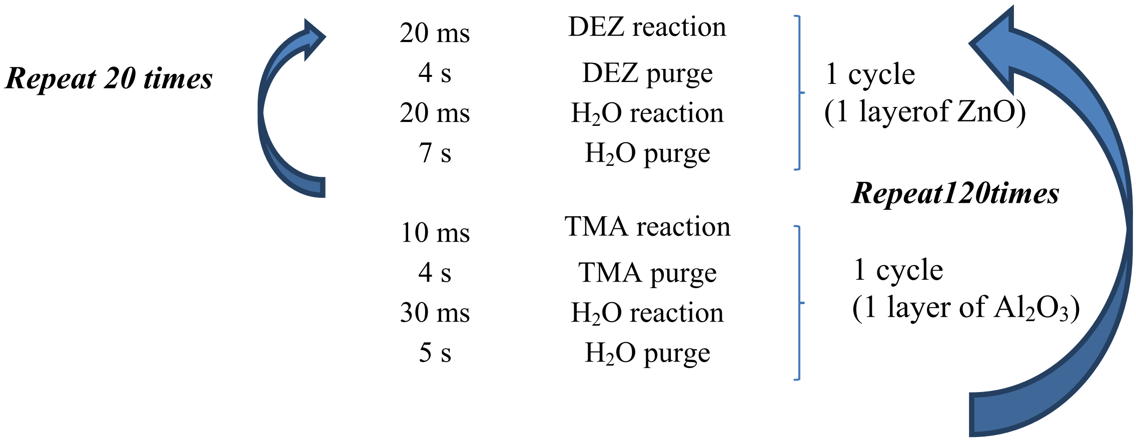

Figure 1 –Schematic representation of AZO thin film deposition experimental mode in the ALD reactor

The second group of experimental samples of AZO films obtained by the method of magnetron sputtering (VUP 5 deposition setup). In this deposition setup, the principle of targets cathode sputtering in magnetron discharge plasma is used. In our experiments as targets, we used Zn and Al mixed targets with different variations of the Al atoms concentration.AZO thin films deposited also on the surface of laboratory glass and p-type monocrystalline silicon wafers (100) with a specific resistivity of 10 Ω*cm at a temperature of 230°C and pressure of 5mTorr. The surface density of the discharge power ranged between 0.07 - 0 21 W/cm^2. The process conducted in $Ar_2:O_2$ mixture medium and the ratio of gases were 1:1.The average thickness of obtained AZO films was 400 ± 20 nm .

3 Results and discussion

The surface morphology of the AZO films was investigated by atomic force microscopy (AFM). In AFM images of AZO, obtained by atomic layer deposition, it is clearly seen that the surface is sufficiently smooth but contains irregularities in the form of needles of about 15-20 nm as shows in Fig. 2. The surface of AZO films with the presence of spherical features obtained by magnetron sputtering, is also quite homogeneous, but is looser than the surface of the films prepared by ALD technique as presented in Fig. 3. The averages size of the roughness in magnetron sputtered films was 35-40 nm. Data analysis of the surface morphology of the films obtained by two methods indicates that the use of ALD technology allow to obtain layers with more uniform and smooth surface.

One of the important characteristics for different optoelectronic application of investigated semiconductor material is an optical transparency. Optical parameters of samples were studied by means of spectrophotometry through measuring and analysis of transmission spectra in the optical range between 300 nm and 800 nm (Lambda 35, Perkin Elmer). In the Fig. 4the transmission spectra of the AZO films, obtained by ALD and magnetron sputtering are presented. There are shown transmission spectra of the AZO films deposited by both methods at the following aluminum and zinc ratios: 1:10, 1:20 and 1:30. Also, for the comparison of our experimental results, we added the spectrum of undoped ZnO film. The absorption edge of the undoped zinc oxide film is marked by dotted lines at the wavelength of 375 nm with a maximum of transmittance above 600 nm.

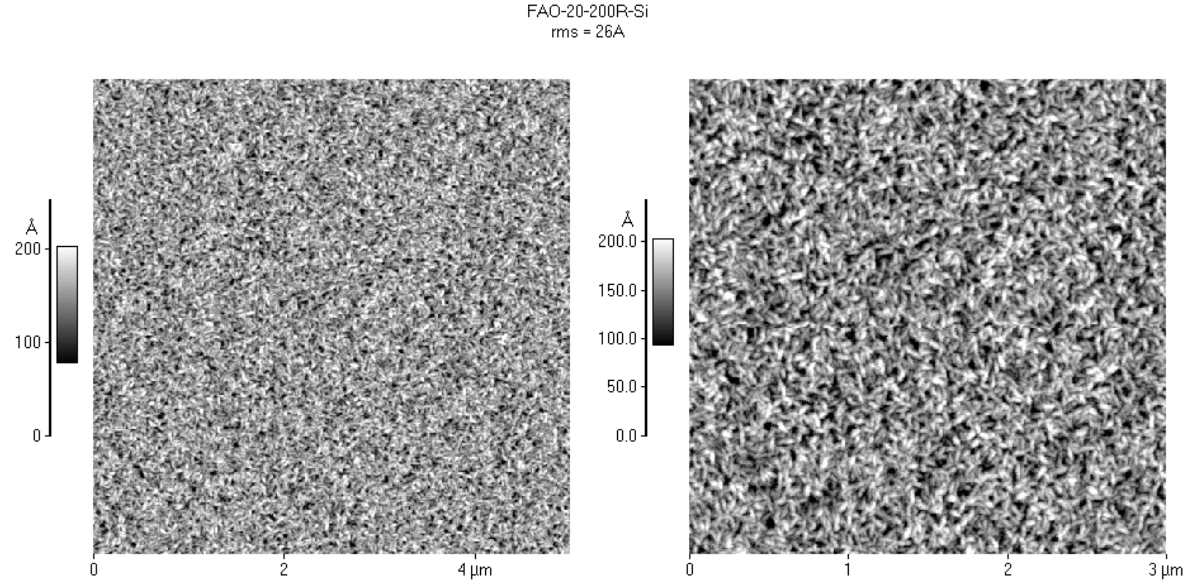

Figure 2 – AFM images of AZO film growth by atomic layer deposition method

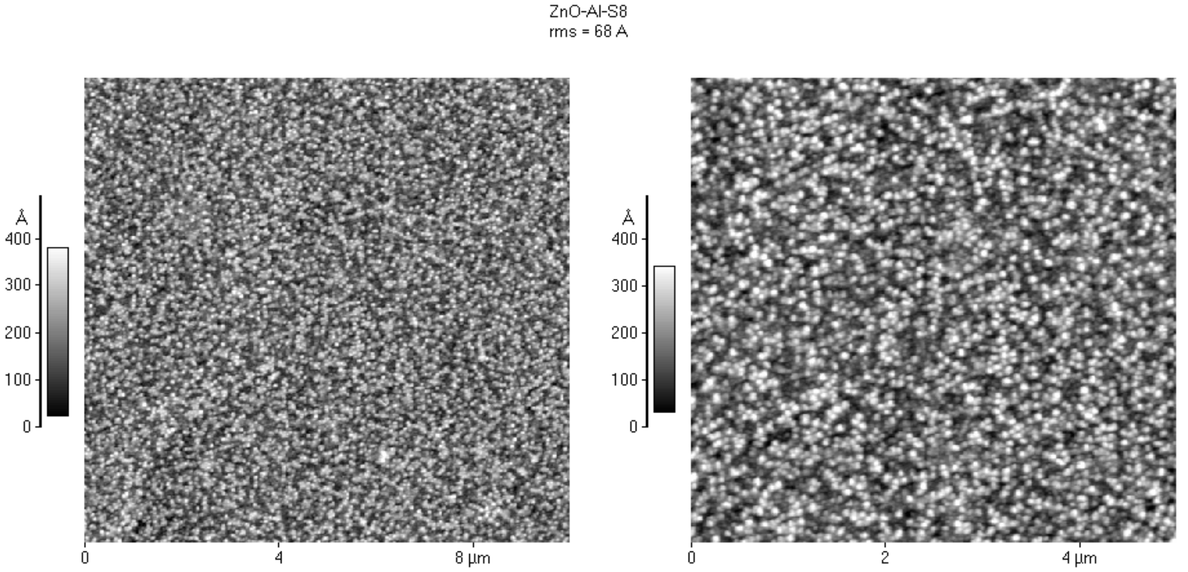

Figure 3 – AFM images of AZO film growth by magnetron sputtering deposition method

According to analysis of the spectra shown in the Fig. 4a, it follows that in the visible range of 400 nm - 800 nm transmittance of all samples, obtained by ALD, exceeds 90%. By all ALD AZO layers the transmittance is 10-20% higher in the 400-600 nm range. The maximum value of the transmittance reaches 99.4% for the sample obtained at the Al/Zn ratio of 1:10. The transmission spectra maxima occurs in the interval of 500 -550 nm. As concentration of dopant (Aluminum) increase transmission maxima shifted to shorter wavelengths area. The transmittance reduced to 70% in the area of the material's absorption edge, for which a blue shift is also observed. This result is very good indeed, because a high transparency rate of these films could become one of the key parameters for their application in photovoltaics and electronics related areas.

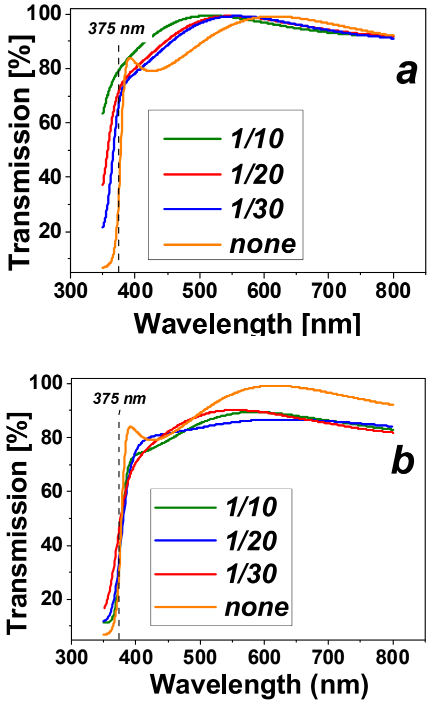

Figure 4 – The transmission spectra of AZO films growth by: (a) atomic layer deposition and (b) magnetron sputtering deposition method

The transmission spectra of AZO samples, produced by magnetron sputtering deposition are presented in the Fig. 4b. The spectra show that such AZO films also have a quite high transmittance in full visible range of 400-800 nm. The spectra of all examined samples there is a maximum transmission in the wavelength region of 500-550 nm. However, the maximum transmission does not exceed 90%. The similar transmittance to undoped ZnO layer was obtained for magnetron sputtered layer in the range between 400 up to 520 nm. The lower transmittance (10-15%) in comparison to undoped ZnO layer was obtained in the range between 520 up to 800 nm. Our results suggest that transparency of AZO films, produced by magnetron sputtering deposition is about 10-15% lowerin comparison of analogous layers produced by ALD method. Similar to AZO films, obtained by ALD, blue shifts of the transmission maximum and the absorption edge of the layer with increasing of dopant concentration obtained in transmission spectra of thin layers produced by magnetron sputtering deposition.

Another important criterion in the selection of materials for different technical applications is its electrical conductivity. Therefore, we measured the specific electrical resistivity of AZO layers, obtained at different concentrations of aluminum atoms and deposition temperatures. Resistivity of all AZO films was measured by four point method.Figure 5 represents a dependence of the r specific electrical esistivity average value on deposition temperature for ALD AZO films with different doping levels. The analysis of this study results that the minimum value of AZO films resistivity was obtained at the deposition temperature of 250°C for doped and undoped samples of zinc oxide layers. For all doped and undoped layers, there is observed almost the same behavior, thus with increasing deposition temperature resistivity of the material sharply decreases at first, then gradually. The lowest resistivity is 1.2 * 10^{-3} Ω*cm and respects to the sample obtained at 1:20 Al/Zn ratio.

For undoped zinc oxide layer the specific electrical resistivity minimum is almost observed at the deposition temperature of 250^0C and equal to $5.9*10^{-3}$ Ω*cm, hence, AZO films with doping ratio of 1:20 improves its conductivity almost for 5 times. As it shown in the Fig. 5 in the deposition temperature range of $250\text{-}300^0$C resistivity of all samples increases. This phenomenon is presumably because of at high temperatures atomic layer deposition process does not occur uniformly and too high kinetic energy of aluminum atoms results to their irregular deposition on the zinc oxide surface, thus conductivity of the output material suffers.

In order to compare the ALD AZO electrical characteristics with magnetron sputtered AZO layers the specific electrical resistivity was also measured for magnetron sputtered AZO films. Unfortunately, the electrical parameters of these films were very weak. The minimum value of the resistivity was 0.22 Ω*cm for sample obtained from the dopant concentration ratio Al/Zn of 1:20. Thus, the comparative analysis of the samples resistivity indicates that the conductivity of AZO films obtained by atomic layer deposition actually two orders of magnitude higher in comparison to the thin films obtained by magnetron sputtering.

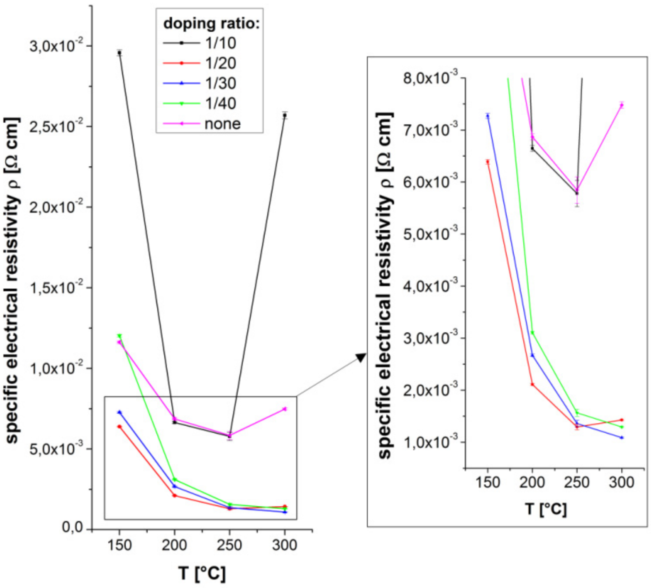

Figure 5 –Specific electrical resistivity of aluminum doped ZnO depending on deposition temperature and deposited doping ratio

4 Conclusions

We have performed experiments on formation of AZO films by atomic layer deposition and magnetron sputtering techniques. It is experimentally shown that the surface of produced by ALD AZO films is more smoother in comparison with those obtained by magnetron sputtering. According to comparative analysis of optical transmittance spectra in the visible range of 300 - 800 nm, layers formed by ALD technique demonstrates 10-15% higher transparency than those that obtained by magnetron sputtering or undoped ZnO layer. Investigation of samples electrical properties show that the specific electrical resistivity of AZO films obtained by ALD technique actually two orders of magnitude lower than analogues obtained by magnetron sputtering.

Following the findings based on presented experimental results, we concluded that the most optimal characteristics have AZO films produced by ALD. Besides, ALD allows to obtain a high quality AZO layers with optimal optoelectronic properties at comparatively low deposition temperatures that opens a new technological opportunities for using temperature sensitive surfaces, such as flexible polymers, as a substrate.

Acknowledgement

The National Science Foundation of Germany (DFG) under German–Kazakh Grant No. supported this work. SI1893/5-1 and by the Ministry of Education and Science of the Republic of Kazakhstan under Grant No.3205/GF4.

References

[1] M. Sushea, S. Christoulakis, K. Moschovis, N. Katsarakis, G. Kiriakidis. ZnO transparent thin films for gas sensor applications // Thin Solid Films – 2006. – Vol. 515. – № 2. – P.551-554.

[2] Chang Wei-Chen, Chang Yao-Yi, Yu Wan-Chin, Yao Yin-Chun, Lee Chia-Hua, Ko Hung-Han. Enhancing performance of ZnO dye-sensitized solar cells by incorporation of multiwalled carbon nanotubes // Nanoscale Research Letters. – 2012. – Vol.7. – P. 1-7.

[3] C. Dagdeviren, Hwang Suk-Won, Y. Su, Kim, H. Cheng, O. Gur, R. Haney, F.G. Omenetto, Y. Huang, J.A Rogers. Transient, Biocompatible Electronics and Energy Harvesters Based on ZnO // Small. – 2013. – Vol. 9. – № 20. – P. 3398-3404.

[4] Y. Zhang, T.R. Nayak, H. Hong, W. Cai. Biomedical Applications of Zinc Oxide Nanomaterials // Curr Mol Med. – 2013. – Vol. 13. – №10. – P. 1633-1645.

[5] X. Chen, J. Liu, J. Ni, Zhang X. Wide-spectrum Mg and Ga co-doped ZnO TCO thin films for solar cells grown via magnetron sputtering with H_2 introduction // Applied Surface Science. – 2015. – Vol. 328. – P. 193-197.

[6] T. Oh. Optical Characteristic of Al Doped ZnO Film Deposited by Radio Frequency Magnetron Sputtering on SiOC // International Journal of Engineering and Innovative Technology (IJEIT). – 2013. – Vol. 2.– № 12. – P. 137-139.

[7] L. Lu, J. Chen, L. Li, W. Wang. Direct synthesis of vertically aligned ZnO nanowires on FTO substrates using a CVD method and the improvement of photovoltaic performance // Nanoscale Research Letters. – 2012. – Vol. 7:293. – P. 1-8.

[8] S.M. George. Atomic Layer Deposition: An Overview // Chem. Rev. – 2010. – Vol. 110. – P. 111–131.

[9] Jun Min-Chul, Park Sang-Uk, Koh Jung-Hyuk. Comparative studies of Al-doped ZnO and Ga-doped ZnO transparent conducting oxide thin films // Nanoscale Research Letters. – 2012. – Vol.7:639.– P. 1-6.

[10] S. Baruah, J. Dutta. Hydrothermal growth of ZnO nanostructures // Sci. Technol. Adv. Mater. – 2009. – Vol. 10. – P.1-18.

[11] P. Banerjee, W.J. Lee, K.R. Bae, S.B. Lee, G.W. Rubloff. Structural, electrical, and optical properties of atomic layer deposition Al-doped ZnO films // J. of Appl. Phys. – 2010. – Vol. 108. – P. 043504.

[12] K.M. Yu, M.A. Mayer, D.T. He.H. Speaks, R. Zhao, L. Hsu, S.S. Mao, E.E. Haller, W. Walukiewicz. Ideal transparent conductors for full spectrum photovoltaics // Journal of Appl. Phys. – 2012. – Vol. 111. – P. 123505.

[13] Q. Li, Yu. Yuan-Hsin, A.S. Bhatia, L.D. Marks, S.C. Lee, Y.W. Chung. Low-temperature magnetron sputter-deposition, hardness, and electrical resistivity of amorphous and crystalline alumina thin films // J. Vac. Sci. Technol. A. – 2000. – Vol. 18. – №5. – P. 2333-2338.

UDC 537.311.3

Structure and electronic properties of amorphous $As_{40}Se_{30}S_{30}$ films prepared by ion-plasma sputtering method

O. Prikhodko[1], M. Maltekbasov[2], N. Almasov[1],
S. Maximova[1], V. Ushanov[1], S. Dyusembayev[1],
S. Kozyukhin[3]

[1] Al-Farabi Kazakh National University, IETP, al-Farabi 71, 050040 Almaty, Kazakhstan
[2]Zhansygurov Zhetysu State University, 058000, Zhansygurov 187a, Taldykorgan, Kazakhstan
[3]Kurnakov Institute of General and Inorganic Chemistry, RAS, 119991, Moscow, Russia

The atomic and local structure, as well as the electrical, optical, photoelectrical properties and drift mobility of charge carriers in amorphous $As_{40}Se_{30}S_{30}$ films, prepared by the method of RF ion-plasma sputtering (RF-films), were studied in comparison with those of the films, prepared by the method of thermal vacuum evaporation (TE-films). These two methods differ significantly in the conditions of substance vaporization and condensation of atoms on a substrate.

It was found that the films fabricated by the different methods have differences in structure and electronic parameters. The essential differences in photoconductivity and transport phenomena are observed, too.

It was concluded that RF $As_{40}Se_{30}S_{30}$ films have a modified structure. This leads to changes in the spectrum of extended and localized electronic states in these films, which, in its turn, causes differences in their electronic properties.

Key words: ion-plasma sputtering, RF-films, photoconductivity.
PACS numbers: 68.55.-a, 73.61.-r

1 Introduction

It was shown earlier that electronic properties of amorphous As_2Se_3 and As_2S_3 films, arsenic containing chalcogenide glassy semiconductors (ChGS) of binary composition, are strongly influenced by structure modification as a result of their preparation by ion-plasma sputtering method [1, 2]. Redistribution in electron energy spectrum in these modified films be assumed in the first place is due to As atoms presence in composition of the films. As a consequence it is of interest to study the films preparation technique influence on electronic properties of amorphous $As_{40}Se_{30}S_{30}$ films, arsenic containing ChGS of triple composition.

In this work the results of complex investigation of atomic and local structure, electrical, optical and photoelectrical properties as well as carrier drift mobility in $As_{40}Se_{30}S_{30}$ amorphous films, prepared by the methods of RF sputtering (RF films) in comparison to the results of the films prepared by thermal vacuum evaporation (TE films) are described.

2 Experimental

For the films fabricated by sputtering of a bulk ChGS target of the initial composition, the process was carried out in argon atmosphere at a frequency of 13.56 MHz and a pressure ~ 1 Pa. Fabrication of the films by evaporation was carried out in a vacuum of $\sim 4 \cdot 10^{-3}$ Pa on substrates kept at a room temperature. In the both methods The preparation parameters were selected so as to produce amorphous films with composition corresponding to that of the starting ChGS and having the maximum possible carrier drift mobility. The latter parameter is known to be one of the most structure-sensitive for semiconductor materials [3, 4].The thickness of the obtained films was varied from 0.5 to 5 µm.

To stabilize the structure and properties as-prepared films were annealed at temperature close to glass transition temperature of $As_{40}Se_{30}S_{30}$ 440 K for 30 min. The composition, morphology and amorphicity of the prepared films were determined by scanning electron microscope Quanta 3D 200i using energy-dispersive analysis and x-ray diffraction analyses, respectively.

The atomic structure of the amorphous films (the short- and medium range order in the atomic arrangement) was studied by x-ray diffraction analysis using CuK$_\alpha$ radiation (λ=1.5418Å). The x-ray grazing angle was constant and equal to 4.52º. The intensity of reflected x-rays was recorded in the range of diffraction angles 2θ from 5º to 140º. The results were reproducible within 2%.

The local structure of the films was analyzed by means of Raman spectroscopy. The Raman spectra were recorded at room temperature on T64000 (Horiba Jobin Yvon) spectrometer using light of DPY Nd:YAG laser (532 nm). Vertically polarized light of lasers were used in the backscattering (at an angle of 180^o) mode. The number of accumulations was the same at all measurements and equal to 25. The measurement error was ± 1 cm^{-1}.

The temperature dependence of the films conductivity was measured in the range from 300 to 430 *K*. The planar structure samples were used. The optical gap E_g of the films was found from spectral characteristics of absorption according to Tauc relation $(\alpha h\nu)^{1/2} \sim (h\nu - E_g)$ (where $h\nu$ is the photon energy), at absorption coefficient α corresponding to the fundamental absorption edge.

Charge carrier transport was studied at a room temperature using time-of-flight technique [3-5], with carriers injected into a sample by a 10 ns pulse of strongly absorbed light (0.337 μm). Films photoconductivity was studied using standard technique.

3 Results and discussion

Figures 1 and 2 show the chemical composition and morphology of amorphous RF and TE $As_{40}Se_{30}S_{30}$ films.

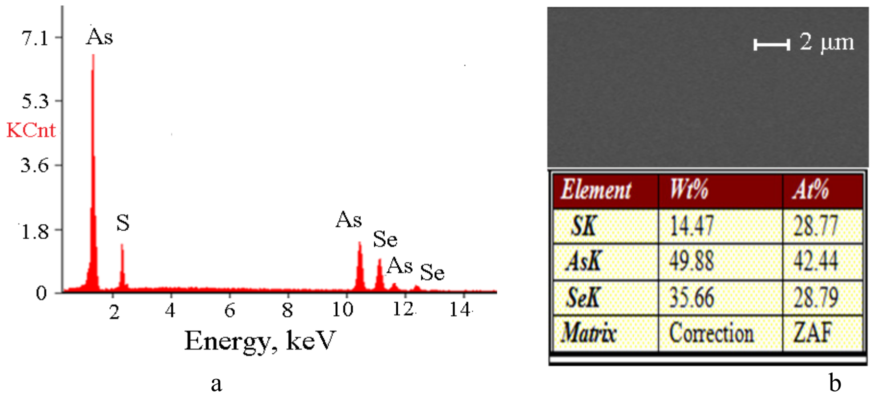

Element	Wt%	At%
SK	14.47	28.77
AsK	49.88	42.44
SeK	35.66	28.79
Matrix	Correction	ZAF

a b

Figure 1 – Energy-dispersive spectrum (a) and morphology (b) of RF a-$As_{40}Se_{30}S_{30}$ film

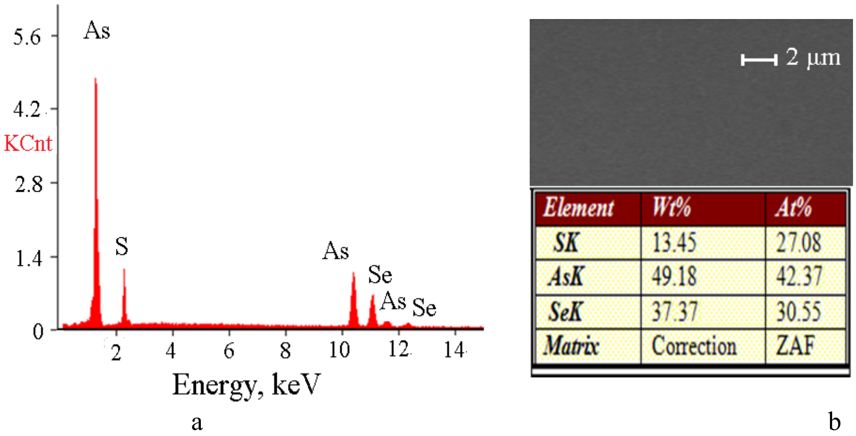

Element	Wt%	At%
SK	13.45	27.08
AsK	49.18	42.37
SeK	37.37	30.55
Matrix	Correction	ZAF

a b

Figure 2 – Energy-dispersive spectrum (a) and morphology (b) of TE a-$As_{40}Se_{30}S_{30}$ film

The results show that the a-$As_{40}Se_{30}S_{30}$ films prepared by both methods are continuous, and there are no unintentional impurities and the submicron sized defects in these films.

The composition of the films differed from that of initial material by less than 3% regardless of the preparing method.

Figure 3 (a, b) shows angular dependences of the x-ray diffraction intensity $I(2\theta)$ for RF and TE a-$As_{40}S_{30}Se_{30}$ films.

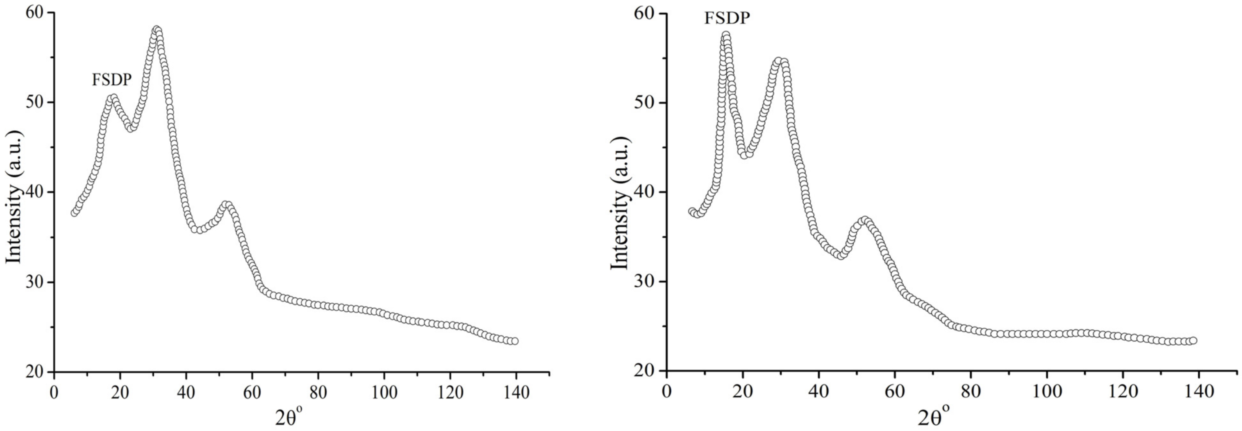

a

b

Figure 3 – X-ray diffraction patterns for RF (a) and TE (b) a-$As_{40}S_{30}Se_{30}$ films

It can be seen, that there are three distinct peaks on $I(2\theta)$ curves for films prepared by both methods. However, the diffraction peak amplitudes and peak half-widths differ for RF and TE films. These distinctions are particularly well seen for the first sharp diffraction peak (FSDP) in the curves. The FSDP curves made it possible to determine the wave factor S, at which the FSDP maximum is observed ($S = 4\pi\cdot\sin(\theta_{max1})/\lambda$, were θ_{max1} is the angle of the FSDP maximum; λ is the x-ray wavelength). FSDP on $I(2\theta)$ curves for RF and TE films are situated at $2\theta = 16.5^{o}$, and S=1.17 $Å^{-1}$. Linear dimensions of the local structural order regions (medium-range order), characterized by the parameter $L = 0.9\cdot\lambda/[B(2\theta)\cos(\theta_{max1})]$, where $B(2\theta)$ is the FSDP half-widths in radians, were estimated using the Scherrer's formula [6]. Medium range order parameter has been estimated to be 15 Å and 24 Å for RF and TE films, respectively. The 'quasi-period' d of the structure, whose existence within a certain correlation region gives rise to FSDP, was estimated using an approximate expression $d \approx 2\pi/S_{FSDP}$. For RF and TE films studied, d is 5.2 and 5.5 Å, respectively.

It should be noted that the difference in the short-range order structural parameters of RF and TE films is far from being as significant as the difference in the medium range order parameter L. The shorter dimension of the medium-range order region for RF films indicates that the structure of these films is more disordered. Besides, the photostructural changes in RF films are less obvious. It follows that the structure of these films is more rigid than that of the TE films.

Figure 4 shows the Raman spectra of RF and TE films. It can be seen that the spectrum of RF films as well as that of TE films have two general broad bands corresponding to vibrations of pyramidal structure units $AsSe_{3/2}$ (in the range from 200 to 300 cm^{-1}) and $AsS_{3/2}$ (in the range from 300 to 400 cm^{-1}). It follows that these pyramidal structure units are general units in the network of studied films. The peaks that modulate the contour of the bands and the frequencies of the peaks point on the presence of a great number of homopolar bonds such as As-As, Se-S, Se-Se and S-S in the network of the RF and TE films [7-9]. However the spectra of both RF and TE films have significant differences in the shape and intensity above mentioned general bands. In the spectra of RF films one can see a great number of clear recorded additional peaks that modulate the contour of the bands. Thus in RF films one can see the peaks with low intensity at frequencies 114, 167, 183, 202, 211, 218 cm^{-1} on the slope of the band (from 200 to 300 cm^{-1}) at low frequency region. These peaks correspond to different types of As-As and As-Se bond vibrations in structural molecular units such as $AsSe_{4/2}$, As_4Se_4 and As_4Se_3. These structural units can be present in the network of triple composition As-Se-S films because of their presence in the structure of the binary stoichiometric composition As_2Se_3 and As_2S_3 films [8-9]. The revealed differences in Raman spectra show significant differences in local structure of RF and TE films.

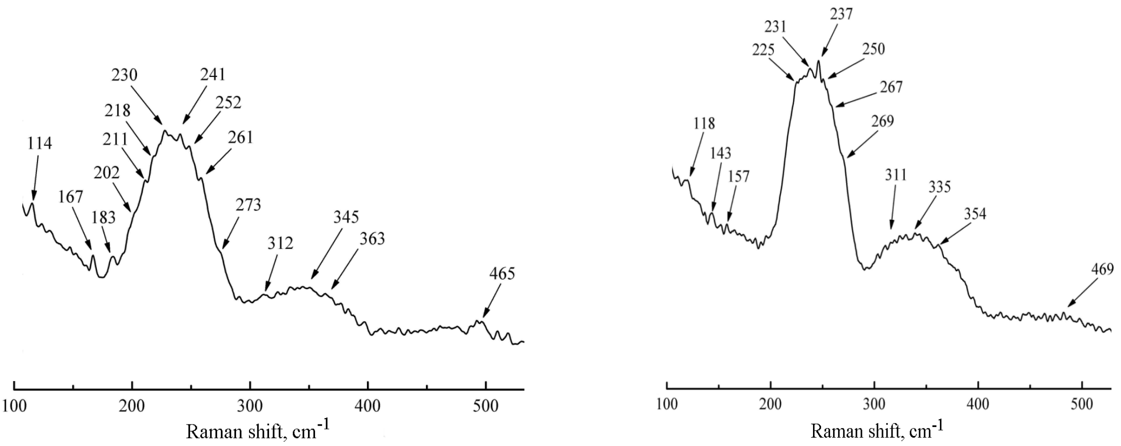

a b

Figure 4 – Raman spectra of a-$As_{40}S_{30}Se_{30}$ films: (a) RF film and (b) TE film

The results we obtained in studying the electrical and optical properties of amorphous RF and TE films were used to determine the following parameters of the films: conductivity σ at T= 300 K; activation energy of conductivity E_σ and optical band gap E_g as well as ΔE_F (shift of Fermi level with respect to the midgap) (Table). The error in these parameters, resulting from data scatter from sample to sample, are about half an order of magnitude for σ, $\Delta E_\sigma = \pm0.02$ eV and $\Delta E_g = \pm0.01$ eV for the activation energy and optical gap.

Table – Electronic parameters of amorphous RF and TE $As_{40}S_{30}Se_{30}$ films

Films	$\sigma(T=300\ K)$, Ohm^{-1}·cm^{-1}	E_σ, eV	C, Ohm^{-1}·cm^{-1}	E_g, eV	$\Delta E_F = E_g/2 - E_\sigma/2$, eV
RF	$6\cdot10^{-16}$	1.02	$3\cdot10^{3}$	1,89	- 0.08
TE	$1\cdot10^{-15}$	0.96	$4\cdot10^{3}$	2,08	0.08

One can see from the Table that the parameters of the RF and TE films are different. The RF films are characterized by lower conductivity, higher activation energy of conductivity and narrower optical gap. The contradiction between lower conductivity at narrow band gap can be accounted for by invoking concepts of the physic of amorphous semiconductors, concerning the antiparallel energy fluctuations of the band gap [3].

The spectral dependence of photoconductivity of the amorphous RF and TE films was measured in longitudinal regime at electric field strength ranging from 10^2 to 10^4 V/cm [10]. The “sandwich” structure samples were studied. It was found that the dependences for the RF and TE films have significant difference in short wavelength region (Figure 5). It is seen from Figure 5, that in TE films the photorectification takes place. On the contrary, the spectral characteristics of RF films don’t depend on the voltage polarity on illuminated electrode that is the evidence in favor of bipolar photoconductivity in these films.

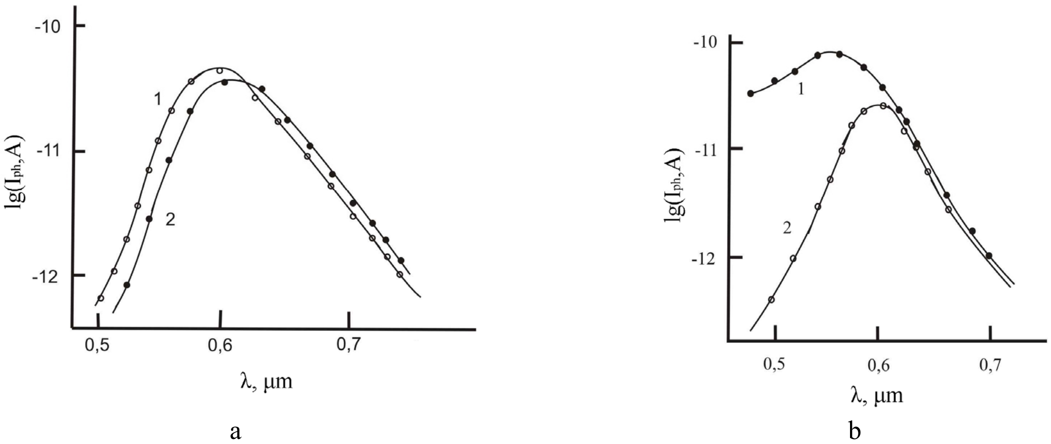

a b

Figure 5 – Spectral dependence of longitudinal photocurrent in RF (a) and TE (b) a-$As_{40}S_{30}Se_{30}$ films: 1 – positive and 2 – negative voltage polarity on illuminated electrode

Significant differences can be seen in charge carrier drift mobility μ studying for TE and RF films (E=10^5 V/cm, T=300 K) (Figure 6). The mobile charge carrier in TE films are the holes only ($\mu_p \approx 10^{-6}$ cm^2/(V·s)), but in RF films both electrons and holes are mobile ($\mu_p \approx \mu_p \approx 10^{-6}$ cm^2/(V·s)), that is the bipolar charge carrier transport occur.

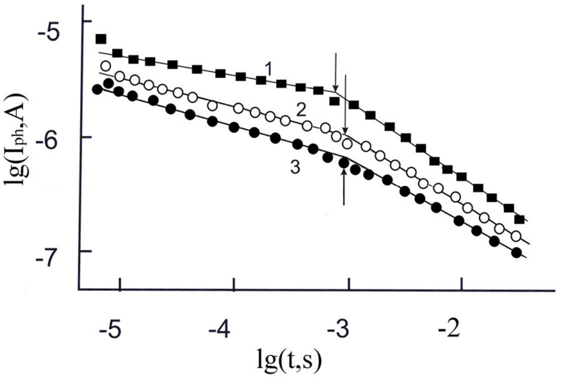

Figure 6 – Transient hole (1, 2) and electron (3) photocurrents in a-$As_{40}S_{30}Se_{30}$ TE (1) and RF(2, 3) films

The results of our photoconductivity and charge carrier drift mobility study are indicative of considerable redistribution in localized electron states controlling electron transport in RF films.

It should be noted that observed features in the differences of structure and electronic properties of RF and TE a-$As_{40}S_{30}Se_{30}$ films are similar to those for RF and TE As_2Se_3 and As_2S_3 films [1, 2, 11], that is the evidence in favor of important role of arsenic atoms in structure modification of RF films of arsenic containing lower coordinated ChGS.

4 Conclusion

Thus, the use of RF ion-plasma sputtering method for preparation of amorphous $As_{40}Se_{30}S_{30}$ films makes it possible to modify electronic properties of the films by changing their structure and opens new opportunities for controlling the electronic properties of amorphous films of arsenic containing chalcogenide glassy semiconductors.

Acknowledgments

The part of the research was carried out on No 4607/GF4 grant of Education and Science Ministry of RK

References

[1] Sh.Sh. Sarsembinov, O.Yu. Prikhodko, A.P. Ryaguzov, S.Ya. Maksimova. Comparison of atomic structures and electronic properties of amorphous AsSe films // Semicond. Sci .Technol. – 2001. – Vol. 16. – P. 872.

[2] Sh.Sh. Sarsembinov, A.P. O.Yu. Prikhodko, Ryaguzov, S.Ya. Maksimova, V.Z. Ushanov. Local structure and electronic properties of amorphous As2S3 films prepared by different methods // Semicond. Sci. Technol. – 2004. – Vol. 19. – P. 787.

[3] N.F. Mott and E.A. Devis. Electron Processes in Non-Crystalline Materials. – Oxford: Oxford University Press, 1979. 660 p.

[4] K.D. Tsendin. Electron Phenomena in Chalcogenide Glassy Semiconductors. –St Petersburg: Nauka, 1996. 486 p.

[5] W.E. Spear. Drift mobility techniques for the study of electrical transport properties in insulating solids // J. Non-Cryst. Solids. – 1969. – Vol. 1. – P. 197.

[6] J.P. de Neufville, S.C. Moss, S.R. Ovshinsky. Photostructural transformations in amorphous As2Se3 and As2S3 films // J. Non-Cryst. Solids. – 1973. – Vol. 13. – P. 191.

[7] L. Wenyan, S. Sudipta *et al.* Role of S⁄SeS⁄Se ratio in chemical bonding of As–S–Se glasses investigated by Raman, x-ray photoelectron, and extended x-ray absorption fine structure spectroscopies // J. Appl. Physics. – 2005. – Vol. 98. – P. 053503.

[8] N. Mateleshko, V. Mitsa, M. Veresa, M. Koosa. Investigation of nanophase separation in glassy as40se60 using raman scattering and ab initio calculations // Chalcogen. Letters. – 2004. – Vol. 1. – P. 139–144.

[9] N. Mateleshko, V. Mitsa, M. Veres, M. Koos, A. Stronski. Investigation of nanophase separation in IR optical glasses As40Se60 using resonant Raman scattering // Semicon. Phys., Quant. Elect. Optoelec. – 2004. – Vol. 7. – P. 171.

[10] Sh.Sh. Sarsembinov O.Yu. Prikhodko M.J. Maltekbasov S.Ya. Maksimova A.P. Ryagusov. Soh Deawha. Proc. Intern. Conf. on Advanced Sciences and Technologies – Korea: ICAST-98. – 1998. – 133 p.

[11] Sarsembinov Sh.Sh., Prikhodko O.Yu., Ryaguzov A.P., Maksimova S.Ya., Ushanov V.Z. Atomic structure and short- and medium-range order parameters in amorphous chalcogenide films prepared by different methods // J. of Non- Cryst. Solids. – 2007. – Vol. 353. – P. 2057–2061.

UDC 535:530.182

Nonlinear wave interactions in modern photonics

S.B. Momynov[1], E.S. Mukhametkarimov[1], I.R. Gabitov[2], A.E. Davletov[1,*]
[1]*Al-Farabi Kazakh National University, IETP, al-Farabi 71, 050040 Almaty, Kazakhstan*
[2]*The University of Arizona, Tucson, Arizona 85721 AZ, USA*
[*]*e-mail: askar@physics.kz*

One of the main factors impeding further progress in the field of application of met materials is significant energy losses due to the physical nature of exploited plasmon resonance, and their compensation is the most urgent problem to be addressed by the modern science of met materials. That is why this paper studies the parametric interaction of electromagnetic waves and, in particular, the process of generation and amplification of the second harmonic generation in met materials with the negative refractive index. It is found that the fundamental waves in the process of the second harmonic generation cannot exchange energy through the second harmonic wave at the non-collinear phase matching, and, thus, further consideration is required of optical rectification of the field in the nonlinear met materials.

Key words: met material, fundamental wave, second harmonic generation.
PACS: 42.70.Qs, 42.65.-k–

1 Introduction

Recent advances in the technology of structured materials made it possible to create new materials with unusual physical properties, which are not encountered in nature. The best known example of such materials is the so-called met materials that are nanocomposites with the negative refractive index [1,2].Such unique physical characteristics can be obtained by using structured materials, which include those based on metal-insulator [3,4], metal-organic [5,6] biological [7], and other media.

On the one hand the linear optical properties of met materials are well studied at the moment. On the other hand the invention of powerful sources of coherent radiation, associated with the creation of lasers, led to a new field of optics, nonlinear optics, which gave a direct impetus to the development of optoelectronic devices and information technologies. At present the formation of nonlinear optics of met materials is under way, which, along with effects similar to those of the classical nonlinear optics, discloses a number of phenomena that are unique for met materials. It should be noted that interest in the theory of nonlinear optical phenomena in met materials is heated by the problems of both fundamental science and potential applications in technology. Possible applications of met materials are still hampered by essential energy losses due to the plasmon resonance. Compensation of those losses is the most urgent problem to be addressed by the modern science of met materials. In this regard, this paper studies the parametric interaction of electromagnetic waves and, in particular, the process of generation and amplification of the second harmonic wave in met materials with the negative refractive index, with further focus on the effectiveness of frequency conversion and compensation of energy losses in met materials.

Second harmonic generation is a nonlinear optical process, in which electromagnetic waves with the same frequency interact with a nonlinear material to effectively generate electromagnetic wave with the doubled frequency. In the classical case, the second harmonic generation occurs in strongly nonlinear crystals with quadratic nonlinearity χ^2 [8,9]. It is well known that for an effective second-harmonic generation in ordinary matter the perfect phase matching $\Delta k = 2k_1 - k_2 = 0$ must be satisfied. In case of its violation a periodic exchange of energy between the fundamental wave and the second harmonic wave is observed.

2 Non-collinear second harmonic generation in met materials

Consider the process of the second harmonic generation in a met material with a negative refractive index. The phase matching is achieved by the interaction of two collinear waves of the fundamental frequency and the second harmonic wave, so that $\mathbf{k}_1^+ + \mathbf{k}_1^- + \mathbf{k}_2 = 0$, where $\mathbf{k}_1^{\pm}, \mathbf{k}_2$ denote the wave vectors corresponding to the pump waves and the second harmonic, see Fig.1. This situation is a generalization of the case of collinear second harmonic generation studied in [10].

In case of the non-collinear second-harmonic generation in a met material the pump wave and the second harmonic wave can be represented as follows:

$$\begin{aligned} E_1(t,\mathbf{r}) &= e_1^{(+)}(t,x,z)\exp\left[-i\omega t + i\mathbf{k}_1\cdot\mathbf{r}\right] + \\ &+ e_1^{(-)}(t,x,z)\exp\left[-i\omega t + i\mathbf{k}_2\cdot\mathbf{r}\right], \\ E_2(t,\mathbf{r}) &= e_2(t,x,z)\exp\left[-2i\omega t + i\mathbf{k}_3\cdot\mathbf{r}\right]. \end{aligned} \qquad (1)$$

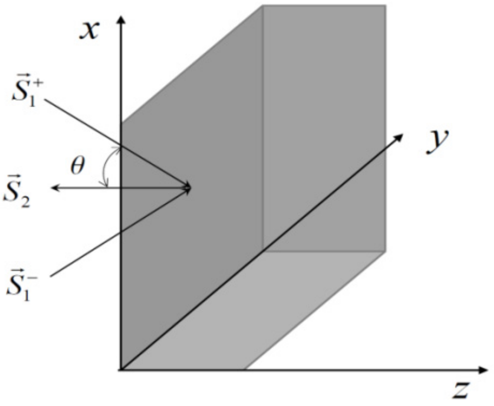

Figure 1 – Non-collinear SHG process. Two pump waves are incident at a certain angle to the normal of the met material surface. The directions of the respective energy fluxes are characterized by Poynting vectors $\mathbf{S}_1^{\pm}$. and $\mathbf{S}_2$, which is oppositely directed to the normal

It is assumed that at the fundamental frequency ω the refractive index of the metamaterial is negative, and it is positive at the second harmonic frequency 2ω. The second harmonic wave propagates oppositely to the normal of the metamaterial surface. The direction of the Poynting vector $\mathbf{S}_2$ of the second harmonic is opposite to the sum of the Poynting vector $\mathbf{S}_1^{\pm}$ of the pump waves, which is directed along the normal (see Fig. 1). That is, the second harmonic wave vector $\mathbf{k}_3$ is directed along the axis Z and the wave vectors $\mathbf{k}_1$ and $\mathbf{k}_2$ of the incident waves lie in the XZ plane, so that

$$\mathbf{k}_1 = k_1\begin{pmatrix} \eta_x \\ -\eta_z \end{pmatrix},\ \mathbf{k}_2 = k_2\begin{pmatrix} -\eta_x \\ -\eta_z \end{pmatrix}, \qquad (2)$$

where $\eta_x = \sin\theta$, $\eta_z = \cos\theta$, θ refer to the angle between vectors $\mathbf{k}_1$ and $\mathbf{k}_3$.

The set of equations describing the non-collinear synchronization at the second harmonic generation is written as follows:

$$\begin{aligned} &(-\eta_z\partial_z + \eta_x\partial_x + \upsilon_1^{-1}\partial_t)E_1^{(+)} = i\gamma_1 E_1^{(-)*}\varepsilon_2 e^{i\Delta\mathbf{k}\cdot\mathbf{r}}, \\ &(-\eta_z\partial_z - \eta_x\partial_x + \upsilon_1^{-1}\partial_t)E_1^{(-)} = i\gamma_1 E_1^{(+)*}E_2 e^{i\Delta\mathbf{k}\cdot\mathbf{r}}, \\ &(\partial_z + \upsilon_2^{-1}\partial_t)E_2 = i\gamma_2 E_1^{(-)}E_1^{(+)}e^{-i\Delta\mathbf{k}\cdot\mathbf{r}}. \end{aligned} \qquad (3)$$

Here $E_1^{(\pm)}$ and E_2 designate the complex envelopes of the electric fields of the pump and second harmonic waves with the corresponding group velocities $\upsilon_{1,2}$, $\gamma_{1,2}$ stand for the coefficients of the nonlinear interaction.

The mismatch in the vector synchronism $\mathbf{\Delta k}$ is then obtained in the form:

$$\Delta k = k_z(2\omega) + 2k(\omega)\eta_z. \qquad (4)$$

If $E_1^{(\pm)}$ and E_2 change slowly, they can be expressed as

$$\begin{aligned} E_1^{(\pm)}(x,z,t) &= \Phi_1^{(\pm)}(x)A_1^{(\pm)}(z,t), \\ E_2(x,z,t) &= \Phi_2(x)A_2(z,t), \end{aligned} \qquad (5)$$

and wave equations (3) can be rewritten as follows:

$$\Phi_2(x)\left(\frac{\partial}{\partial z} + \frac{1}{\upsilon_2}\frac{\partial}{\partial t}\right)A_2(z,t) = i\gamma_2\Phi_1^{(-)}(x)\Phi_1^{(+)}(x)A_1^{(-)}(z,t)A_1^{(+)}(z,t)e^{-i\Delta kz}. \qquad (6)$$

The last equation can be transformed to

$$\frac{\left(\partial_z + (1/\upsilon_2)\partial_t\right) A_2(z,t)}{i\gamma_2 A_1^{(-)}(z,t) A_1^{(+)}(z,t) e^{-i\Delta kz}} = \frac{\Phi_1^{(-)}(x)\Phi_1^{(+)}(x)}{\Phi_2(x)}, \quad (7)$$

in which the right side of equation (7) depends on z, whereas the left function singly depends on x. This means that the left hand side of (7) is constant, that is:

$$\frac{\Phi_1^{(-)}(x)\Phi_1^{(+)}(x)}{\Phi_2(x)} = const. \quad (8)$$

The equations for the incident waves can be rewritten as follows:

$$\begin{aligned} &\Phi_1^{(\pm)}(x)\left(-\eta_z \frac{\partial}{\partial z} + \frac{1}{\upsilon_1}\frac{\partial}{\partial t}\right) A_1^{(\pm)}(z,t) \pm \\ &\pm \eta_x \frac{\partial \Phi_1^{(\pm)}}{\partial x} A_1^{(\pm)}(z,t) = \quad (9) \\ &= i\gamma_1 \Phi_1^{(\mp)*}(x)\Phi_2(x) A_2(z,t) A_1^{(\mp)*}(z,t) e^{+i\Delta kz}. \end{aligned}$$

Dividing this expression by $\Phi_1^{(\pm)}$ gives rise to

$$\frac{\Phi_2(x)\Phi_1^{(\pm)*}(x)}{\Phi_1^{(\mp)}(x)} = m\left|\Phi_1^{(\mp)}(x)\right|^2. \quad (10)$$

Assume that $\left|\Phi_1^{(\mp)}(x)\right|^2 = 1$. Then, the equation for the incident wave is written as

$$\begin{aligned} &\left(-\eta_z \frac{\partial}{\partial z} + \frac{1}{\upsilon_1}\frac{\partial}{\partial t}\right) A_1^{(\pm)}(z,t) \pm \\ &\pm \eta_x \frac{1}{\Phi_1^{(\pm)}} \frac{\partial \Phi_1^{(\pm)}}{\partial x} A_1^{(\pm)}(z,t) = \quad (11) \\ &= i\gamma_1 m A_2(z,t) A_1^{(\mp)*}(z,t) e^{+i\Delta kz}. \end{aligned}$$

Separating the variables yields

$$\frac{1}{\Phi_1^{(\pm)}} \frac{\partial \Phi_1^{(\pm)}}{\partial x} = const^{(\pm)}, \quad (12)$$

which allows one to conclude that $\Phi_1^{(\pm)} = C^{(\pm)} e^{\pm const^{(\pm)} x}$.

Taking into account that $\left|\Phi_1^{(\mp)}(x)\right|^2 = 1$,one finds that $\Phi_1^{(\pm)} = e^{\pm i l_1 x}$, where l_1 are arbitrary constant.

Finally, taking into account all the substitutions, equation (11) can be rewritten as:

$$\begin{aligned} &\left(-\eta_z \frac{\partial}{\partial z} + \frac{1}{\upsilon_1}\frac{\partial}{\partial t}\right) A_1^{(\pm)}(z,t) \pm \\ &\pm i l_1 \eta_x A_1^{(\pm)}(z,t) = \quad (13) \\ &= i\gamma_1 m A_2(z,t) A_1^{(\mp)*}(z,t) e^{+i\Delta kz}. \end{aligned}$$

Using the phase shift in the substitution $A_1^{(\pm)} = A_1^{(\pm)} \exp(i l_1 \eta_x / \eta_z)$the left hand side of equation (13) can be eliminated. Thus, the set of equations describing the interaction of three non-collinear waves in the nanocomposite medium, i.e. a metamaterial with the negative refractive index, is found as:

$$\begin{aligned} &\left(-\eta_z \frac{\partial}{\partial z} + \frac{1}{\upsilon_1}\frac{\partial}{\partial t}\right) A_1^{(+)}(z,t) = i\gamma_1 A_2(z,t) A_1^{(-)*}(z,t) e^{+i\Delta kz}, \\ &\left(-\eta_z \frac{\partial}{\partial z} + \frac{1}{\upsilon_1}\frac{\partial}{\partial t}\right) A_1^{(-)}(z,t) = i\gamma_1 A_2(z,t) A_1^{(+)*}(z,t) e^{+i\Delta kz}, \\ &\left(\frac{\partial}{\partial z} + \frac{1}{\upsilon_2}\frac{\partial}{\partial t}\right) A_2(z,t) = i\gamma_2 A_1^{(+)}(z,t) A_1^{(-)}(z,t) e^{-i\Delta kz}. \end{aligned} \quad (14)$$

Consider the stationary case in which the set of equations (14) can be rewritten as follows:

$$\begin{aligned} &-\eta_z \frac{\partial}{\partial z} A_1^{(+)}(z) = i\gamma_1 a_2(z) A_1^{(-)*}(z), \\ &-\eta_z \frac{\partial}{\partial z} A_1^{(-)}(z) = i\gamma_1 a_2(z) A_1^{(+)*}(z), \quad (15) \\ &\frac{\partial}{\partial z} a_2(z) - i\Delta k a_2(z) = i\gamma_2 A_1^{(+)}(z) A_1^{(-)}(z). \end{aligned}$$

On substituting $A_2(z) = a_2 \exp(-i\Delta kz)$, $z / z_0 = x$, $\Delta k = \Delta$, $\eta_z = \alpha$ gives rise to the following set of equations in dimensionless form:

$$-\frac{\partial}{\partial x}e_1^{(+)}(x)=ie_2(x)e_1^{(-)*}(x),$$
$$-\frac{\partial}{\partial x}e_1^{(-)}(x)=ie_2(x)e_1^{(+)*}(x), \qquad (16)$$
$$\frac{\partial}{\partial x}e_2(x)-i\delta e_2(x)=ie_1^{(+)}(x)e_1^{(-)}(x).$$

The normalization of the amplitude of the interacting waves are defined herein as $A_1^{(\pm)}=(1/z_0)\sqrt{\alpha/\gamma_1\gamma_2}e_1^{(\pm)}$, $a_2=(\alpha\Delta/\gamma_1 z_0)e_2$ and $\delta=\Delta z_0$ .If the length of the sample is denoted as l, the boundary conditions in this case can be written as:

$$e_1^{(\pm)}(0)=e_{10}^{(\pm)}\exp(i\phi_{10}),\ e_2(l)=0. \qquad (17)$$

Thus, the set of differential equations (16), describing non-collinear wave interaction at the SHG, should be solved together with boundary conditions (17), set at the opposite ends of the sample.

The set of equations (16) can be rewritten in terms of amplitudes and phases, by setting $e_1^{(\pm)}=u^{(\pm)}\exp(i\varphi_1^{(\pm)}),\ e_2=v\exp(i\varphi_2)$ and subsequent separation of the imaginary and real parts yields:

$$\partial_z u^+=vu^-\sin\theta,$$
$$\partial_z u^-=vu^+\sin\theta,$$
$$\partial_z v=u^+u^-\sin\theta, \qquad (18)$$
$$\partial_z\theta=\left(vu^-/u^+ + vu^+/u^- + u^+u^-/v\right)\cos\theta-\delta,$$
$$u^\pm(0)=u_0^\pm,\ \text{v}(l)\text{=0},\ \theta(l)\text{=-}\pi/2,$$

where $\theta=\varphi_2-\varphi_1^+-\varphi_1^-$, $\varphi_1^\pm$ and φ_2 denote the phases of the pump and second harmonic waves, respectively.

The presence of a common factor $\sin\theta$ in the equations above means that the exchange of energy between the harmonics takes place in such a way that the fundamental waves both lose or gain some energy at the same time, that is the energy exchange between the fundamental waves u^- and u^+ through the second harmonic is impossible.

The set of equations (18) has three first integrals, among which are the Manley-Rowe relations:

$$\left(u^+\right)^2-v^2=m_1^2,$$
$$\left(u^-\right)^2-v^2=m_2^2, \qquad (19)$$
$$\left(u^+\right)^2-\left(u^-\right)^2=m_1^2-m_2^2,$$

where $m_{1,2}=u_1^\pm(l)$.

The last equation in (18) can be easily integrated to give:

$$u^+u^+v\cos\theta-v^2\delta/2=m_3, \qquad (20)$$

where m_3 is a constant .

It follows from the last expression that $m_3=0$, $F=\cos\theta=v\delta\Big/\left[2\sqrt{(v^2+m_1^2)(v^2+m_2^2)}\right]$. The maximum value of this function is achieved at the point $v_0=\sqrt{m_1m_2}$. Taking into account the inequality, $\left|\cos\Phi\right|\le 1$ allows one to conclude that, like in the collinear case, there are two regimes of the second harmonic generation. In case of $\left|\delta\right|\le\delta_{cr}=2(m_1+m_2)$, v can take any value, increasing indefinitely along the axis z . This in turn means that for the entire range energy $0\le z\le L$ the energy is transferred from the fundamental wave to the second harmonic. In case of $\left|\Delta\right|>\Delta_{cr}$ the domain of allowed values of v lies in the interval $0\le v\le v_0$, where

$$v_0=\sqrt{K-\sqrt{K^2-64m_1^2m_2^2}}\Big/2\sqrt{2},$$

$K=\delta^2-4(m_1^2+m_2^2)$. Thus, the exchange of energy between the fundamental wave and the second harmonic takes place along the sample, leading to spatial oscillations of the amplitudes of the interacting waves. In Figure 2, the curves of the function $F=\cos\theta$ are plotted for different values of the amplitude of the second harmonic which corresponds to the solid line with $\left|\delta\right|=2(m_1+m_2)$. For the lower curve $\left|\delta\right|<2(m_1+m_2)$ and in this case the amplitude of the second harmonic wave can take arbitrary values. If $|\delta| > 2(m_1 + m_2)$,there are forbidden bands for the values of the amplitudes of the second harmonic corresponding to the upper curves. This is the so-called supercritical regime of the second harmonic generation.

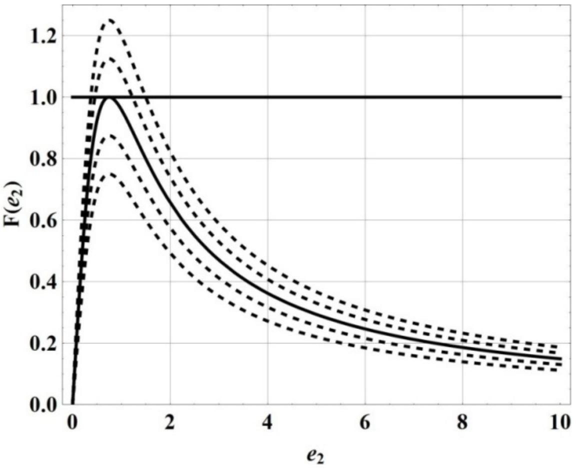

Figure 2 – The dependence of the function $F = cos\theta$ on the amplitude of the second harmonic at m$_1$ – 0.8, m$_2$ 0.7

Using the conservation laws (19) together with (18) the following equation for the intensity of the second harmonic is derived for $m_3 = 0$:

$$\frac{d}{dz}v^2 = -2\sqrt{v^2(m_1^2+v^2)(m_2^2+v^2)-(\frac{v^2}{2}\delta)^2}. \quad (21)$$

Let the intensity of the second harmonic be such that $v^2 = P$ and, then, the last equation is rewritten in the form

$$\frac{\partial P}{\partial z} = -\sqrt{4P^3 + (4(m_1^2+m_2^2)-\delta^2)P^2 + 4m_1^2m_2^2P}, (22)$$

and its solution is found as:

$$-\int \frac{dP}{\sqrt{4P^3 + (4(m_1^2+m_2^2)-\delta^2)P^2 + 4m_1^2m_2^2P}} = \int dz. (23)$$

The integral on the left side is elliptical, and the solution of (23) can be expressed by using the Weierstrass function. Thus, the solution of (21) can be written as:

$$z - l = -\int \frac{ds}{\sqrt{4s^3 - g_2 s - g_3}}. \quad (24)$$

Here $P = P_0 + 6f'(P_0)/(24s - f''(P_0))$, where P_0 is one of the roots of the polynomial $f(P) = 4P^3 + (-K)P^2 + 4m_1^2m_2^2P$, $K = \delta^2 - 4(m_1^2 + m_2^2)$.

The polynomial under the square root of equation (24) has the following roots:

$$P_a = 0,$$
$$P_{b,c} = \frac{1}{8}(K \mp \sqrt{(K^2 - 64m_1^2m_2^2}). \quad (25)$$

The invariants of the Weierstrass function g_2 and $g_3$are, thus, equal to:

$$g_2 = \frac{1}{12}(-K)^2 - 4m_1^2m_2^2,$$
$$g_3 = \frac{1}{3}m_1^2m_2^2(-K) - \frac{1}{216}(-K)^3. \quad (26)$$

A special feature of this case is that at perfect phase matching of $\delta = 0$, the solution is expressed in terms of Jacobi elliptic functions :

$$P = v^2 = -m_1^2 sn^2[im_2(z-l), \frac{m_1^2}{m_2^2}]. \quad (27)$$

Solutions for the intensities of the remaining two pump waves are easily found using expression (19).It should be noted that in the collinear interaction of waves solutions are expressed in terms of hyperbolic functions at $\delta = 0$.In the case of $|\delta| > \delta_{cr} = 2(m_1 + m_2)$ the second harmonic wave $v$starts to exchange energy with the pumping waves u^+ and u^-. Figure 3 shows the intensity of the second harmonic wave from as a function of the coordinate z. The solid curve corresponds to the perfect phase matching at which the energy is permanently transferred to the second harmonic along the entire sample. The dashed curve corresponds to the critical value of the phase mismatch when $\delta > \delta_{cr}$ and the energy exchange between the pump waves and second harmonic takes place along the sample, i.e. the amplitude of the second harmonic turns a periodic function of the coordinate. Thus, in contrast to the classical case, the effective frequency conversion in metamaterials is possible for the whole range of the phase mismatches both in collinear or non-collinear matching which is quite an attractive feature in sense of possible applications.

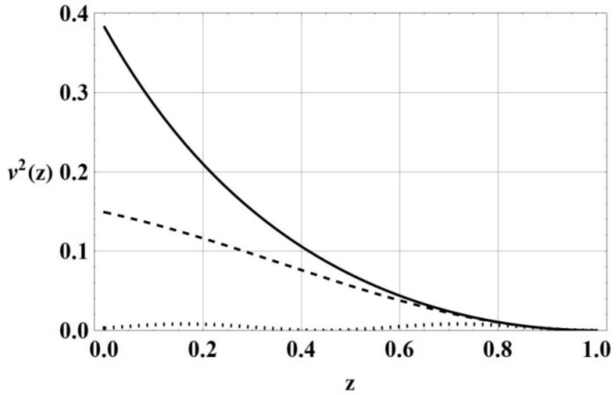

$u_{10}^{+}=1$, $u_{10}^{-}=0.9$, $l=1$

Solid line – $\delta < \delta_{cr}$, dashed line – $\delta < \delta_{cr}$,
dotted line – $\delta < \delta_{cr}$

Figure 3 – Spatial profiles of the second harmonic wave along the sample at different values of δ

In the ideal phase matching solution (18) for the wave intensity is written as follows:

$$v(z)^2 = -m_1^2 \operatorname{sn}^2\left[im_2(z-l), \frac{m_1^2}{m_2^2} \right],$$

$$\left(u^{+}(z)\right)^2 = v(z)^2 + m_1^2,\ \left(u^{-}(z)\right)^2 = = v(z)^2 + m_2^2. \quad (28)$$

Note that expressions (28) are implicit solutions of (18), since they contain undefined parameters such as m_1 and m_2, which are corresponding values of the amplitudes of the pump waves at the right end of the sample $u^{+}(l)$, $u^{-}(l)$. To determine the dependence of $m_{1,2}$ on the amplitude of the input value of $u^{\pm}(0)$ the following transcendental equations must be solved:

$$\left(u^{\pm}(0)\right)^2 = v(0)^2 + m_{1,2}^2. \quad (29)$$

The results of the numerical solution of transcendental equations (29) are shown in Figures 4-5. Figure 4 corresponds to the case of ideal phase matching, in which the curve of the amplitude of the incident pump wave at the right end of the sample as a function of its value at the left end has several branches. The physical meaning can only be prescribed to the lower branch, whereas for the parameters of the upper branches the fields within the sample can take infinite values. It follows from the analysis of the behavior of the lower branch that the second harmonic reaches saturation, which corresponds to the total transformation of the energy of the fundamental waves into the energy of the second harmonic.

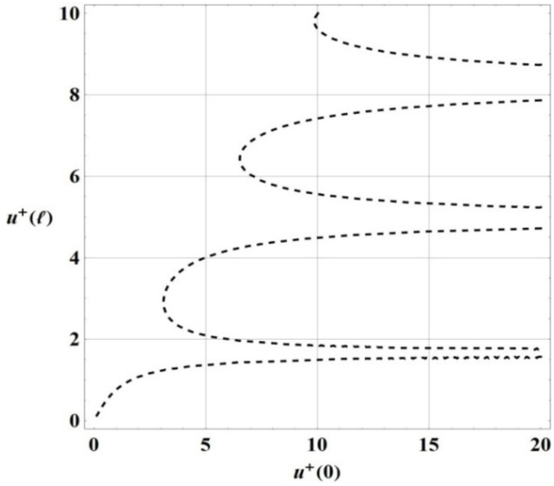

Figure 4 – The dependence of the amplitude of the pump wave $u^{+}(l) = m_1$ on $u^{+}(0)$

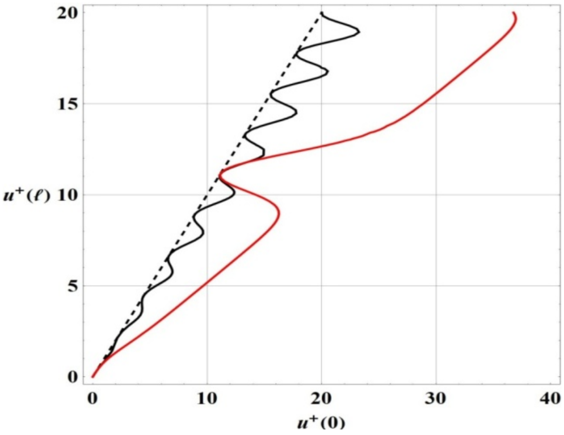

Red curve: $|\delta| \sim \delta_{cr} = (m_1 + m_2)$,
black curve: $|\delta| \sim 2.2(m_1 + m_2)$,
dashed curve: $|\delta| \sim 20(m_1 + m_2)$

Figure 5– The dependence of the amplitude of the pump wave $u^{+}(l) = m_1$ on $u^{+}(0)$

3 Conclusions

The curves in Figure 5 show the intensity of the fundamental wave at the left end of the sample $u^{+}(0)$ as a function of its value $u^{+}(l)$ at the right end in the supercritical regime of SHG. The red curve corresponds to the case of $|\delta| \sim \delta_{cr} = 2(m_1 + m_2)$, the black curve is drawn for $|\delta| \sim 2.2(m_1 + m_2)$, and for the dashed curve $|\delta| \sim 20(m_1 + m_2)$. For quite large values of the phase mismatch the dependence is almost linear, which actually prevents the SHG since the energy transfer from the fundamental wave to the second harmonic does not take place, and the intensity of the incident fundamental waves remains unchanged while passing along the sample. For values of the phase mismatch not higher than the critical one, rapid oscillations occur due to the periodic exchange of energy between the fundamental wave and the second harmonic.

In a case of non-collinear phase matching it is found for the second-harmonic generation in a metamaterial with the negative refractive index that the fundamental waves simultaneously either lose or gain energy, i.e. the energy exchange between them through the second harmonic turns impossible. Nevertheless, the exchange of energy between the pump waves is possible the constant field appearing due to the optical rectification, which is always present in the process of the second harmonic generation.

Acknowledgements

The authors acknowledge the support from the state grant number 3221/GF4, funded by the Ministry of Education and Science of the Republic of Kazakhstan.

References

[1] J.B. Pendry. Negative refraction makes a perfect lens // Phys. Rev. Lett. – 2000. – Vol. 85. –P. 3966.

[2] V.G. Veselago. The electrodynamics of substances with simultaneously negative values of ε and μ // Sov. Phys. Usp. – 1968. – Vol.10. – P. 509-514.

[3] M.A. Noginov. *et al.* Enhancement of surface plasmons in an Ag aggregate by optical gain in a dielectric medium // Opt. Lett. – 2006. – Vol 31. – P. 3022–3024.

[4] M.A. Noginov. *et al.* The effect of gain and absorption on surface plasmons in metal nanoparticles. // Appl. Phys. B – 2007. – Vol. 86. – P. 455-460.

[5] Zokan Jaksic, *et al.* Functionalization of plasmonic metamaterials utilizing metal–organic framework thin films // Phys. Scr. – 2012. – P. 014051.

[6] H. Gliemann, C. Wöll. Epitaxially grown metal-organic frameworks // Materials today. – 2012. – Vol. 15. – P. 110-116.

[7] A. Mauri. Kostiainen, Panu Hiekkataipale, Ari Laiho, *et.al.* Synthetic and biological nanoparticles combined to produce new metamaterials // Nature Nanotechnology. – 2013. – Vol. 8. – P. 52-56.

[8] W. Boyd. Nonlinear Optics.– New York:Academic Press, 2008. – P. 640.

[9] Y.R. Shen. The principles of non-linear optics. – New York: John Wiley Sons, 1984. – P. 563.

[10] Zh. Kudyshev, I.R. Gabitov, A. Maimistov. The effect of phase mismatch on second harmonic generation in negative index materials // Phys.Rev. A. – 2013. – Vol. 87. – P. 063840.

UDC 530.1

Electrical conductivity of silicon quantum nanowires

Z.Zh. Zhanabaev, T.Yu. Grevtseva[*], M.K. Ibraimov

Al Farabi Kazakh National University, NNLOT, al Farabi 71, 050040Almaty, Kazakhstan

[*]*e-mail:* Tatyana.Grevtseva@kaznu.kz

We suggest a new theory for the description of electrical conductivity of semiconductor quantum nanowires. We take into account that oscillations of quantum nanowires lead to their self-similar deformation, and because of interaction between nanowires they form fractal clusters. Electrical potential of these structures is described via nonlinear fractal measures. We conclude that current-voltage characteristics of quantum nanowires contain hysteresis loops with oscillations. This fact corresponds to existence of negative differential resistance due to multi barrier tunneling effect in the described fractal structures.Our theoretical results have been confirmed by results of corresponding specific experimental study of nanoscale wire-like structures in silicon.

Key words: silicon, quantum nanowire, tunneling effect, hysteresis, nonlinear fractal.
PACS numbers: 61.46.-w, 61.46.Km, 62.63.Hj, 73.63.-b.

1 Introduction

Silicon quantum nanowires (SiNWs) have been attracting considerable attention due to various application of nanowires in nanoelectronics, optoelectronics, sensor devices [1-6]. Microphotographs of SiNWs show sets of separated groups of nanowires. Each group contains several interacting nanowires. It can be explained by overlapping of wave functions of the nanowires. So, we can consider such structures as quantum nanowires.

At the present time singularities of electrical conductivity of quantum nanowires considered in theoretical and experimental studies on the base of Landauer’s theory [7, 8]. In a one-dimensional regular quantum wire density of states is inversely proportional to speed of electrons. In case of a single electron, electrical conductivity is a constant value expressed via the Planck constant and electron charge. This result follows from the Heisenberg's uncertainty principle also. Structure of quantum wires can be irregular,so, in this case we must take into account not only external potential between electrodes (“reservoirs”) but value of potential caused by internal heterogeneous distribution of electrons. According to [7] this potential is called the “scattering potential”, but its physical nature hasn’t been described. In order to define values of current we must integrate relations including probability density function of these potentials, and use different approximations of these relations: uneven (for example, via the Heaviside step function) and wave-like (classical). But irregular alternation of probability density function of distribution of electrons on energies is possible only near absolute zero. quasi-classical description can be used in case of motion of quantum particles with relatively big impulses in a potential field with small gradients. In our case these conditions are improbable. Effective mass and impulse of an electron in a semiconductor are substantially less than effective mass and impulse of a quasi-free electron in a metal. Nano-sized semiconductors have fractal structure with sharp variations of potential barriers. Semiconductor nanofilms can be characterized by existence of hierarchy of similar structures with fractal dimensions in range of spatial scales from 10 to 10^3 nanometers [9]. Results of recent studies show that electrical conductivity of semiconductor nanostructures is a non-monotone function, andcurrent-voltage characteristics of such structures contain areas with negative differential resistance and hysteresis cycle. So, the aim of our work is to construct a simple nonlinear theory for the description of electrical conductivity of semiconductor quantum nanowires accounting values of potential of internal fractal structures, and to compare the theoretical results with our experimental study of SiNWs.

2 Model of clustering of quantum nanowires and theory of electrical conductivity

Let us consider an ensemble of semiconductor nanowires. Diameter L of a nanowire is about sum of size of several atomic layers and the de Broglie wavelength λ of an electron. As usual, L is about 50 nanometers [1-6]. Nanowires can be considered as nonlinear objects because their properties depend on processes in the nanowires. Thermal fluctuations and non-uniform electric potential of boundary aggregation of molecules (ions) disturb shape of nanowires. The simplest and universal algorithm of nonlinear evolution of initially harmonic perturbations (leading to dynamical chaos) is doubling of period. Amplitude of perturbations decreases during a spatial period. The next period characterized by increasing of the amplitude. As a result, wave functions of two nanowires overlap each other (Figure 1). Next stages of evolution of the perturbations can lead to chaotic distribution of electrons in a space with cellular fractal structure. So, a fractal harness consisting of two wires can be formed in a direction perpendicular to the wire. A similar harness formed in three-dimensional space consists of three wires ($\pi^{d}/_{d} = \pi \approx 3$). Correlations of third and higher order are possible also, but probability of this case is low.

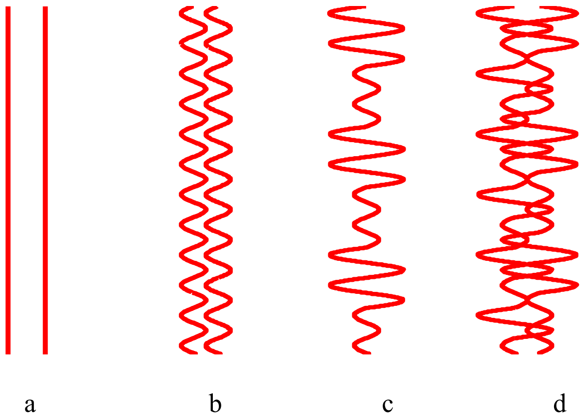

a) single wire, b) harmonic perturbations of wires, c) doubling of perturbation period of the single wire, d) forming of a harness with cellular structure consisting of two wires in the first cycle of doubling of perturbation period with phase shift.

Figure 1 – Model of clustering of quantum nanowires

So, we can take into account a possibility for realization of more complex cycles of overlapping of wave functions and existence of impurity atoms. This approach let to obtain an image of harness of nanowires with fractal structure similar to experimental data. Below we shall describe more complex evolution of perturbations than doubling of period.

3 Quantum electrical conductivity of a fractal nanowire

Let us consider a quantum wire with ideal contacts without scattering. Voltage between the contacts is U An electron moves inside of fractal cluster formed of quantum wires under the influence of potential $V(U)$. We shall describe the potential below. Current corresponding to a single electron is equal to product of density of states $g(E)$ in the energy range eV on speed of electrons $v(E)$ and value of elementary charge e:

$$I = g(E)\upsilon(E)e. \quad (1)$$

Let us define density of states for unit of length equal to distance between contacts via differential of impulse dP and the Planck constant h [7] as

$$g(E) = \frac{2dP(E)}{h} = \frac{2dE}{h\,{}^{dE}\!/_{dP}} = \frac{2}{h}\frac{dE}{\upsilon(E)} = \frac{2eV(U)}{h\upsilon(E)}. \quad (2)$$

Coefficient “2” in the Eq. 2 is necessary for taking into account the possibility of motion of electrons in two (opposite) directions. From Eqs. (1) and (2) we have

$$I = G_0 V(U),\ G_0 = \frac{2e^2}{h},\ \frac{1}{G_0} = R_0 = 12906\,\Omega, \quad (3)$$

where G_0 is fundamental conductivity. Value $G_0/2$ is called the quantum unit of conductivity, and $2R_0$ is quantum resistance. If conducting channel passes N electrons and M modes (one standing half-wave), the result follows from the Landauer’s theory can be written as [7]

$$G = G_0 \sum_{n,m}^{M} T_{n,m} N_{n,m}(E), \quad (4)$$

where $T_{n,m}$ is probability of transmissions from m – th mode of one contact to n – th mode of another contact, $N_{n,m}(E)$ is number of electrons on the level corresponding to full energy E of the m – th and n – th modes. For quantum nanowires $M = 1$ and by use of delta-symbol we have

$$\sum_{n,m}^{M} T_{n,m} N_{n,m}(E) = \delta_{n,m} N_{n,m}(E) = N(E). \qquad (5)$$

Let us designate relative values of potential $V(U)$ between clusters with numbers i and j as $V_{ij}(U)$, and probability of this relation as P_{ij}. Fractal clusters are located chaotically, so, value of total potential difference can be defined as potential difference between ends of a circuit consisting of K elements.

By analogy with Eq. (5) at $k = 1$ we have

$$\sum_{i,j}^{K} P_{ij} V_{ij}(U) = \delta_{ij} V_{ij}(U) = V(U). \qquad (6)$$

Function $V = V(U)$ called the “scattering potential” (according to [7]) in our case can be considered as a nonlinear fractal measure characterizing metastable states. We consider measure as a measurable additive value. As usual, fractal measure can be defined by scale of measurement δ depending on structure of an object. Structure of nanowires changes according to applied voltage U. Therefore, we must choose scales of measurement corresponding to variations of the measure as

$$\delta_U = \left|1 - \frac{V(U)}{U}\right|, \ \delta_V = \left|1 - \frac{U}{V(U)}\right|. \qquad (7)$$

Indexes at δ describe the determining variables. Values δ_U and δ_V can be used for the description of metastable threshold phenomena at $U \sim V$. We can describe the scattering potential via Eq. (7) and definition of nonlinear fractal measure leading to the Hausdorff’s formula for fractal dimension by the following way:

$$V(U,\delta_U) = V_0 \left(\left| 1 - \left| \frac{V(U)}{U} \right| \right| \right)^{-\gamma},$$

$$V(U,\delta_V) = V_0 \left(\left| 1 - \left| \frac{U}{V(U)} \right| \right| \right)^{-\gamma}, \qquad (8)$$

$$\gamma = D - d,$$

where D is fractal dimension of the set of values $V(U)$, d is its topological dimension. Eqs. (8) contain only difference between D and d. Therefore, these relations can be used for the description as geometrical as physical spaces. At $\gamma = 0$ we have $V(U) = V_0$ which is a non-fractal (for regular structures) value of $V(U)$.

We can use $V_0 = E_g$ as a rank value, where E_g is band-gap energy of silicon measured in electron-volts. Choice of $V_0 = E_g$ as a rank value can be explained by the fact that this value characterizes interruption of energy on boundaries of structures (Brillouin zones).

Equation (3) defines value of current in a regular (non-fractal) nanowire. Fractality is an integral characteristic. Electrical conductivity is a differential, local characteristic. Therefore, we use an expression for fractal measure for resistance $R(U)$ instead of R_0. In this case from Eqs. (3)-(8) we have the following system of equations for the description of current in a nanowire:

$$I(U) = \frac{V(U)}{R(U)}, \qquad (9)$$

$$V(U) = V_0 \left(\left| 1 - \left| \frac{V(U)}{U} \right| \right| \right)^{-\gamma}, \qquad (10)$$

$$R(U) = R_\lambda \left(\left| 1 - \left| \frac{U}{I(U)R(U) - V_0} \right| \right| \right)^{-\gamma}. \qquad (11)$$

Values of current influence on properties of nanowires, so, we can use difference between current and $V_0/R(U)$ as a determining variable in Eq. (11). Resistance R_λ depends on length of a fractal nanowire considered as fractal measure, and can be expressed via relative scale of length λ/L as

$$R_{\lambda} = R_0 \left(\frac{\lambda}{L} \right)^{-(D-d)}, \tag{12}$$

where λ is the de Broglie wavelength, L is size of an area including nanowires, $2R_0$ is quantum resistance. D is fractal dimension of an area ($D > 3$) including considered fractal wires ($d = 1$), therefore, $2 < (D - d) < 3$.

Fine structure of quantum nanowires can be described via relation for second generation of hierarchical structure of cluster potential as

$$V(U) = V_0 \left| 1 - \frac{V(U)}{V_0 \left| 1 - \frac{V(U)}{U} \right|^{-\gamma}} \right|^{-\gamma}. \tag{13}$$

4 Results of numerical analyses and experiment

All parameters of our theory have a certain physical meaning. So, we can choose values of these parameters according to a considered problem.

At first, let us define $V(U, \delta_U)$ according to Eq. (8). In order to choose value of the parameter $\gamma = D - d$ we take into account that generally d isn't equal to the greatest integer part of D. For a one-dimensional curve $V(U)$ d – 1,1 < D < 2 therefore, $0 < \gamma < 1$. $V_0 = E_g = 1.12$ eV for silicon. Curve $V(U, \delta_U)$ is non-monotone, there are several peaks at $U \geq V_0$. Amplitude of the peaks growths with increasing of γ (Figure 2).

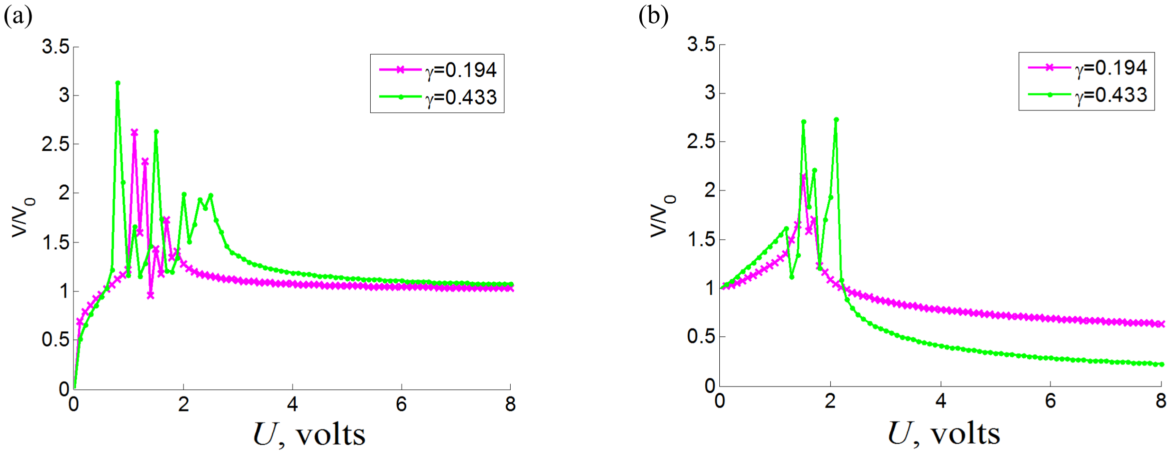

Figure 2 – Curves $V(U, \delta_U)$ and $V(U, \delta_V)$ for different γ according to Eqs. (8) at $V_0 = 1.12$ V.

$V_0 = E_g$ is maximal value of negative potential of an electron localizing in a cluster. So, values of modulus $V(U, \delta_U)$ should be considered as values of potential effecting on electron. Sign of the potential equals to sign of U (determining variable for relative scale of measurement). For correct choosing of determining variable of the required potential $V(U, \delta_U)$ at $U = 0$ we must take into account value of eigen potential barrier of the cluster $V(U = 0, \delta U) = V_0$.

Dependence $I = I(U)$ described by Eqs. (9)-(11) has sharp oscillations at $U \approx V_0$ and saturates at $U > V_0$ (Figure 3). Curves $I(U)$ are intersects each other at different γ_1 and γ_2. In the cross points one metastable state with parameter of fractal dimension γ_1 transfers to another metastable state characterized by γ_2. Hysteresis curves (universal physical phenomena in mediums with metastable states) are located between the cross points of curves $I(U)$.

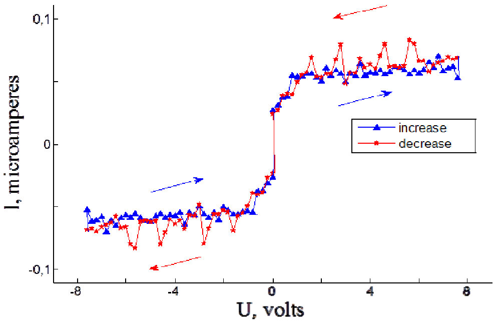

Figure 3 – Theoretical current-voltage characteristics of quantum nanowires for different γ at $R_\lambda = 28$ MΩ, $V_0 = 1.12$ B, γ: ▲ – 0.095, ★ – 0.128.

Electrical conductivity of a nanowire *G(U) = 1/R(U)* calculated by use of Eqs. (9)-(11) increases due to influence of external voltage U and described by corresponding growth of γ (Figure 4).

Main theoretical results obtained on the base of the stated above theory have been checked by our specific experiment. SiNWs were fabricated by well-known metal-induced chemical etching [5, 11, 12] according to the scheme shown in Figure 5. The method consists of three stages: deposition of solution of $AgNO_3$:HF as catalyst, chemical etching in H_2O_2:HF during 40 minutes, and removal of remains of metals in HNO_3. We used p-type crystalline silicon doped by boron as a substrate. Thickness of films is 300 mkm, crystallographic direction is (100), surface resistance of the substrate is 10 Ω·mm^2.

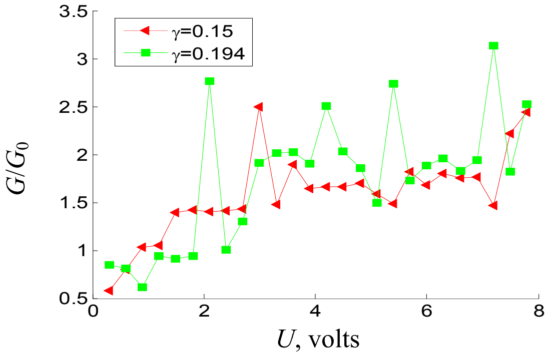

Figure 4 – Variation of electrical conductivity of a nanowire vs voltage for different γ.

$$G_0 = \frac{1}{R_0} = \frac{1}{28\,M\Omega} = 4.3478 \cdot 10^{-8}\,S.$$

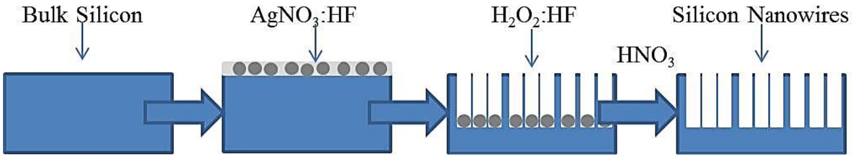

Figure 5 – Scheme for metal-induced chemical etching

We studied the fabricated films by atomic-force microscope. Results of this study are shown in Figure 6.

Results of the study show that length of the considered wire-like structures is about 1÷5 micrometers (Figure 6a), and diameter is 25÷200 nanometers (Figure 6b). Figure 6c shows that distance between sets of wire-like structures is about 100÷500 nanometers.

In case of vertical nanowires metal electrodes must be connected to two ends of SiNWs in order to measure value of resistance of the nanowires. Metal electrode must be closely connected to the end of nanowire. For this aim we used of surface-contact structures shown in Figure 7. Experimental dependence *I(U)* (Figure 8) is a hysteresis curve with a set of loops.

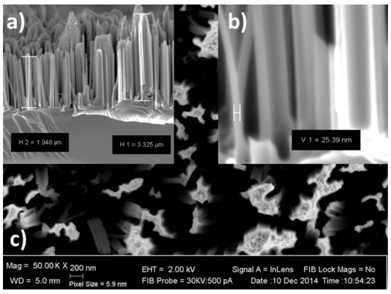

Figure 6 – AFM microscopic image of SiNWs.
a) lateral view (medium zoom), b) lateral view on separate nanowires (maximal zoom), c) top view.

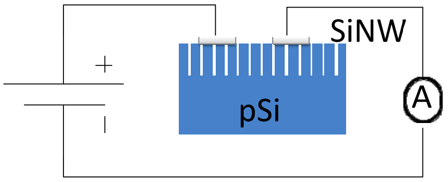

Figure 7 – Scheme of electrical contacts of the sensor with vertical SiNWs (vertical contact).

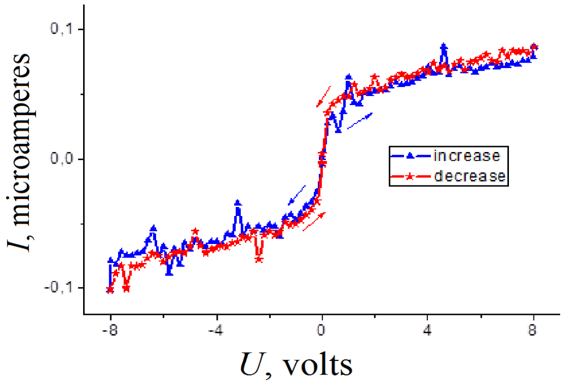

Figure 8 – Experimental current-voltage characteristics of SiNWs

A similar dependence $I(U)$ follows from Eqs. (9)-(13) (Figure 9). According to Eq. (10) at the absence of external field value of potential of cluster affecting on electrons $V(U) – 0$, therefore, $I|_{U=0} – 0$. Growth of U leads to increasing of $V(U)$, resistance of quantum nanowire decreases (according to Eq. (11)), and $I(U)$ increases sharply. At further growth of U value of $V(U)$ tends to V_0, and current saturation is observed. But at $U – V_0$ function $V(U)$ became a nonlinear fractal measure, and $I(U)$ pulses. It indicates to existence of multi-barrier tunneling effect leading to negative differential resistance at $V(U) – V_0$.

In non-fractal crystal ($\gamma = 0$) $V = V_0|_{R_0}$ at $0 < U < V_0$, and inclination of $I(U)$ doesn't change. It's equivalent to using of $V(U, \delta_V)$ in Eq. (8), i.e. we use $V(U) – V_0$. as a main variable (instead of U). Therefore, we have $I = V(U) – V_0/R_0$ at $U = 0$. For more precision description of the dependence $I(U)$ we can take into account second generation of fractal hierarchy of potential according to Eq. (13). In this case we can notice an insignificant growth of inclination of the curve $I(U)$ relative to abscissa axis in comparison with this dependence shown in Figure 3 at the same γ.

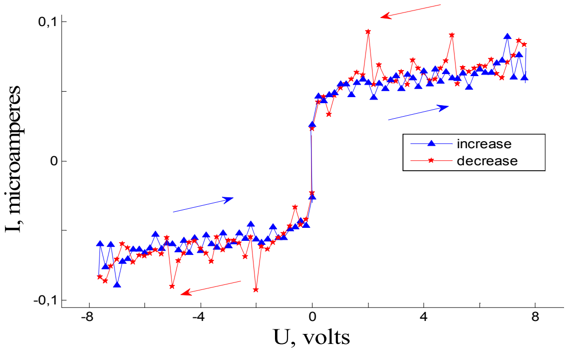

Figure 9 – Theoretical current-voltage characteristics of SiNWs with taking into account their fractal hierarchy according to Eqs. (9)-(13) for different γ at $R_\lambda = 28\,\text{M}\Omega$, $V_0 = 1.12\,\text{eV}$, γ : ▲ – 0.095, ● – 0.128.

Hysteresis in current-voltage characteristics have been observed in different experiments. For example, electrical conductivity of Au/pentacene/Si-nanowire arrays has been studied in [4]. Existence of negative differential resistance has been registered in recent works, for example, in current-voltage characteristics of nanowires and nanobelts *ZnO* [13, 14]. But quantitative descriptions of singularities of these effects haven't been suggested in the works.We suppose that taking into account the fractal structure of nonlinear quantum nanowires let us to obtain the new results.

Thus, our theoretical results obtained via Eqs. (9)-(13) and experimental data adequately describe main physical singularities of electrical conductivity of semiconductor quantum nanowires.

5 Conclusions

Electrical conductivity of nanoscale wire-like structures depends on value of internal potential of fractal clusters. Scattering potential of the clusters can be considered as a nonlinear measure defining by value of external voltage.

Fractality of geometry of wire-like formations leads to appearance of multi-barrier effects in nanoscale wires grown on surfaces of homogeneous films (silicon). Because of this fact the current-voltage characteristic of SiNWs has areas with negative differential resistance and hysteresis loops. Previously such effects have been observed in silicon compounds and heterostructures, but in the present work we describe this phenomena in pure silicon. Results of the present work can be used for perfection of electronic memory schemes, devices of nanoelectronics and optoelectronics.

References

[1] V. Sivakov, and S. Christiansen. Novel Discovery of Silicon // Journal of Nanoelectronics and Optoelectronics. – 2012. – Vol. 7. – P. 1-7.

[2] J.Zh. Chew, L. Lijie. A Discrete Memristor Made of ZnO Nanowires Synthesized on Printed Circuit Board // Material letters. – 2013. – Vol. 91. – P. 248-300.

[3] R. Zang, Sh.U. Yuldashev, J.C. Lee, V.Sh. Yalishev, T.W. Kang, D.J. Fu. Memristive behavior of ZnO/NiO stacked heterostructure // Microelectronic Engineering. – 2013. – Vol. 112. – P. 31-34.

[4] H.Y. Tsao, Y.J. Lin. Resistive Switching Behaviors of Au / Pentacene / Si-Nanowire Arrays / Heavily Doped n-type Si Devices for Memory Applications // Applied Physics Letters. – 2014. – Vol. 104. – Iss. 5. – P 053501.

[5] X. Li, P.W. Bohn. Metal-assisted chemical etching in HF / H2O2 produces porous silicon // Appl. Phys. Lett. – 2000. – Vol. 77. – P. 2572-1-5.

[6] Zh. Huang, N. Geyer, P. Werner, J. Boor, and Gösele U. Metal-Assisted Chemical Etching of Silicon: A Review // Advanced Materials. – 2011. – Vol. 23. – P. 285.

[7] P.F. Bagwell, T.P Orlando. Landauer's Conductance Formula and its Generalization to Finite Voltages // Phys. Rev. B. – 1989. – Vol. 40. – P. 1456.

[8] A. Mehonic], A. Vrajitaarea, S. Cneff, S. Hudziak, C. Labbe, R. Rizk, M. Pepper, and A.J. Kenyon. Quantum Conductance in Silicon Ovide Resistive Memory Devices // Scientific Reports / 3 : 2708 | DOI: 10.1038/srep02708. – 2013. – P. 1-8.

[9] Z.Zh. Zhanabaev, T.Yu. Grevtseva. Physical Fractal Phenomena in Nanostructured Semiconductors // Reviews in Theoretical Science. – 2014. – Vol. 2. – No 3. – P. 211-259.

[10] Z.Zh. Zhanabaev, T.Yu. Grevtseva, T.B. Danegulova, G.S. Assanov. Optical Processes in Nanostructured Semiconductors // Journal of Computational and Theoretical Nanoscience. – 2013. – Vol. 10. – No 3. – P.673-678.

[11] R. Juhasz, N. Elfstrom, J. Linnros. Controlled fabrication of silicon nanowires by electron beam lithography and electrochemical size reduction // Nano Lett. – 2005. – Vol. 5. – No 2. – P. 275-280.

[12] C.M. Hsu, S.T. Connor, M.X. Tang, Y Cui. Wafer-scale silicon nanopillars and nanocones by Langmuir-Blodgett assembly and etching // Appl. Phys. Lett. – 2008. – No 93. – P. 133109.

[13] R. Könenkamp, C. Robert. Word, and Schlegel C.Vertical nanowire light-emitting diode // Applied Physics Letters. – 2004. Vol. 85. – No 24. – P. 6004-6008.

[14] Ch. Lao, Li Yi, C.P. Wong, Z.L. Wang. Enhancing the Electrical and Optoelectronic Performance of Nanobelt Devices by Molecular Surface Functionalization // Nano Letters. – 2007. – Vol. 7, No 5. – P. 1323-1328.

UDC 551.5

Climate changing and non-equilibrium atmosphere

Nurgaliyeva K.*, Tlekova K.

Al-Farabi Kazakh National University, IETP, al-Farabi 71, 050040 Almaty, Kazakhstan

**e-mail: kdungen@rambler.ru*

This work is a first step to solve the problem on creation of the theory of evolution of non-equilibrium open systems. The mean factors forming atmospheric structures are radiation fluxes. So in order to understand atmospheric evolutional processes it is a necessary to consider atmospheric gas in continuity with radiation. This problem couldn't be solved in the frames of traditional gas dynamics equations because of dissipative structures in any systems including atmosphere and radiation causes by entropy production and interchange and this don't describing in the frames of traditional gas dynamics. But for this aim we could use more complex non-equilibrium thermodynamics equations which taking into account exchange processes in such systems. The behavior of wave disturbances in non-equilibrium medium: atmospheric gas – solar radiation taking into account atmospheric structures and radiation flux interrelations was investigated in this work. The dispersion relation of acoustic-gravity waves was found from reductive atmospheric gas – solar radiation system dynamic equations set in the frames of non-equilibrium thermodynamics. Calculations show that the taking into account of solar radiation leads to slowly decreasing of pressure with height than without taking it into account. The maximum deviation of pressure comes to heights of 10-15 km and amounts about 3 percents. The dependence of AGW spectra deviation in non-equilibrium atmosphere from the spectra in equilibrium atmosphere from the height was estimated. It was found that in the frames of non-equilibrium spectra shifts into high-frequency region. Numerical calculations also shows that in the heights of ionosphere these effects shown up sharply at transitionally times at abrupt change of solar energy influx into atmosphere. Analysis of pressure variations shows the experimental prove of existing of obvious trend of spectra shift into high-frequency region of daytime spectra relatively to nighttime spectra and the difference made 10 percents and proves the correctness of theoretical calculations.

Key words: Climate changing, non-equilibrium atmosphere, gas – solar radiation, radiation flux interrelation.
PACS numbers: 92.70.Cp, 92.60.Vb

1 Introduction

There is a destruction of climatic machine on the Earth. Thawed the Arctic and Antarctic ice, Tien Shan, Alps, Greenland glaciers melt away and the mean temperature of Earth grows [1,2]. Moreover the quantity of weather anomalies sharply increased. The rate of climate change on Earth is higher than thought scientists. In thear prognosis on Arctic ice thawing researches mistakes approximately for 30 years. Today the danger of disappearance concerns not only living creatures of earth but even continents [3-5].

In accordance with known laws of non-equilibrium dynamics all these signs significant for bifurcation change. After crossing of bifurcation point climate wouldn't be restored. It would have rather different characteristics than now. It creates serious danger for humankind. That why the mean problem of mankind is to understand the causes and mechanism of climate changing in order to take the necessary steps on prevention or even decreasing of catastrophic aftermath.

For nowadays we for certain know that there are two causes of these phenomena. First bind with natural circle climate changes. The second depend on anthropogenic activity. And it is not ruled out that these causes overlay. But we couldn't say that kind of scenario would realize actually.

There is a reason to say that the climate changing course of anthropogenic activity. Really the fact of atmosphere existing related with existence of live on the Earth [6]. The modern atmosphere composition made by living organism. They change original Earth climate. On the first level of development atmosphere of Earth haven't free oxygen, it was composition of carbon dioxide. It hence on chemical composition of iron compound of these periods. Approximately 1.8 billion years ago (the Earth age is about 40 billion years) in the result of microorganisms activity the oxygen exists in atmosphere. It's lead to existing of ozone layer at the heights of 20—50 km. As a result the living organisms which could live out of solar radiation have a possibility to spread over all the Earth and having an advantages to survive change the atmosphere composition some more.

For the advantage of anthropogenic mechanism of climate changing testify the striking coincidence of annual planetary temperature changing rate with carbon dioxide consantration change rate. [7,8] The serious reason for assumption on curtail human role in climate changing is the increasing of observing weather fluctuations in different Earth regions. It's very difficult to explain the rate of this change by natural circles. That's why most of scientists thought that the climate changing caused by human activity.

World public already now tries to make some efforts against climate changing. But it's very difficult to wait efficiency of any efforts when we don't know the causes of running processes. Today science limited by observation of existing processes and by mapping empiric prognosis which only could gave epignosis. The existing mathematical atmospheric models adopted for numerical weather calculation. They made weather prognosis but couldn't answer the question on climate changing. It is a due to rough atmosphere parameters used in numerical calculations. That's why it's important to reveal the mechanisms of weather and climate formation. Without knowing it we couldn't answer the question on prevention measures.

Any atmospheric changes somehow depend on external parameters variations: solar activity variation, magnetic storms, anthropogenic carbon dioxide fluxes and so on. In order to understand their influence to atmosphere we should to take into account the openness of atmosphere that's mean its non-equilibrium. We should to know how external parameters variations changes influence on atmospheric processes. But today we practically don't understand mechanisms that define the dependence character of non-equilibrium systems dynamics at external conditions and system parameters changes. There aren't necessary fundamental theories which could help to create evolutional mathematical atmosphere models. These set a problem for science *to create the theory of evolution of non-equilibrium open systems*. [9-11].

2 Main body

The mean factors forming atmospheric structures are radiation fluxes. They cause such dissipative strictures as ionosphere, ozone layer, temperature and other atmospheric inhomogeneities. These structures are non-equilibrium since their existence due to constant interchange of energy between atmosphere and cosmic space. So *in order to understand atmospheric evolutional processes it is a necessary to consider atmospheric gas in continuity with radiation.* This problem couldn't be solved in the frames of traditional gas dynamics equations because of dissipative structures in any systems including atmosphere and radiation causes by entropy production and interchange and this don't describing in the frames of traditional gas dynamics. But for this aim we could use more complex non-equilibrium (non-equilibrium) thermodynamics equations which taking into account exchange processes in such systems. Of course this essentially complicated the problem but we couldn't find simpler path for understanding of evolutional processes.

The systems of atmosphere dynamic equations in the frames of non-equilibrium (non-equilibrium) thermodynamics are written as:

$$\frac{\partial}{\partial t}\rho = -\nabla\rho\vec{v}\,, \tag{1}$$

$$\rho\frac{\partial}{\partial t}\vec{v} + \rho(\vec{v}\nabla)\vec{v} = -\nabla P + \rho\vec{g}\,, \tag{2}$$

$$\frac{\rho c_V}{P}\frac{dP}{dt} - c_p\frac{d\rho}{dt} + \frac{1}{T}\{(\nabla L) - \int \chi'_a(\nu)\rho I_\nu d\nu + (divJ_e) = 0\,, \tag{3}$$

$$-\frac{dJ}{dz} + \mu\rho J = 0\cdot \tag{4}$$

where: t – time; ρ – atmospheric gas density; T – temperature; $\vec{v}$ – gas transference velocity; P – pressure; g – acceleration of gravity; c_v, c_p – heat capacities at constant volume and pressure correspondingly; I_v– photon beam with frequency v; $\chi`_a(v)$ – specific radiation absorption coefficient; L -

thermal flux and $\nabla L = -\kappa \Delta T$; κ – thermal conductivity coefficient; J_e – atmospheric gas thermal emission; μ – average coefficient of solar radiation absorption. The flow of solar radiation J is directed downward.

Calculations showed that the consideration of atmosphere as non-equilibrium system: non-equilibrium atmosphere considering as interacting medium – atmospheric gas and incoming and outgoing radiation flow leads to instability of atmospheric parameters for the radiation parameters changes (Fig.1). Calculations showed that the taking into account of solar radiation leads to slowly decreasing of pressure with height in comparison with the case without taking into account of solar radiation. The maximum deviation of pressure takes place at heights of 10-15 km with amounts about 3 percents (Fig. 2). The atmospheric parameters defined on the basis of existing models of atmosphere.

Calculations were done for different means of albedo and radiation absorption coefficients. It was found that in the frames of parameters allowed values obtained temperature and density profiles essentially depend on surface temperature, absorption coefficient and albedo. So non-equilibrium atmospheric background model calculations shows that atmosphere is extremely unstable for radiation parameters changing (Fig. 3).

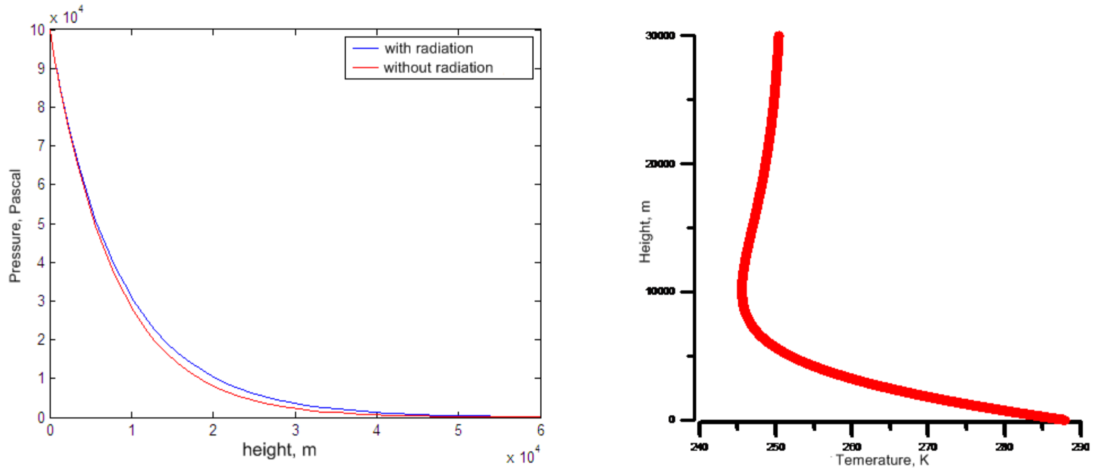

Figure 1 – Pressure and temperature profile

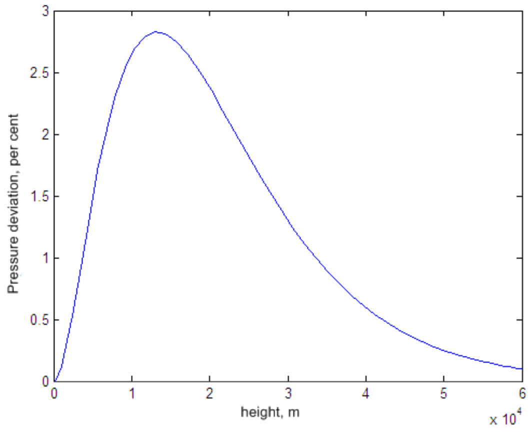

Figure 2 – Deviation from barometric formula at radiation consideration

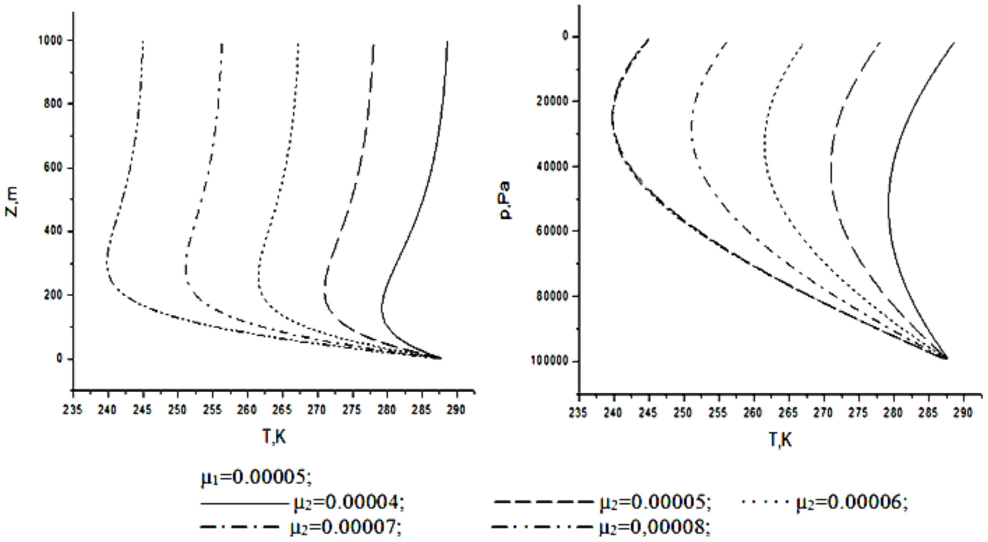

Figure 3 – Dependence of temperature profile on on surface temperature, absorption coefficient and albedo changes

The non-equilibrium spectrum of atmospheric oscillations was calculated based on the set of equations of non-equilibrium thermodynamics (1)-(4) written taking into account the interaction between the atmospheric gas and radiation. The set includes equations of continuity, energy, and momentum. The energy equation includes the terms related to the interaction of the atmospheric gas with solar radiation and thermal conductivity and radiation of the atmosphere. The set of gas dynamic equations is supplemented with the simplified equation for solar radiation flux absorbed by the atmospheric gas. Solar radiation flux absorbed by the atmosphere and atmospheric density are interrelated quantities. Therefore, all four equations are self-consistent.

The dispersion equation corresponding to the linearized equations of the set (1)–(4) for the non-equilibrium spectrum of atmospheric gas natural oscillations has the form

$$w^4-\frac{4\sigma T_0^3}{\rho_0 c_V}k_z w^3-g\gamma\left(Hk^2-ik_z\right)w^2+\frac{4\sigma T_0^3 g\gamma}{\gamma\rho_0 c_V}ik_z\left(iHk^2+k_z\right)w+$$

$$+\frac{\mu c^2}{\gamma T_0 c_V}\frac{ik_z J_0 k^2}{ik_z-\mu\rho_0}w+g^2(\gamma-1)k_x^2=0 \qquad (5)$$

Here i – imaginary unit; w – harmonic frequency, k_x, k_z - are the corresponding wavevector harmonics along the x, z axes, and $k^2=k_x^2+k_z^2$; $\gamma=\frac{c_p}{c_V}$; $H=c^2/(g\gamma)$ – is the so-called height of the homogeneous atmosphere.

If we omit the fourth equation in the set (1)–(4) and neglect three last terms in the energy equation, then the dispersion equation for AGWs in the equilibrium atmosphere [Gershman, 1974] will correspond to the obtained set of equations. The same dispersion equation can be obtained immediately from (5) by rejecting all even terms related to energy exchange between gas and radiation.

The dependence of difference between AGW spectra for non-equilibrium and equilibrium atmosphere on height was estimated. It is found that for non-equilibrium atmosphere AGW spectra is shifted into high-frequency region (fig. 4). Also numerical calculations show that at the heights of ionosphere these effects become brighter at transition times, when the solar energy input changes abruptly (fig 5).

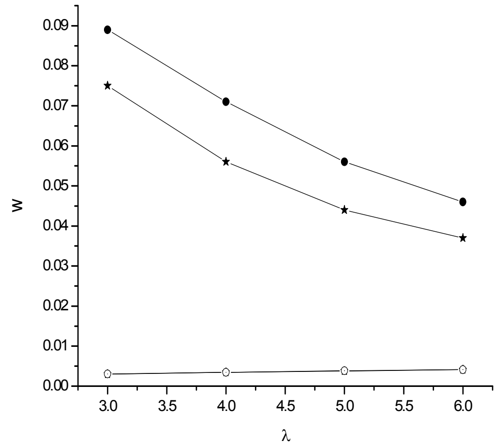

Figure 4 – Variations in the oscillation frequency ω vs. λ_z in the nonequilibrium (non-equilibrium) daytime (circles, line 3) and nighttime (asterisks, line 2) atmosphere and in the equilibrium case (line 1) calculated using the background values of the parameters at an altitude of h = 50 km.

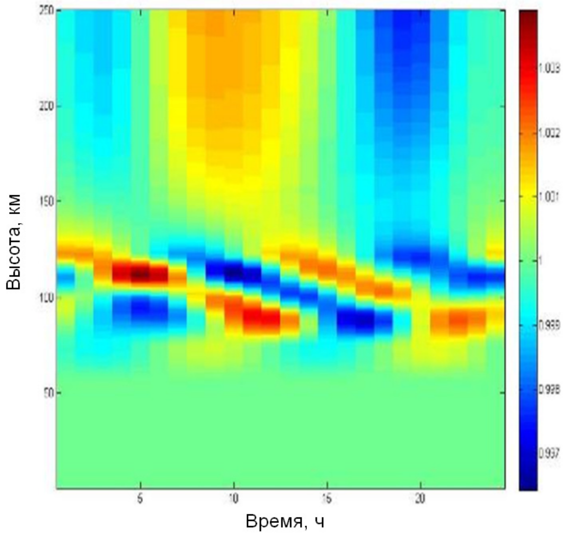

Figure 5 – Ratio of non-equilibrium and equilibrium spectrum for heights 0-250 km.

To calculate the equilibrium spectrum of oscillations, we used the traditional equation of the AGW spectrum [12]. As was noted above, this equation can be obtained immediately from (5) by eliminating the terms related to energy exchange between radiation and the atmospheric gas. The dispersion relation was numerically analyzed for different conditions: in the presence of solar radiation in the atmosphere and without this radiation, as well as for the equilibrium case at different atmospheric altitudes. The temperature values were taken from the existing atmosphere/ionosphere models up to 250 km. The average temperature difference in daytime and nighttime hours is approximately 20 K in the selected altitude interval. According to these results, in both cases the oscillation spectrum shifts into the HF spectral region with increasing temperature.

3 Conclusions

Thus, according to the numerical estimates, the presence of non-equilibrium in the atmospheric gas should lead to a shift of the atmospheric natural oscillation spectrum. The difference of the atmospheric temperature in daytime and nighttime hours for the equilibrium model of the atmospheric gas cannot result in such a spectrum shift. Therefore, an experimental detection of the shift of the atmospheric natural oscillation spectrum will be a necessary argument for the substantial role of non-equilibrium in the dynamics of the atmosphere.

To confirm the theoretically founded spectra shifts into high-frequency region, the analysis of pressure variations for August, September and December of 2002 measured on high-mountain station of cosmic rays of Ionosphere Institute, Almaty, Kazakhstan and Ukraine station ”Academic Vernadskii”, Antarctica was made [13]. The analysis proved the existing of obvious trend of daytime spectra shift into high-frequency region relatively to nighttime spectra at about of 10 percents. The analysis of ionospheric data for Mach, June, September and December of 2005 on Ukraine station ”Academic Vernadskii”, Antarctica also proved obtained theoretical results for the ionosphere heights (Fig. 6).

As further investigations on this field it should be studied the interrelation of cosmic factors variations with dynamical processes on Earth atmosphere on the basis of open non-equilibrium systems theory and experimenta data of radiation fluxes in atmosphere

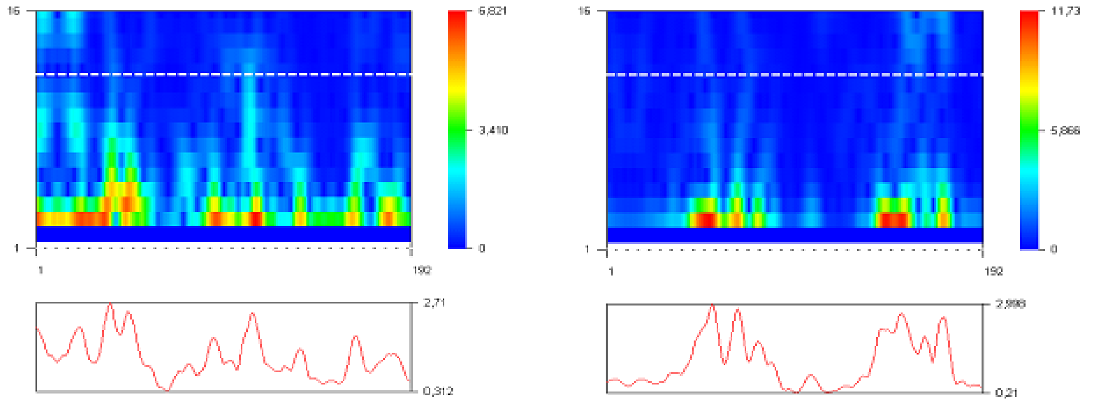

а) March **б) June**

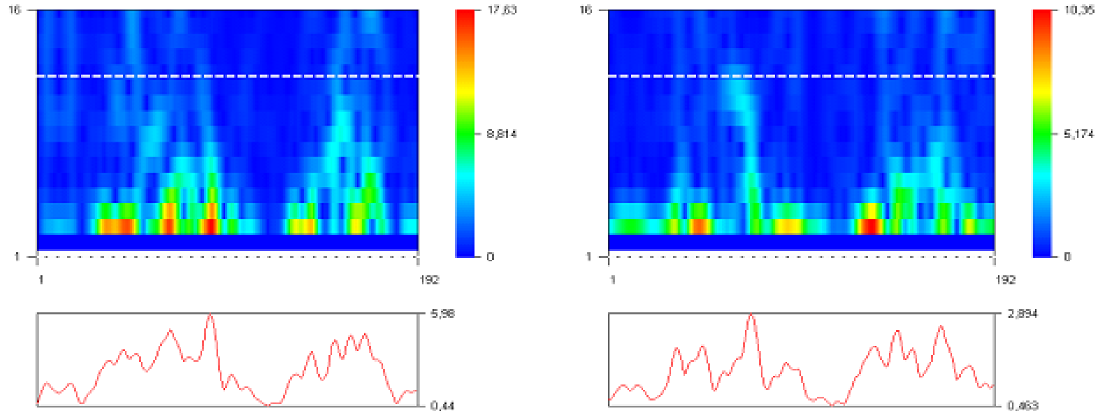

в) September **г) December**

Figure 6 – Spectrogram of ionosphere data

Acknowledgments

We are grateful to the Ukrainian Antarctic Center for presented meteorological data from Akademik Vernadsky station. The participation of the researchers of RI NAN Ukraine in this work was partially supported by NIR “Resonansy” UATs MON Ukraine

Research was made in the frames of projects “Development of non-equilibrium atmosphere researches”, reg. num. 0112PK00294

References

[1] D. Coumou, A. Robinson, S. Rahmstorf. Global increase in record-breaking monthly-mean temperatures. Climatic Change (online) [doi:10.1007/s1 0584-012-0668-1] Weblink to the article: http: // link.springer.com/article/10.1007/s10584-012-668-1, 2013.

[2] Paul Edwards. A Vast Machine: Computer Models, Climate Data, and the Politics of Global Warming. Cambridge, MA: MIT Press, 2010.

[3] Tobias Bolch. Climate change and glacier retreat in northern Tien Shan (Kazakhstan/Kyrgyzstan) using remote sensing data // Global and Planetary Change. – 2008. – Vol. 61.

[4] Kerry Emanuel. Increasing destructiveness of tropical cyclones over the past 30 years // Nature, Letter. – 2005. – Vol. 4364.

[5] D.A. Stainforth, T. Aina1, C. Christensen, et. al. Uncertainty in predictions of the climate response to rising levels of greenhouse gases // NATURE. – 2005. – Vol. 433.

[6] B.M. Smirnov. Ecological problems of earth. Uspehi phizicheskih nauk. – 1975. – Vol. 117. – Issue. 2. – P. 313-322.

[7] National Research Council: Global Emissions | U.S. Emissions.

[8] James Hansen, Larissa Nazarenko, Reto Ruedy, Makiko Sato, Josh Willis, Anthony Del Genio, Dorothy Koch, Andrew Lacis, Ken Lo, Surabi Menon, Tica Novakov, Judith Perlwitz, Gary Russell, Gavin A. Schmidt, Nicholas Tausnev. Earth's Energy Non-equilibrium: Confirmation and Implications. www.sciencemag.org // SCIENCE. – 2005. – Vol. 308.

[9] N. Essex. Radiation and Irreversible Thermodynamics of Climate // J. Atmos. Sci. – 1986. – Vol. 41 (12). – P. 1985–1991.

[10] M.N. Izakov. Self-Organization and Information on Planets and in Ecosystems // Usp. Fiz. Nauk. – 1997. – Vol. 167 (10). – P. 1087–1094.

[11] Stanislaw Sieniutycz, Henrik Farkas. Variational and Extremum Principles in Macroscopic Systems // Elsevier Science, Oxford. – 2004. – P. 791.

[12] B.N. Gershman. Ionospheric Plasma Dynamics. Nauka, Moscow, 1974.

[13] V.P. Antonova, K.E. Dungenbaeva, A.V. Zaliaovskii, A.S. Inchin, S.V. Kryukov, V.M. Somsikov, Yu.M. Yampol'skii. Difference between the spectra of Acoustic Gravity Waves in Daytime and Nighttime Hours due to Nonequilibrium Effects in the atmosphere // Geomag. & Aeron. – 2006. – Vol. 46. – P. 101-109.

UDC 533.9

Dynamic structure factor of non-ideal one-component plasmas

Yu.V. Arkhipov[1], A. Askaruly[1], A.E. Davletov [1], Z. Donkó[2],
D. Dubovtsev[1*], P. Hartmann[2], I. Korolov[2], I.M. Tkachenko[3]

[1]*Al-Farabi Kazakh National University, IETP, al-Farabi 71, 050040 Almaty, Kazakhstan*
[2]*Institute of Solid State Physics and Optics, Wigner Research Centre for Physics,*
Hungarian Academy of Sciences, 1525 Budapest, POB. 49, Hungary
[3]*Departamento de Matemática Aplicada, Universidad Politécnica de Valencia,*
Camino de Vera s/n, 46022Valencia, Spain
e-mail.denis.dubovcev@gmail.com

The dynamic characteristics of non-ideal Coulomb one-component plasmas are studied within the moment approach. In the work five odd moments were considered, whereas even moments are equal to zero, since the distribution functions is symmetrical in relation to the frequency. An empirical expression for the collective mode dispersion is proposed in terms of the characteristic frequencies. These characteristic frequencies are also used to obtain a Nevanlinna parameter-function. Our results on the dynamic structure factor satisfy the sum rules and other exact relations automatically. A quantitative agreement is obtained with numerous simulation data on the plasma dynamic properties, including those on the dispersion of collective modes.

Key words: dynamic structure factor, method of moments, peak position intervals.
PACS numbers: 52.27.Gr, 05.20.Jj.

1 Introduction

The one-component plasma is a simplified version of real physical systems ranging from electrolytes and charged stabilized colloids [1], laser-cooled ions in cryogenic traps [2] to dense astrophysical matter in white dwarfs and neutron stars [3].

The aim of this paper is the investigation of electrodynamic properties of Coulomb one-component plasmas (OCPs). It is a classical system of a single species of *N* point particles of charge *Ze* and mass m that interact via a pair potential with a uniform background of neutralizing charge.

Hence, the interaction potential in a OCP is the Coulomb potential:

$$\varphi(r) = \frac{(Ze)^2}{r}. \quad (1)$$

In an equilibrium state at a temperature T, the OCP is fully characterized by only one dimensionless coupling parameter Γ, which is approximately the ratio of the potential energy between two ions to the average thermal (kinetic) energy of an ion:

$$\Gamma = \frac{(Ze)^2}{ak_BT}, \quad (2)$$

where $a = (3/4\pi n)^{1/3}$ is the average inter-particle distance called the Wigner-Seitz radius [4].

In this paper, the OCP dynamic properties are studied within the moment approach based on sum rules and other exact relations, see [5,6] and references therein, and comparison is successfully carried out with the simulation data.

2 Method of moments: mathematical background

Consider five convergent sum rules which are frequency power moments of the system dynamic structure factor (DSF):

$$S_\nu(k) = \frac{1}{n}\int_{-\infty}^{\infty} \omega^\nu S(k,\omega)d\omega, \ \nu = 0,1,2,3,4. \quad (3)$$

All odd-order moments vanish since, in a classical system, the DSF is an even function of frequency. The method of moments is, generally speaking, capable of handling any number of convergent sum rules. In two-component plasmas, though, all higher-order frequency moments diverge which can be attributed to and understood [7] on the basis of the exact asymptotic form of the imaginary part of the dielectric function [8]. There is no such clear theoretical result for the model system to be dealt with here and, thus, it is simply impossible to presume that the three first even order moments are the only convergent even order frequency sum rules. However, the ambiguity of higher-order frequency moments, related to our scarce knowledge of the triple and, presumably, higher-order correlation functions, remains insuperable nowadays and can only impede our understanding of the physical processes to be described below.

The zero-order moment is the static structure factor (SSF):

$$S_0(k) = S(k). \tag{4}$$

The second moment is the f-sum rules:

$$S_2(k) = \omega_0^2(k) = \omega_p^2\left(\frac{k^2}{k_D^2}\right) = \omega_p^2\left(\frac{q^2}{3\Gamma}\right). \tag{5}$$

The fourth moment is equal to:

$$S_4(k) = \omega_p^2\omega_0^2(k)\left\{1 + \frac{3k^2}{k_D^2} + U(k)\right\} = \omega_p^2\omega_0^2(q)\left\{1 + \frac{q^2}{\Gamma} + U(q)\right\}. \tag{6}$$

Here $q = ka$, $\omega_p = \sqrt{4\pi ne^2/m}$ refers to the plasma frequency, and $k_D = \sqrt{4\pi nZ^2e^2\beta}$ is the Debye wavelength, m being the ion mass. The last contribution to the fourth moment is due to the ion-ion interactions in the OCP, while the second term represents the Vlasov correction to the ideal-gas dispersion relation of the plasmon mode.

The Nevanlinna formula of the classical theory of moments [9,10] expresses the response function

$$S(k,z) = -\frac{1}{n}\frac{E_3(k,z)+Q(k,z)E_2(k,z)}{D_3(k,z)+Q(k,z)D_2(k,z)} \tag{7}$$

in terms of a Nevanlinna class function $Q = Q(k,z)$, analytic in the upper half-plane $\mathrm{Im}\, z > 0$ with a positive imaginary part: $\mathrm{Im}\, Q(k,\omega + i\eta) > 0, \eta > 0$. The function $Q(k,z)$ should additionally satisfy the limiting condition:

$$\lim_{z\uparrow\infty}\frac{Q(k,z)}{z} \to 0,\ \mathrm{Im}\, z > 0 \tag{8}$$

Furthermore, the polynomials $D_j(k,z), j = 0,1,2,3$, orthogonal with respect to the distribution density $S(k,\omega)$ together with their conjugate counterparts $E_j(k,z), j = 0,1,2,3$, determined as

$$E_j(k,z) = \int_{-\infty}^{\infty}\frac{D_j(k,\omega)-D_j(k,z)}{\omega - z}S(k,\omega)d\omega\,, \tag{9}$$

have real coefficients and their simple real zeros alternate. A rather routine renormalization casts these polynomials as:

$$\begin{gathered}D_0 = 1, D_1 = z, D_2 = z^2 - \omega_1^2(k), D_3 = z^3 - z\omega_2^2(k),\\ E_0 = 0, E_1 = S_0(k), E_2 = zS_0(k), E_3 = S_0(k)\left(z^2 + \omega_1^2(k) - \omega_2^2(k)\right).\end{gathered} \tag{10}$$

The frequencies $\omega_1^2(k)$ and $\omega_2^2(k)$ are defined by the respective ratios of the moments $S_\nu(k)$ [6] and are determined by the system static characteristics:

$$\omega_1^2 = \omega_1^2(k) = \frac{S_2(k)}{S_0(k)},\ \omega_2^2 = \omega_2^2(k) = \frac{S_4(k)}{S_2(k)}. \tag{11}$$

Therefore, the DSF can be rewritten as:

$$S(k,\omega) = \frac{n}{\pi}\frac{S_0\omega_1^2(\omega_2^2 - \omega_1^2)\mathrm{Im}Q(k,\omega)}{\left(\omega(\omega^2 - \omega_2^2) + \mathrm{Re}Q(k,\omega)(\omega^2 - \omega_1^2)\right)^2 + \left(\mathrm{Im}Q(k,\omega)(\omega^2 - \omega_1^2)\right)^2} \tag{12}$$

3 Method of moments: new developments

a) Peak position intervals

In the present work we approximate the Nevanlinna interpolation function Q(q, z) by its static value:

$$Q(k,0) = ih(k),\ h(k) > 0. \tag{13}$$

In this case, the DSF expression (12) simplifies:

$$\mathrm{S}(\mathrm{k},\omega) = \frac{\mathrm{n}}{\pi}\frac{\mathrm{S}_0\omega_1^2(\omega_2^2-\omega_1^2)\mathrm{h}(\mathrm{k})}{\left(\omega(\omega^2-\omega_2^2)\right)^2+\left(\mathrm{h}(\mathrm{k})(\omega^2-\omega_1^2)\right)^2}. \tag{14}$$

The peak of the DSF corresponds to a propagating plasmon mode in the system. Mathematically, the presence of a peak implies that the expression (14) has a maximum value. After some analysis of the extrema of (14), we obtained an expression for *h(k)*:

$$\mathrm{h(k)} = \sqrt{\frac{\omega_2^4 - 4\omega_2^2\Omega^2 + 3\Omega^4}{2(\omega_1^2 - \Omega^2)}}, \qquad (15)$$

where Ω is the DSF peak frequency, i.e. the collective mode dispersion.

In according to the determination of *h(k)*, namely, as a positive wavenumber function, we can analyze the domain of validity of (15), and get the intervals for the Ω values:

$$\Omega \in \left[0, \frac{\omega_2}{\sqrt{3}}\right) \cup (\omega_1, \omega_2). \qquad (16)$$

It means that within our model we can expect to observe the DSF peak only in these frequency intervals. Therefore, the physical meaning of the characteristic frequencies ω_1, ω_2 is that they are the bounds for the DSF dispersion value.

b) Phenomenological expression for the collective mode dispersion

In order to satisfy to the above condition, we propose the expression for the collective mode dispersion as a weighted expression of the characteristic frequencies:

$$\Omega = A_{\mathrm{emp}}\omega_1 + (1 - A_{\mathrm{emp}})\omega_2, \qquad (17)$$

where A is a weight (0<A<1). We propose an empirical expression for it:

$$A_{\mathrm{emp}} = 0.008\Gamma^{\frac{3}{2}} + 0.417. \qquad (18)$$

The expression (18) has several conditions of applicability:

1) $q < 2$ (long-wavelength approximation);
2)$\Gamma < 17$ (for the OCP case).

c) Results

The obtained expression for the DSF (14) with Nevanlinna parameter-function (15) was compared with simulation data for Γ = 1,4,5,8,10 and different values of dimensionless wave number (see Fig. 1)

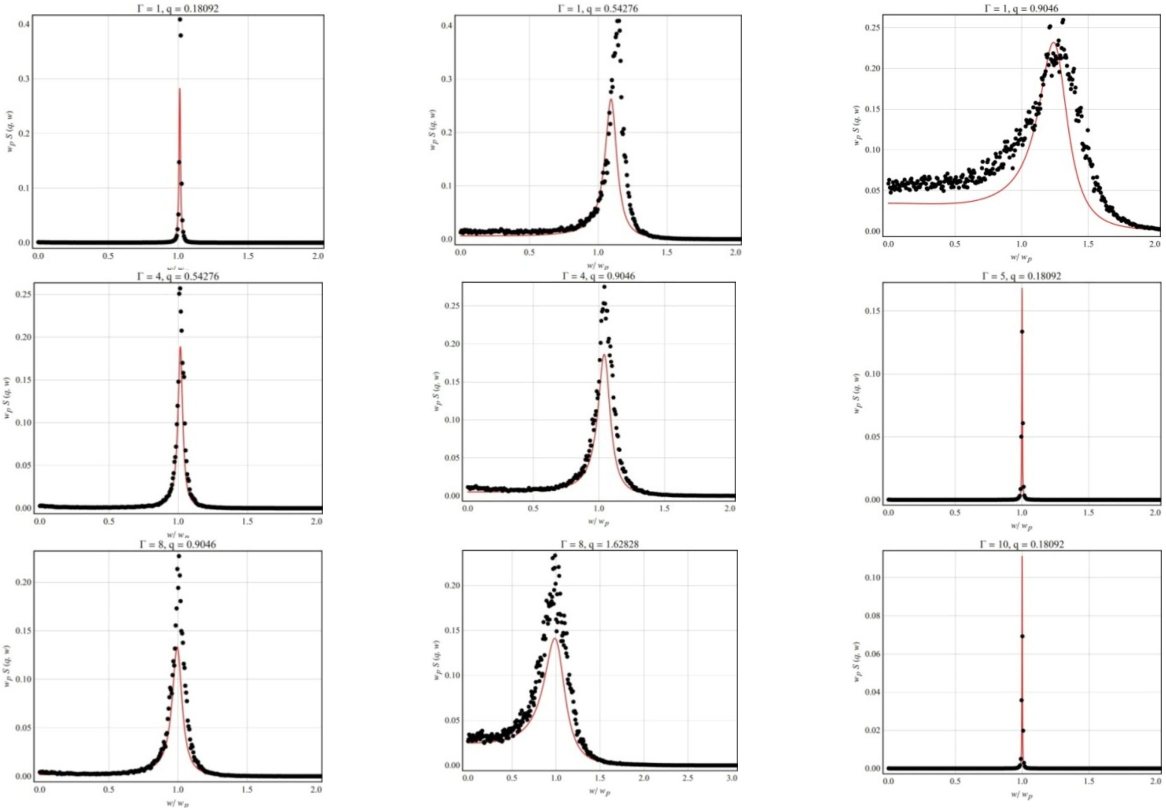

Figure 1 – Comparison between DSF MD data and expression (14) with (15) and (17) for given values of Γ and q

4 Conclusions

The classical method of moments is applied to the investigation of dynamic properties of dense one-component plasmas. A novel approach is suggested to determine the Nevanlinna parameter function. An empirical expression for the collective mode dispersion is found in terms of the characteristics frequencies. The results are in good agreement with the simulation data obtained using the method of molecular dynamics. More information about the method of moments and its application in the plasma physics can be found in [11].

Acknowledgements

The authors acknowledge the support from the state grant numbers 3119/GF4, 3831/ГФ4, funded by the Ministry of Education and Science of the Republic of Kazakhstan.

References

[1] S. Alexander, P. M. Chaikin, P. Grant, G. J. Morales, P. Pines. D. Hone. Charge renormalization, osmotic pressure, and bulk modulus of colloidal crystals: Theory // Chem J. Phys. – 1984. – Vol. 80. – P. 5776-5781.

[2] K. Kremer, M.O. Robbins, G.S. Grest. Phase Diagram of Yukawa Systems: Model for Charge-Stabilized Colloids // Phys. Rev. Lett. – 1986. – Vol. 57. – P. 2694.

[3] S.L. Gilbert, J.J. Bollinger, and D.J. Wineland. Shell-Structure Phase of Magnetically Confined Strongly Coupled Plasmas // Phys. Rev.Lett. – 1988. – Vol. 60. – P. 2022.

[4] M.G. Raizen, J.M. Gilligan, J.C. Bergquist, W.M. Itano, and D.J. Winel and. Ionic crystals in a linear Paul trap // Phys. Rev. A. – 1992. – Vol. 45. – P. 6493.

[5] D.H.E. Dubin, and O'Neill T.M. Trapped nonneutral plasmas, liquids, and crystals (the thermal equilibrium states) // Rev. Mod. Phys. – 1999. – Vol. 71. – P. 87.

[6] V.M. Adamyan, I.M. Tkachenko. Sum rules and exact relations for quantal Coulomb systems // Contrib. PlasmaPhys. – 2003. – Vol. 43. – P. 252-257.

[7] Yu.V. Arkhipov, A. Askaruly, D. Ballester, A.E. Davletov, G.M. Meirkanova, and I.M. Tkachenko Collective and static properties of model two-component plasmas // Phys. Rev. E – 2007. – Vol. 76. –026403.

[8] V.I. Perel, and G.M. Eliashberg, Zh. Eksp. Teor. Fiz. 41, 8861961, Sov. Phys. JETP 14, 633 1962.

[9] N.I. Akhiezer. The Classical Moment Problem Hafner, – NewYork, 1965.

[10] M.G. Krein, and A.A. Nudel'man. The Markov moment problem and extremal problems, Translations of MathematicalMonographs American Mathematical Society, – Providence, RI, – 1977. – Vol. 50.

[11] I.M. Tkachenko, Y.V. Arkhipov, and A. Askaruly. The Method of Moments and its Applications in Plasma Physics. – Germany: Lambert press, 2012. – P. 312.

UDC 533.9

Electrodynamical properties of the dense semiclassical plasmas

K.N. Dzhumagulova*, T.S. Ramazanov, A.K. Baidualiyeva, A. Bakirzhankyzy

Al-Farabi Kazakh National University, IETP, Faculty of physics and technology,
al-Farabi 71, 050040 Almaty, Kazakhstan
**e-mail: dzhumagulova.karlygash@gmail.com*

In this work the dielectric function of the dense semiclassical collisionless plasmas was investigated on the basis of the interaction potential which takes into account the effects of diffraction in a wide range of temperatures and densities. The dielectric function was analytically and numerically investigated in approximation of high frequencies. We obtained the expression for the real part of the dielectric function for collisionless plasma in high – frequency limit within asymptotic approximation. All obtained results are in a good agreement. Taking into account of the diffraction effect in a wide region of temperature and densities can lead to perceptible change in the dielectric function.

Key words: dielectric function, collisionless plasma, interaction potential.
PACS numbers: 52.25.Mq, 52.27.Gr.

1 Introduction

It is well known that the dielectric function plays a key role in description of the electrodynamic plasma properties. Using it one can describe the spectrum of the plasma waves, optical properties as well as many other phenomena [1-3]. In the dense plasmas the influence of the many-body effects and quantum mechanical effects increases. In this case the dielectric function can significantly differ from the dielectric function of the rarefied plasma. To adequately determine the dielectric function it is necessary to know the interaction potential of the plasma particles. Development of the particle interaction models and study of the strongly coupled dense plasmas properties on their basis are of a great fundamental and practical interest [4-9]. To take into account quantum mechanical effects in the interaction potential the special method was developed. It consists of the comparison of the classical Boltzmann's factor and the quantum mechanical Slater sum. This approach was first described in [10]. The Deutsch potential [8,9], which correctly considers the diffraction effect only at high temperatures, has the following form:

$$\Phi_{\alpha\beta}(r)=\frac{Z_\alpha Z_\beta e^2}{r}\left(1-e^{-\frac{r}{\lambda_{\alpha\beta}}}\right). \qquad (1)$$

Here $\lambda_{\alpha\beta}=\hbar/\sqrt{2\pi m_{\alpha\beta}k_B T}$ is the de Broglie thermal wavelength; $m_{\alpha\beta}=m_\alpha m_\beta/(m_\alpha+m_\beta)$ – is the reduced mass of α and β interacted particles. In this work the following dimensionless parameters were used: $\Gamma=Z_\alpha Z_\beta e^2/(a k_B T)$ is the coupling parameter (the average distance between particles is $a=(3/4\pi n)^{1/3}$; $n=n_e+n_i$ is the numerical density of the electrons and ions; T is the plasma temperature; k_B is the Boltzmann constant); $r_s=a/a_B$ is the density parameter ($a_B=\hbar^2/m_e e^2$ is the Bohr radius).

In work [11] the interaction micropotential of the dense semiclassical plasma was obtained on the basis of the method [10] with help of interpolation of the numerical results in a wide region of temperatures and densities:

$$\Phi_{\alpha\beta}(r)=\frac{Z_\alpha Z_\beta e^2}{r}\left(1-than(\sqrt{2}\frac{\lambda\!\!\!^{-}{}^2_{\alpha\beta}}{a^2+br^2})e^{-than(\sqrt{2}\frac{\lambda\!\!\!^{-}{}^2_{\alpha\beta}}{a^2+br^2})}\right)\times\left(1-e^{-r/\lambda\!\!\!^{-}_{\alpha\beta}}\right),\quad b=0.033, \tag{2}$$

where a is the average distance between particles. This micropotential (2) takes into account the quantum diffraction effect in a wide region of temperatures and densities.

Dielectric function $\varepsilon(\omega,k)$ is defined as the value characterizing the magnitude of charge screening in plasma. Dielectric function of the collisionless plasma in high – frequency limit can be presented by the following expression [1]:

$$\varepsilon(k,\omega)=1-\chi_e^0(k,\omega)\tilde{\varphi}_{ee}(k), \tag{3}$$

where $\tilde{\varphi}_{ee}(k)$ is the Fourier transform of the interaction micropotential between the electrons, the response function of the system of non-interacting particles is:

$$\chi_e^0(k,\omega)=-\frac{n_e}{k_BT}W\left(\frac{\omega}{k\mathrm{v}_{Te}}\right), \tag{4}$$

where v_{Te} is the thermal velocity of the electrons, k is a wave vector.

$$W(z)=1-z\exp(-z^2/2)$$
$$\cdot\int_0^z\exp(y^2/2)dy+i\sqrt{\frac{\pi}{2}}z\exp(-z^2/2). \tag{5}$$

Function $W(z)$ in the asymptotic expansion at the high-frequency approximation $\omega/kv_{Te}>>1$ is

$$W(z)=iz\sqrt{\frac{\pi}{2}}\exp\left(-\frac{z^2}{2}\right)-\frac{1}{z^2}-\frac{3}{z^4}-..... \tag{6}$$

2 Tasks and results

In this work the dielectric function of the dense semiclassical plasma was obtained on the basis of the potential (2). For obtaining of analytical expression for the dielectric function the exponents and tangent in the potential (2) were expanded and only the first term, giving the main contribution, was taken into account. The Fourier transform of such simplified form of the interaction potential (2) was deduced analytically and then we obtained the following expression for the real part of the dielectric function for collisionless plasma in high – frequency limit within asymptotic approximation

$$\mathrm{Re}(\varepsilon(k^*,\omega^*))=1-\frac{(k^*)^2}{(\omega^*)^2}\cdot\left(\frac{1}{(k^*)^2+\frac{2\Gamma}{\pi r_s}}+\frac{\pi\frac{2\Gamma}{\pi r_s}}{k^*\sqrt{2b}}-\frac{\pi\left(\frac{2\Gamma}{\pi r_s}\right)^2}{k^*2\sqrt{b}}\left(1+\frac{k^*}{\sqrt{b}}\right)\exp\left(-\frac{k^*}{\sqrt{b}}\right)\right), \tag{7}$$

here dimensionless wave vector and frequency are $\omega^*=\omega/\omega_p$, $k^*=ka$, where $\omega_p=\sqrt{4\pi n_e e^2/m_e}$ is the electron Langmuir frequency. Real part of the dielectric function within the Coulomb potential in this approach is presented by the following expression:

$$\mathrm{Re}(\varepsilon(\omega^*))=1-\frac{1}{(\omega^*)^2}, \tag{8}$$

Real parts of the dielectric functions obtained by formula (7) and also for the Coulomb potential by formula (8), and for the Deutsch potential are shown in Fig. 1, 2. One can see that, the real part of the dielectric function obtained on the basis of the potential (2) (expression (7)) lies above the other curves and tends to the data obtained on the basis of the Deutsch potential at decreasing of the coupling parameter.

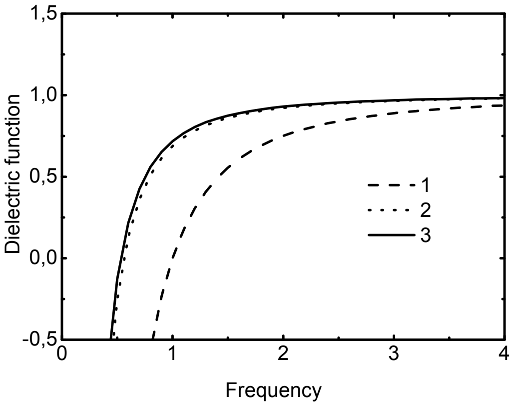

Figure 1 – The real part of the dielectric function obtained on the basis of: 1 – formula (8); 2 – the Deutsch potential; 3 – formula (7). $\Gamma = 0.5$, $ka = 0.1$, $r_s = 5$

For more precise estimation of the dielectric function we used again the equations (3), (4) and (6) but instead of an analytical expression for the Fourier transform of the potential (2), we used numerical method for its calculation. As a result we received data, which agrees qualitatively with the formula (7) (Fig. 3).

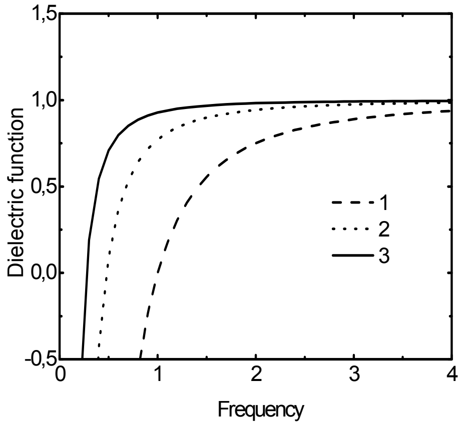

Figure 2 – The real part of the dielectric function obtained on the basis of: 1 – formula (8); 2 – the Deutsch potential; 3 – formula (7). $\Gamma = 1$, $ka = 0.1$, $r_s = 5$

In the third approach we obtained the dielectric function on the basis of the numerically calculated $W(z)$ (eq.(5)). Obtained results are presented on Fig. 4-6.

On fig. 4 and 5 one can see that the curves obtained on the basis of the Deutsch potential and potential (2) are close to each other and differ from result obtained on the basis of the Coulomb potential at increasing of the coupling parameter. Wherein the result on the basis the potential (2) differs stronger than that on the basis of the Deutsch potential. On fig. 6 the dielectric functions obtained on the basis of the potential (2) at different values of the coupling parameter are shown.

Based on all the obtained results one can conclude that taking into account of the diffraction effect in a wide region of temperature and densities can lead to perceptible change in the dielectric function.

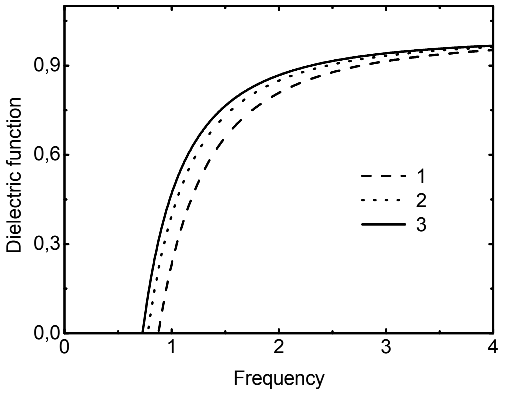

Figure 3 – Numerical calculation of the dielectric function in the asymptotic approximation obtained on the basis of: 1 – formula (8); 2 – the Deutsch potential; 3 – the potential (2). $\Gamma = 0.1$, $ka = 0.1$, $r_s = 5$

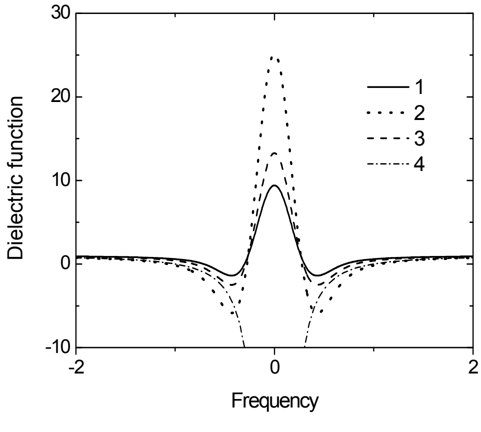

Figure 4 – Dielectric function obtained without asymptotic expansion on the basis of: 1 – the potential (2); 2 – the Coulomb potential; 3 – the Deutsch potential; 4 – formula (8). $\Gamma = 5$, $ka = 0.78$, $r_s = 1$

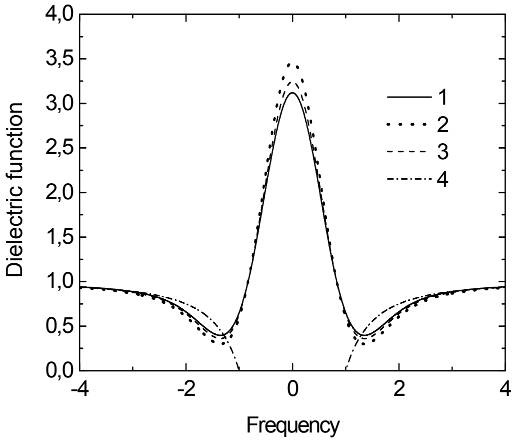

Figure 5 – Dielectric function obtained without asymptotic expansion on the basis of : 1 – the potential (2); 2 – the Coulomb potential; 3 – the Deutsch potential; 4 – formula (8). Γ = 0.5, *ka* = 0.78, r_s = 1

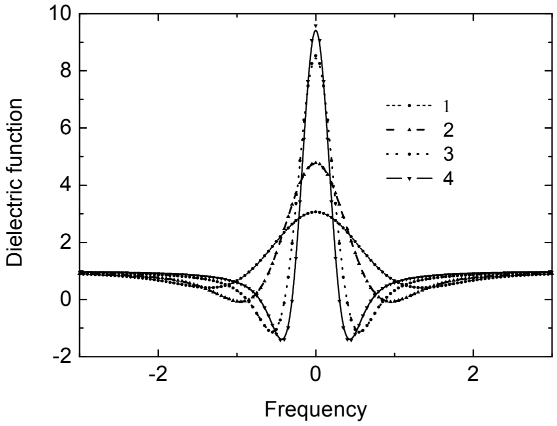

Figure 6 – Dielectric function obtained without asymptotic expansion on the basis of the potential (2) at different coupling parameter, *ka* = 0.78, r_s = 1, 1) Γ = 0.5, 2) Γ = 1, 3) Γ = 3, 4) Γ = 5,

References

[1] S. Ichimaru. Strongly coupled plasmas: high-density classical plasmas and degenerate electron liquids // Rev. Mod. Phys. – 1982. – 54. – P. 1017–1059.

[2] Young-Dae Jung, Woo-Pyo Hong. Electron spin-interaction effects on the ponderomotive magnetization and radiation in degenerate quantum plasmas // Physics of Plasmas. – 2013. – 20. – P. 084502.

[3] W.R. Johnson, C. Guet, G.F. Bertsch. Optical properties of plasmas based on an average-atom model // J. Quant. Spectrosc. Radiat. Transfer. – 2006. – 99. – P. 327–340.

[4] T.S. Ramazanov, K. N. Dzhumagulova. Effective screened potentials of strongly coupled semiclassical plasma // Phys. Plasmas. – 2002. – 9. – P. 3758.

[5] C. Deutsch. Nodal2002 expansion in a real matter plasma // Phys. Letters A. – 1977. – 60 – P. 317.

[6] T.S. Ramazanov, K.N. Dzhumagulova, Y.A. Omarbakiyeva. Effective polarization interaction potentials of the partially ionized dense plasma // J. Phys. A: Math. Gen. – 2006. – 39. – P. 4369.

[7] Young-Dae Jung, Daiji Kato. Quantum effects on the entanglement fidelity in elastic scatterings in strongly coupled semiclassical plasmas// Phys. Plasmas. – 2008. – 15 – P. 104503,

[8] C. Deutsch, M.M. Combert. Diffraction corrections to equilibrium properties of the classical electron gas. Pair correlation function // J. Math. Phys. – 1976. – 17. – P. 1077.

[9] C. Deutsch, Y. Furutani. and M.M. Gombert. Nodal expansions for strongly coupled classical plasmas // Phys. Rep. – 1981. – 69 – P. 85.

[10] A.A. Barker. Effective potential between the components of a hydrogenous plasma // J. Chem. Phys. – 1971. – 55. – P. 1751.

[11] Zh.A. Moldabekov, T.S. Ramazanov, K.N. Dzhumagulova. Pair Interaction Potential of Particles for Two-Component Plasma // Contr. Plasma Phys. – 2012. – 52. – P. 207-210.

UDC539.19; 53.043

Nonrelativistic ionization energy levels of a helium atom

D.T. Aznabayev[1], A.K. Bekbaev[1], I.S. Ishmukhamedov[1], V.I. Korobov[2], A.B. Turmaganbet[1]
[1]Al-Farabi Kazakh National University, IETP, al-Farabi 71, 050040 Almaty, Kazakhstan
[2]Joint Institute for Nuclear Research, 141980 Dubna, Moscow oblast, Russia
e-mail: bekbaev-askhat@mail.ru

The nonrelativistic ionization energy levels of a helium atom are calculated for *S*, *P*, and *D* states. The calculations are based on the variational method of "exponential" expansion. Variational wave functions of bound states were obtained by solving the Schrodinger equation for the quantum three body problem with Coulomb interaction using a variational approach based on exponential expansion with the parameters of exponents being chosen in a pseudorandom way. The convergence of the calculated energy levels is studied as a function of the number of basis functions (*N*). This allows us to claim that the obtained energy values (including the values for the states with a nonzero angular momentum) are accurate to 20 significant digits.

Key words: variational method, expansion, variational principle, Schrödinger equation, inverse iteration method.
PACS numbers: 31.15.-p, 34.50.Fa.

1 Introduction

The quantum problem of three bodies with Coulomb interaction is one of the most notable nonintegrable problems in quantum mechanics. At the same time, extremely accurate numerical solutions for the problem of bound states for a system of three particles may be obtained with modern computers. For example, the nonrelativistic energy of the ground state of helium with a nucleus of an infinite mass is now known accurately to 46 significant digits [1].

In the present study, a version of the variational method (the so-called "exponential" expansion) that renders it possible to numerically solve the quantum Coulomb three-body problem with a very high accuracy and is applicable to, among other things, states with a nonzero angular momentum is considered. This method is used to calculate the nonrelativistic ionization energies of a helium atom for *S*, *P* and *D* states. It is shown that the developed method is an efficient and flexible instrument for investigating Coulomb systems. An analysis of convergence proves that the method is highly accurate and demonstrates that nonrelativistic energy values accurate to 20 significant digits may be obtained easily.

The development of such high-precision methods is also important for the reason that it may help solve a wide variety of physical problems that are of interest in practice. For example, atoms of antiprotonic helium $\mathrm{He}^{+}\bar{p}$ are studied in physics of exotic atoms and molecules [2]. One of the electrons of helium is replaced by an antiproton in this atom. Under certain conditions, this antiproton forms metastable states with a lifetime of several microseconds. Not only is this a record lifetime for an antiparticle within a standard (real) medium, but also an astronomical time by the standards of atomic physics, where the lifetime of the 2*P* state of a hydrogen atom is only 10 ns. This allows one to use precision laser spectroscopy to probe the structure of the spectrum of an antiprotonic helium atom. Another very important aspect, namely, the cross impact of atomic and nuclear physics [3], in the determination of statistical parameters of nuclei should be noted. For example, the accuracy of the mean square helium charge radius that is determined experimentally from electron–nuclei scattering is about 1–3%. At the same time, the experimental determination of the charge radius of $^{4}\mathrm{He}$ by muonic atom spectroscopy allows one to reduce the error in the value of this parameter by more than an order of magnitude.

The paper is structured as follows. The application of the variational method to the stationary Schredinger problem (specifically, the variational "exponential" expansion used in practical calculations) is discussed in detail in Sections 1 and 2. The inverse iteration method, which is considered to be one of the most efficient computational approaches to a discretized problem with a finite basis, is reviewed in Section 3. In the last section, the convergence of numerical calculations is investigated, and the final theoretical results for 11 states of a helium atom are given.

2 Variational method

Let us first formulate the variational principle for bound states and describe the variational method that defines the form of basis functions of the solution expansion and the choice of variational parameters in the construction of wave functions. This method is hereinafter referred to as the "exponential" expansion.

The Hylleraas–Undheim variational principle, which is better known in mathematics as the Rayleigh–Ritz variational principle, is the starting point in solving the stationary Schrödinger equation

$$\mathrm{H}\psi = \mathrm{E}\psi \tag{1}$$

for a certain Hamiltonian using variational methods. This principle is considered a versatile method for deriving an approximate solution. The problems of determining the extrema or stationary values of functionals are the basic problems of variational calculation. The essence of this method consists of substituting the problem of finding the stationary values of functionals with a fundamentally less complex problem of finding the stationary values of functions of several variables [4].

Let there be a self-adjoint operator defined within the Hilbert space for which the following boundedness condition is satisfied:

$$\mathrm{H} \geq \mathrm{cI}, \tag{2}$$

where c is a certain constant. Let us then define a functional

$$\Phi(\psi) = \frac{(\psi, H\psi)}{(\psi,\psi)}, \tag{3}$$

that is bounded from below by c.

Theorem 1 [4]. Let H be a self-adjoint operator that satisfies condition (2). Let us define

$$\mu_n(H) = \max_{\dim \chi = n-1} \min_{\substack{\psi \in D(H) \\ \psi \in \chi^{\perp}}} \Phi(\psi), \tag{4}$$

where $\chi^{\perp}$ is a subspace orthogonal to χ and $\mathcal{D}(H)$ is the domain of operator H. One of the following assertions is then true for any fixed n:

(i) n eigenvalues (degenerate eigenvalues are counted according to their multiplicity) lying below the essential spectrum boundary are present and $\mu_n(H)$ is the n-th eigenvalue (with account of multiplicity);

or

(ii) $\mu_n(H)$ is the lower boundary of the essential spectrum.

The determination of eigenvalues (i.e., the energy of bound states of the stationary Schrödinger equation) comes down to calculating the saddle points of functional (1.4). The assertion of the theorem is known as the minimax principle.

Let us now consider a method that uses the Rayleigh–Ritz variational principle to solve practical eigenvalue problems and is called the Ritz process. Let ϕ_k be a complete sequence of vectors in the Hilbert space subject to the following conditions:

(i) vectors ϕ_k belong to the domain of operator H;

(ii) vectors $\phi_1, \phi_2, ..., \phi_n$ are linearly independent at any n.

Let us assume that $u_n = \sum_{k=1}^{n} x_k \phi_k$ where x_k are scalar coefficients. Inserting u_n (at fixed n) into functional $\Phi(\cdot)$, we obtain a function that depends on a finite set of parameters $\{x_k\}_1^n$:

$$\Phi(\mathbf{x}) = \left(\sum_{i,j=1}^{n} a_{ij} x_i x_j \right) / \left(\sum_{i,j=1}^{n} b_{ij} x_i x_j \right),$$

where

$$a_{ij} = (\phi_i, H\phi_j), \qquad b_{ij} = (\phi_i, \phi_j).$$

The determination of minimax solutions is thus reduced to calculating the corresponding eigenvalues of the generalized eigenvalue problem:

$$A\mathbf{x} = \lambda B\mathbf{x}, \tag{5}$$

where matrices A and B are composed of coefficients a_{ij} and b_{ij}, respectively.

Vectors ϕ_k may depend on nonlinear parameters ω. If this is the case, problem (1.5) is solved for each fixed ω and each eigenvalue number k, $\lambda_k(\omega)$ is chosen, and this value is then minimized by all values of nonlinear parameters:

$$\lambda_k = \inf_{\omega} \lambda_k(\omega).$$

One important condition is satisfied for Ritz estimates

$$\mu_k(H) \le \lambda_k. \qquad (6)$$

It follows from there that Ritz estimates are upper bound ones. Inequality (6) for basis functions dependent on nonlinear parameters follows from

$$\mu_k(H) \le \inf_{\omega} \lambda_k(\omega) = \lambda_k. \qquad (7)$$

A rigorous proof of the applicability of Theorem 1 to the problems of nonrelativistic quantum mechanics with a Hamiltonian of the form

$$H = -\sum_{i=1}^{n} \frac{\Delta_i}{2m_i} + V(r_1,...,r_n),$$

and a potential of a sufficiently general form that includes, among others, the Coulomb potential of interparticle interaction was derived by Kato [5].

3 Generalized Hylleraas expansion

We use the generalized Hylleraas expansion for the states with arbitrary values of total orbital moment *L* of the system:

$$\psi(\mathbf{r}_1,\mathbf{r}_2) = \sum_{l_1+l_2=\mathcal{L}} \mathcal{Y}_{LM}^{l_1 l_2}(\hat{\mathbf{r}}_1,\hat{\mathbf{r}}_2)\, G_{l_1 l_2}^{L\pi}(r_1,r_2,r_{12}),$$
$$G_{l_1 l_2}^{L\pi}(r_1,r_2,r_{12}) = \sum_n C_n e^{-\alpha_n r_1 - \beta_n r_2 - \gamma_n r_{12}}, \qquad (8)$$

where $\mathcal{L} = L$ for the states of "normal" spatial parity $\Pi = (-1)^L$ and $\mathcal{L} = L+1$ for the states of "anomalous" spatial parity $\Pi = (-1)^{L+1}$. The $\mathcal{Y}_{LM}^{l_1 l_2}$ functions are regular bipolar spherical harmonics [6] that depend on two angular coordinates:

$$\mathcal{Y}_{LM}^{l_1 l_2}(\hat{\mathbf{r}}_1,\hat{\mathbf{r}}_2) = r_1^{l_1} r_2^{l_2} \{Y_{l_1}(\hat{\mathbf{r}}_1) \otimes Y_{l_2}(\hat{\mathbf{r}}_2)\}_{LM},$$

and spatial parity operator $P\psi = \pi\psi$ acts on the spatial coordinates in the following way: $P(\mathbf{r}_1,\mathbf{r}_2) \to (-\mathbf{r}_1,-\mathbf{r}_2)$. The ease of use of the $\mathcal{Y}_{LM}^{l_1 l_2}$ functions stems from the fact that they correctly reproduce the behavior of the wave function at $r_1 \to 0$ (or $r_2 \to 0$) and retain the reasonable requirement of boundedness of the function within the region of variation of variables for the expression within square brackets in Eq. (1.8). The "normal" and "anomalous" spatial parities were designated this way for the following reasons. It can be seen from expansion (1.8) that "anomalous" parity states may decompose into clusters with angular momentum of the bound pair $l \ge 1$. In atomic physics, the ground state of a pair of particles has zero angular momentum, while the boundary of the continuous spectrum in a system of three particles is defined by the ground-state energy, the energy of the pair with the lowest energy level, or zero energy (if no bound pairs are present). It follows that bound "anomalous" parity states are located below the threshold of the cluster with the excited pair state and normally lie within the continuous spectrum of a three-particle system. Therefore, after the inclusion of any interaction operator that violates spatial parity into the Hamiltonian, these states blend into the continuous spectrum and form resonances.

The calculation of matrix elements comes down to evaluating integrals of the following form:

$$\Gamma_{lmn}(\alpha,\beta,\gamma) = \int\int r_1^l r_2^m r_{12}^n e^{-\alpha r_1 - \beta r_2 - \gamma r_{12}} dr_1 dr_2 dr_{12}. \qquad (9)$$

Differentiating with respect to αunder the integral sign, we obtain the following:

$$\left(-\frac{\partial}{\partial\alpha}\right)\Gamma_{l-1,mn}(\alpha,\beta,\gamma) = \Gamma_{lmn}(\alpha,\beta,\gamma),$$

thus, all integrals may be evaluated from Γ_{000} by simple differentiation:

$$\Gamma_{lmn}(\alpha,\beta,\gamma)=\left(-\frac{\partial}{\partial\alpha}\right)^{l}\left(-\frac{\partial}{\partial\beta}\right)^{m}\left(-\frac{\partial}{\partial\gamma}\right)^{n}\Gamma_{000}(\alpha,\beta,\gamma)$$
$$=\left(-\frac{\partial}{\partial\alpha}\right)^{l}\left(-\frac{\partial}{\partial\beta}\right)^{m}\left(-\frac{\partial}{\partial\gamma}\right)^{n}\left[\frac{2}{(\alpha+\beta)(\beta+\gamma)(\gamma+\alpha)}\right]. \quad (10)$$

Following [7], we then use recurrence relation

$$\Gamma_{lm}(\alpha,\beta)=\frac{1}{\alpha+\beta}\left[l\Gamma_{l-1,m}+m\Gamma_{l,m-1}+\left(-\frac{\partial}{\partial\alpha}\right)^{l}\left(-\frac{\partial}{\partial\beta}\right)^{m}f(\alpha,\beta)\right]$$

Applying it successively to each pair of variables α,β and γ, we arrive at the recurrence scheme for integral evaluation for nonnegative values of parameters (l,m,n):

$$\Gamma_{lmn}=\frac{1}{\alpha+\beta}[l\Gamma_{l-1,m,n}+m\Gamma_{l,m-1,n}+B_{lmn}],$$
$$B_{lmn}=\frac{1}{\alpha+\gamma}[lB_{l-1,m,n}+mB_{l,m,n-1}+A_{lmn}], \quad (11)$$
$$A_{lmn}=\delta_{l0}\frac{2(m+n)!}{(\beta+\gamma)^{m+n+1}}.$$

The fact that the A_{lmn}, B_{lmn} and Γ_{lmn} values in relations (11) are positive is an important feature of these relations that makes recurrence scheme (11) for integral evaluation resistant to the rounding errors in computer calculations.

The averaging over angular variables for the states with a nonzero total orbital moment of the system was analyzed by Drake [8]. This averaging reduces the calculation of matrix elements to integrals (9). A compact and efficient recurrence scheme that implements this reduction was proposed later by Efros [9].

The efficiency of the above-described variational expansions is the highest when they are applied to systems composed of two electrons and a heavy nucleus. Let us now study this version (“exponential” expansion) in more detail. This expansion assumes the following form for *S* states:

$$\psi(r_1,r_2,r_{12})=\sum_n C_n e^{-\alpha_n r_1-\beta_n r_2-\gamma_n r_{12}} \quad (12)$$

where the parameters in the exponent are chosen in one way or another. In early studies [10] that used expansion (12), the obtained representation was associated with the discretization of the integral representation of the wave function

$$\psi(x_1,\dots,x_A)=\int\varphi(x_1,\dots.x_A;\alpha)f(\alpha)d\alpha \quad (13)$$

that was proposed by Griffin and Wheeler [11] in 1957.The α_n, β_n, and γ_n parameters were chosen in accordance with various quadrature integration formulas(13). The systematic study of expansion (12) with parameters generated using pseudorandom numbers was carried out in [12]. In the proposed approach, nonlinear parameters from Eq. (12) are generated using the following simple formulas:

$$\alpha_n=\left[\left\lfloor\frac{1}{2}n(n+1)\sqrt{p_\alpha}\right\rfloor(A_2-A_1)+A_1\right],$$
$$\beta_n=\left[\left\lfloor\frac{1}{2}n(n+1)\sqrt{p_\beta}\right\rfloor(B_2-B_1)+B_1\right], \quad (14)$$
$$\gamma_n=\left[\left\lfloor\frac{1}{2}n(n+1)\sqrt{p_\gamma}\right\rfloor(C_2-C_1)+C_1\right],$$

where $\lfloor x\rfloor$ is the fractional part of x and p_α, p_β and p_γ are certain prime numbers. These simple generators of pseudorandom numbers have their advantage in there producibility of the results of variational calculations. The convergence rate of the exponential expansion with a pseudorandom strategy for choosing nonlinear parameters (14) is exceptionally high at the sets of basis functions of moderate dimensionalities(up to 100–200 test functions). Rapid basis degeneration that results in the loss of computational stability in the double precision arithmetic by basis dimensionality N = 200 is among the disadvantages of the method. Let us write out for convenience the exponential variational expansion in its complete form with account for the angular dependence of the wave function that describes the rotational degrees of freedom:

$$\psi(\mathbf{r}_1,\mathbf{r}_2) = \sum_{l_1+l_2=\mathcal{L}} \mathcal{Y}_{LM}^{l_1 l_2}(\mathbf{r}_1,\mathbf{r}_2)\, G_{l_1 l_2}^{L\pi}(r_1,r_2,r_{12}),$$

$$G_{l_1 l_2}^{L\pi}(r_1,r_2,r_{12}) = \sum_n C_n e^{-\alpha_n r_1 - \beta_n r_2 - \gamma_n r_{12}}, \qquad (15)$$

where $\mathcal{L} = L$ or $L+1$ (depending on the spatial parity of the state) and the complex parameters in the exponent are generated in a pseudorandom way (14).It was already noted that the convergence rate is reduced when the ground state of a helium atom is calculated. This may be attributed to the fact that the wave function has a logarithmic singularity at $r_1, r_2 \to 0 : \rho^2 \ln \rho$, where $\rho = \sqrt{r_1^2 + r_2^2}$ is the hyper radius of two electrons [13]. In order to remedy the situation, one should construct a multilayer variational expansion composed of several independent sets of basis functions, the optimum variational nonlinear parameters for which are found independently. Thus, each set of basis functions defines the optimum approximation in a certain region of coordinates of the system. In the case of a helium atom, the regions should be enclosed within each other and be more and more compact interms of the hyper radius ($\rho < \rho_n = a^n$, where $a \approx 0.1$ and $n = 1,2,3,\ldots$). This strategy makes the exponential expansion an efficient and versatile solution method for bound states in the quantum three-body problem with Coulomb interaction. The capabilities of this method were demonstrated in [14, 15].

4 Inverse iteration method

It was shown in Section 1 that the stationary Schrödinger equation is reduced to the generalized symmetrical eigenvalue problem with the help of the Ritz procedure:

$$Ax = \lambda Bx, \qquad (16)$$

where A is a symmetric matrix and B is a symmetric positive-definite matrix. The standard diagonalization procedure may be used to solve Eq. (16). In order to do that, matrix $B = L \cdot L^T$ is expanded into a product of upper and lower triangular matrices, and the problem is reduced to the standard symmetrical eigen value problem:

$$A' y = \lambda y \qquad (17)$$

and

$$A' y = L^{-1} A L^{-T}, \quad x = L^T y \qquad (18)$$

However, this method is too laborious ($\sim 20N^3$ multiplication operations) and is less resistant to calculation errors. If only a single eigen value (eigenvector) is needed, the solution may be obtained efficiently ($\sim N^3/6$ multiplication operations) with the help of the inverse iteration method:

$$(A - \mu) x_k^{(n+1)} = s^{(n)} x_k^{(n)} \qquad (19)$$

where scalar factor $s^{(n)}$ is chosen in such a way that $\left\| x_k^{(n+1)} \right\| = 1$. If μ is close to exact eigenvalue λ_k, vector sequence $x_k^{(n)}$ converges rapidly to exact eigenvector x_k, and $\lambda_k^{(n)} = (x_k^{(n)}, A x_k^{(n)})$ converges rapidly to exact value λ_k.

In order to illustrate this, one may assume, without a loss of generality, that matrix A is a diagonal one. The solution may then be written down in the explicit form:

$$x_k^{(n)} = c_n \left(\left(\frac{\lambda_k - \mu}{\lambda_1 - \mu} \right)^n u_1, \ldots, \ldots, \left(\frac{\lambda_k - \mu}{\lambda_n - \mu} \right)^n u_n \right)^T \qquad (20)$$

It can be seen from Eqs. (20) that all components of vector $x_k^{(n)}$ (except for u_k, which remains equal to unity) tend to zero under the given normalization conditions. Practical calculations demonstrate that this method is also the most resistant to rounding errors(calculation errors).

5 Results and discussion

The results of numerical calculations of the ionization energies for *S*, *P*, and *D* states of a helium atom are listed in Table 1. These calculations were carried out using the inverse iteration method. Variational parameters were optimized manually. It should be noted that the optimum variational parameters for different states differ from each other, and the calculation accuracy depends to a considerable extent (5–8 digits)on the choice of the optimum variational parameters for the given bound state. Bases with *N* = 1500, 2000,2500, and 3000 functions were used to optimize the variational parameters. When the states listed in the table were calculated, 3–5 "layers" of basis functions were used.

Program modules of quadruple and sextuple precision (32 and 48 decimal digits, respectively) that were developed by one of the authors of the present paper were used in order to remedy the problem of the numerical instability of calculations at large values of *N*.

The convergence of the nonrelativistic energy value is studied in Tables 2 and 3 as a function of number *N* of basis functions. The difference between two neighboring values (calculated for the last digits given in Tables 2 and 3) is listed in the third column. It is seen clearly that the convergence rate is high. This allows one to obtain highly accurate results.

Table 1 – Nonrelativistic energy levels of S,P and D states of helium atom. N is the number of basis functions

State	Basis (N)	E_{nr}
1^1S	2000	–2.903 724 377 034 119 598 28
1^1S	3000	–2.903 724 377 034 119 598 31
2^1S	2000	–2.145 974 046 054 417 415 77
2^1S	3000	–2.145 974 046 054 417 415 81
2^3S	1500	–2.175 229 378 236 791 305 74
2^3S	2500	–2.175 229 378 236 791 305 74
2^1P	3000	–2.123 843 086 498 101 359 24
2^1P	4000	–2.123 843 086 498 101 359 25
2^3P	3000	–2.133 164 190 779 283 205 11
2^3P	4000	–2.133 164 190 779 283 205 14
3^1S	2500	–2.061 271 989 740 908 650 15
3^1S	300	–2.061 271 989 740 908 650 72
3^3S	2500	–2.068 689 067 472 457 192 00
3^3S	3000	–2.068 689 067 472 457 192 00
3^1P	3000	–2.055 146 362 091 943 536 74
3^1P	4000	–2.055 146 362 091 943 536 89
3^3P	2500	–2.058 081 084 274 275 331 26
3^3P	3500	–2.058 081 084 274 275 331 34
3^1D	3000	–2.055 620 732 852 246 489 39
3^1D	4000	–2.055 620 732 852 246 489 39
3^3D	3000	–2.055 636 309 453 261 327 11
3^3D	4000	–2.055 636 309 453 261 327 11

Table 2 – Investigation of the convergence of the nonrelativistic energy of 1^1S state of helium atom

Basis (N)	E_{nr}	ΔE_{nr}
1600	–2.903 724 377 034 119 597 961	
1800	–2.903 724 377 034 119 598 225	264
2000	–2.903 724 377 034 119 598 282	57
2400	–2.903 724 377 034 119 598 307	25
3000	–2.903 724 377 034 119 598 311	4

Table 3 – Investigation of the convergence of the nonrelativistic energy of 1^1S state of helium atom

Basis (N)	E_{nr}	ΔE_{nr}
2000	–2.123 843 086 498 101 358 687	
2500	–2.123 843 086 498 101 359 180	493
3000	–2.123 843 086 498 101 359 237	57
4000	–2.123 843 086 498 101 359 246	9

6 Conclusions

Variational wave functions of bound states were obtained by solving the Schrodinger equation for the quantum three body problem with Coulomb interaction using a variational approach based on exponential expansion with the parameters of exponents being chosen in a pseudorandom way. The results of calculations of the nonrelativistic energy levels for a helium atom were presented. The numerical calculation results are listed in Table 1. The convergence was studied as a function of the number of test functions. The results of these studies demonstrated that the energy values were accurate to 19–20 significant digits. This accuracy allows one to obtain reliable theoretical predictions.

References

[1] C. Schwartz. Further computations of the He atom ground state // arXiv:math_phys. – 2006. – P. 0605018.

[2] M. Hori, A. Soter, D. Barna, A. Dax, R. Hayano, S. Friedreich, B. Juhasz, Th. Pask, Widmann, D. Horvath, L. Venturelli, and N. Zurlo. Two_photon laser spectroscopy of antiprotonic helium and the antiproton_to_electron mass ratio // Nature. – 2011. – Vol. 475. – P. 484.

[3] J.L. Friar. The structure of light nuclei and its effect on precise atomic measurements // Can. J. Phys. – 2002. – Vol. 80. – P. 1337.

[4] M.C. Reed, B. Simon. Methods of Modern Mathematical Physics. – New York: Academic Press 1978. – Vol. 4. – 325 p. (In Russian: – M.: Mir, 1982)

[5] T. Kato. Fundamental properties of Hamiltonian operators of Schrodinger type // Trans. Am. Math. Soc. – 1951. – Vol. 70. – P. 195.

[6] D.A. Varshalovich, A.N. Moskalev, and V.K. Khersonskii. Quantum Theory of Angular Momentum.– Singapore: World Sci., 1988. – P. 526. (In Russian:– Leningrad: Nauka, 1975).

[7] R.A. Sack, C.C.J. Roothaan, W. Kolos. Recursive evaluation of some atomic integrals // J. Math. Phys. A. – 1967. – Vol. 8. – P. 1093.

[8] G.W.F. Drake. Angular integrals and radial recurrence relations for two-electron matrix elements in Hylleraas coordinates // Phys. Rev. A.– 1978. – Vol. 18. – P. 820.

[9] V.D. Efros. The three-body problem: generalized exponential expansion; arbitrary states in a correlated basis, and the binding energy of muonic molecules // Sov. Phys. JETP. – 1986. – Vol. 63. – P. 5.

[10] C.M. Rosenthal. The reduction of the multidimensional Schrödinger equation to a one-dimensional integral equation // Chem. Phys. Lett. – 1971. – Vol. 10. – P. 381-386.

[11] J.J. Griffin, J.A. Wheeler. Collective motions in nuclei by the method of generator coordinates // Phys. Rev. – 1957. – Vol. 108. – P. 311.

[12] A.J. Thakkar, V.H. Smith. Compact and accurate integral-transform wave functions. The 11*S* state of the helium-like ions from H^- through Mg^{10+} // Phys. Rev. A – 1977. – Vol. 15. – P. 1.

[13] J.H. Bartlett. The helium wave equation // Phys. Rev. – 1937. – Vol. 51. – P. 661.

[14] V.A. Fok. On Schrödinger equation for helium atom // Izv. Akad. Nauk SSSR, Fiz. – 1954. – Vol. 18. –P. 161.

[15] V.I. Korobov. Coulomb three-body bound-state problem: variational calculations of nonrelatistic energies // Phys. Rev. A. – 2000. – Vol. 61. – P. 064503.

[16] V.I. Korobov. Nonrelativistic ionization energy for the helium ground state // Phys. Rev. A. – 2002. – Vol. 66. – P. 024501.

UDC 524.3; 524.1;52-1/-8:530.12; 524.8

Non-rotating and slowly rotating white dwarfs in classical physics

K. Boshkayev[1,2*], J.A. Rueda[2], R. Ruffini[2], B. Zhami [1], Zh. Kalymova[1], G. Balgimbekov[1]

[1]*Al-Farabi Kazakh National University, IETP, al-Farabi 71, 050040 Almaty, Kazakhstan*

[2]*Dipartimento di Fisica and ICRA, Università di Roma "La Sapienza", Piazzale Aldo Moro 5, I-00185 Roma, Italy*

[*]*e-mail: kuantay@mail.ru*

The equilibrium configurations of uniformly rotating white dwarfs are calculated in the framework of classical physics. The Chandrasekhar and the Salpeter equations of state are used to describe the white dwarf matter. The Hartle formalism is applied to the integration of the equations of hydrostatic equilibrium and field equations. The equations of structure have been expanded in powers of the angular velocity Ω of the white dwarf, and terms of higher order than Ω^2 have been neglected.All parameters of rotating white dwarfs such as the total mass, polar and equatorial radii, eccentricity, moment of inertia, angular velocity, angular momentum, gravitational potential and quadrupole moment have been calculated numerically within this approximation.

Key words: white dwarfs, uniform rotation, Hartle's formalism, equilibrium configurations, moment of inertia, quadrupole moment.
PACS numbers: 97.10.Cv, 97.10.Kc, 97.10.Nf, 97.10.Pg, 97.20.Rp.

1 Introduction

In order to investigate the equilibrium structure of non-rotating and rotating white dwarfs in the Newtonian physics a number of authors have calculated in greater detail the classical equilibrium configurations of cold white dwarfs [1, 2]. In the literature among all those approaches the Hartle formalism in the classical case has been neglected, probably due to its relativistic counterpart, which is widely used in the scientific community to describe relativistic objects such as neutron stars, quark stars, and other exotic objects [3-5].

In our recent work [6] we have revisited the Hartle formalism in the classical case, giving detailed derivations of all the physical quantities such as the total rotating mass, the equatorial and polar radii, eccentricity, moment of inertia both for non-rotating and rotating configurations, and quadrupole moment. All these parameters play a pivotal rolein the investigation of the stability and the lifespan of white dwarfs, main sequence stars and giant stars[7-9].

In this work we investigate the effects of angular velocity on the structure of white dwarfs. We examine the case of white dwarfs which rotate rigidly and slowly. We integrate the equations of structure for slowly rotating white dwarfs numerically for the Chandrasekhar and Salpeter equations of state [10, 11].

2 Equation of structure

The method used to construct models for uniformly and slowly rotating stars is summarized briefly here [3, 6].

Equation of state.

As the first step in the calculation of a slowly rotating stellar model, one-parameter equation of state, $p = p(\rho)$, is specified. Here p is the pressure, ρ is the matter density. For white dwarfs this relation will be one of the equations of state summarized in [11-14].

Non rotating white dwarfs.

For a given value of the central density, the non-rotating equilibrium configuration is determined by integrating the Newtonian equation of hydrostatic equilibrium for the pressure, $p^{(0)}(R)$, and the mass interior to a given radius, $M^{(0)}(R)$:

$$\begin{cases} \frac{dp^{(0)}(R)}{dR} = -\rho(R)\frac{GM^{(0)}(R)}{R^2}, \\ \frac{dM^{(0)}(R)}{dR} = 4\pi R^2 \rho(R). \end{cases} \quad (1)$$

The integration is performed outward, starting at the star's center, $R = 0$. At the star's center $M^{(0)}(R=0) = 0$; $\rho(R=0) = \rho_c$ is the given central density; and $p^{(0)}$ is $p^{(0)}(\rho_c)$ as given by the equation of state. The radius of the spherical surface of the star, a, is that value of R at which $p^{(0)}(R)$ drops to zero; and the value of$M^{(0)}(R)$ there is the star's total static mass.

The gravitational potential of a non-rotating star is determined by integrating outward from the center the equation

$$\frac{d\Phi^{(0)}(R)}{dR} = \frac{GM^{(0)}(R)}{R^2} = -\frac{1}{\rho(R)}\frac{dp^{(0)}(R)}{dR} \qquad (2)$$

with the boundary condition$\Phi^{(0)}(\infty) = 0$.

The moment of inertia of a spherical star is calculated easily from the following expression:

$$I^{(0)}(a) = \frac{8\pi}{3}\int_0^a \rho(R)R^4 dR. \qquad (3)$$

Values for the central density and angular velocity.

Once the equation of state is specified, there is a unique equilibrium configuration for each choice of the central density and angular velocity. The small perturbations away from a non-rotating equilibrium configuration are all proportional to the angular velocity or to its square. Consequently, for a given central density, all the models of different angular velocities can be obtained from a single model by applying an appropriate scaling. In this paper the results are given in graphical form for the angular velocity Ω satisfying

$$\Omega = \sqrt{\frac{GM_{tot}}{R_e^3}}, \qquad (4)$$

where G is the gravitational constant, M_{tot} is the total mass of the rotating configuration andR_e is its equatorial radius. This is the critical angular velocity at which mass-shedding will occur, and it is thus a natural upper bound on those angular velocities for which the assumption of slow rotation could be valid. Knowing the values of moment of inertia $I^{(0)}$ and the angular velocity Ω one can determine the angular moment of a spherical star by

$$J = I^{(0)}(a)\Omega. \qquad (5)$$

Having chosen a value of the angular velocity for each value of the central density, one constructs a sequence of equilibrium models by integrating the Newtonian equations of structure for a sequence of central densities.

The spherical deformation of the star.

The spherical part of the rotational deformation is calculated by integrating the$l = 0$equations of hydrostatic equilibrium for the "change in mass" $M^{(2)}(R)$ and the "pressure perturbation function" $p_0^*(R)$:

$$\begin{cases} \dfrac{dp_0^*(R)}{dR} = \dfrac{2}{3}\Omega^2 R - \dfrac{GM^{(2)}(R)}{R^2} \\ \dfrac{dM^{(2)}(R)}{dR} = 4\pi R^2\rho(R)\dfrac{d\rho(R)}{dR}p_0^*(R), \end{cases} , \qquad (6)$$

These equations are integrated out from the origin with boundary conditions that as $R \to 0$

$$p_0^*(R) \to \frac{1}{3}\Omega^2 R^2,\ M^{(2)}(R) \to 0. \qquad (7)$$

These boundary conditions guarantee that the central densities of the rotating and non-rotating configurations are the same. Consequently, the total mass of the star with central density ρ_c and angular velocity Ω is

$$M_{tot} = M^{(0)}(a) + M^{(2)}(a), \qquad (8)$$

where a is the radius of the spherical configuration.

The quadrupole deformation of the star.

One calculates the quadrupole part of the deformations by integrating the $l = 2$ equations. Firstly, one needs to findparticular solution by integrating equations

$$\begin{cases} \dfrac{d\chi(R)}{dR} = -\dfrac{2GM(R)}{R^2}\varphi(R) + \dfrac{8\pi}{3}\Omega^2 R^3 G\rho(R) \\ \dfrac{d\varphi(R)}{dR} = \left(\dfrac{4\pi R^2\rho(R)}{M(R)} - \dfrac{2}{R}\right)\varphi(R) - \dfrac{2\chi(R)}{GM(R)} + \dfrac{4\pi}{3M(R)}\rho\Omega^2 R^4 \end{cases} \qquad (9)$$

outward from the center with arbitrary initial conditions satisfying equations

$$\begin{gathered}\varphi(R) \to AR^2,\\ \chi(R) \to BR^4,\\ B + \tfrac{2\pi}{3} G\rho_c A = \tfrac{2\pi}{3} G\rho_c \Omega^2, \end{gathered} \tag{10}$$

where A and B are arbitrary constants. Set, for example, $A = 1$ and define B from the above algebraic equation. This determines particular solutions $\varphi_p(R)$ and $\chi_p(R)$.

Secondly, the homogeneous solution should be considered by integrating the homogeneous equations

$$\begin{cases} \dfrac{d\chi_h(R)}{dR} = -\dfrac{2GM(R)}{R^2}\varphi_h(R) \\ \dfrac{d\varphi_h(R)}{dR} = \left(\dfrac{4\pi R^2 \rho(R)}{M(R)} - \dfrac{2}{R}\right)\varphi_h(R) - \dfrac{2\chi_h(R)}{GM(R)} \end{cases} \tag{11}$$

outward from the center with arbitrary initial conditions satisfying the equations

$$\begin{gathered}\varphi_h(R) \to AR^2,\\ \chi_h(R) \to BR^4,\\ B + \tfrac{2\pi}{3} G\rho_c A = 0 \end{gathered} \tag{12}$$

Set $A = 1$ and B is given by the above equation. This determines particular solutions $\varphi_h(R)$ and $\chi_h(R)$. Thus interior solution is determined by the sum of the particular and the homogeneous solution

$$\begin{gathered}\varphi_{in}(R) = \varphi_p(R) + K_2\varphi_h(R),\\ \chi_{in}(R) = \chi_p(R) + K_2\chi_h(R).\end{gathered} \tag{13}$$

Matching with the Exterior Solutions.

The exterior solutions are given by

$$\varphi_{ex}(R) = \frac{K_1}{R^3}, \quad \chi_{ex}(R) = \frac{K_1 G M^{(0)}}{2R^4}. \tag{14}$$

By matching (13) and (14) at $(R = a)$

$$\begin{gathered}\varphi_{ex}(R = a) = \varphi_{in}(R = a),\\ \chi_{ex}(R = a) = \chi_{in}(R = a).\end{gathered} \tag{15}$$

constants K_1 and K_2 are determined.

The polar and equatorial radii and eccentricity.

The surface of the rotating configuration, polar R_p and equatorial R_e radii are given by

$$r(a,\Theta) = a + \xi_0(a) + \xi_2(a)P_2(\Theta), \tag{16}$$

$$R_p = r(a,0) = a + \xi_0(a) + \xi_2(a), \tag{17}$$

$$R_e = r(a,\pi/2) = a + \xi_0(a) - \xi_2(a)/2, \tag{18}$$

where $\xi_0(a)$ and $\xi_2(a)$ are given by

$$\xi_0(R) = \frac{R^2}{GM^{(0)}(R)} p_0^*(R), \tag{19}$$

$$\xi_2(R) = -\frac{R^2}{GM^{(0)}(R)}\left\{\frac{1}{3}\Omega^2 R^2 + \varphi_{in}(R)\right\}. \tag{20}$$

The eccentricity is defined by

$$\text{eccentricity} = \sqrt{1 - \left(\frac{R_p}{R_e}\right)^2}. \tag{21}$$

Quadrupole moment.

The Newtonian potential $\Phi(R,\Theta)$ outside the star $(R > a)$is given by

$$\Phi(R,\Theta) = -\frac{GM_{tot}}{R} + \frac{K_1}{R^3} P_2(\cos\Theta), \tag{22}$$

thus the constant K_1 can be written as $K_1 = GQ$, where Q is the mass quadrupole moment of the star. According to Hartle's definition $Q > 0$ defines an oblate object, $Q < 0$ defines a prolate object.

Total moment of inertia and total angular momentum.

The total moment of inertia of a rotating configuration is determined as the sum of the moment of inertia of a static star and the change in the moment of inertia due to rotation and deformation

$$I_{tot}(R) = I^{(0)}(R) + I^{(2)}(R), \tag{23}$$

where the moment of inertia of the non-rotating star is determined as earlier

$$I^{(0)}(R) = \frac{8\pi}{3}\int_0^R \rho(R) R^4 dR, \tag{24}$$

and its change due to rotation is given by [15]

$$I^{(2)}(R)=\frac{8\pi}{3}\int_0^R \rho(R)R^4\left(\frac{d\xi_0(R)}{dR}-\frac{1}{5}\frac{d\xi_2(R)}{dR}+\frac{4}{R}\left[\xi_0(R)-\frac{1}{5}\xi_2(R)\right]\right)dR$$
$$=\frac{8\pi}{3}\int_0^R\left(\left[\frac{1}{5}\xi_2(R)-\xi_0(R)\right]\frac{d\rho(R)}{dR}\right)R^4dR \tag{25}$$

From here the total angular momentum of a rotating configuration will be determined by

$$J_{tot}=I_{tot}(a)\Omega. \tag{26}$$

Thus, we have all the necessary equation to investigate equilibrium configurations of classical white dwarfs.

3 Results and discussion

In equilibrium, a rotating star attains a balance between pressure forces, gravitational forces, and centrifugal forces. In classical physics the magnitude of the centrifugal force is determined by the angular velocity Ω of the fluid relative to a distant observer. In the literature angular velocityΩgiven by (4) is usually known as mass-shedding or Keplerian angular velocity.

In Fig. 1 the mass of a white dwarf is shown as a function of the central density. The mass is given in the units of one solar mass and the central density is given in grams per centimeter cube. We have selected two equations of state: the Chandrasekhar equation of state with average molecular weight $\mu=2$, and the Salpeter equation of state for carbon and iron white dwarfs as a limiting case. All solid curves indicate non-rotating (static) white dwarfs, whereas all dashed curves indicate rotating white dwarfs at the mass-shedding rate. As it has been expected rotating white dwarfs have larger masses with respect to their static counterparts. In all our computations we restricted the values of the central density to the values of inverse beta decay density to fulfill the stability condition of white dwarfs [14]. In classic white dwarfs the maximum (threshold) value of the central density is considered to be the minimum value between the density for the onset of inverse-beta decay process[13,16].

Figure 2 shows mass and equatorial radius relation. The equatorial radius reduces to the static radius in the non-rotating limit. All legends in the plot are the same as in Fig. 1. Depending on the equation of state and chemical composition, white dwarfs display different mass-radius relation. This explains the variety of observed white dwarfs. Nowadays, we have data for 9316 white dwarfs and all of them have diverse characteristics [17, 18].

Figure 3 illustrates normalized moment of inertia as a function of the central density. The legends are the same as in Fig.1. The lower the density the larger the difference in the moment of inertia of rotating and static white dwarfs.

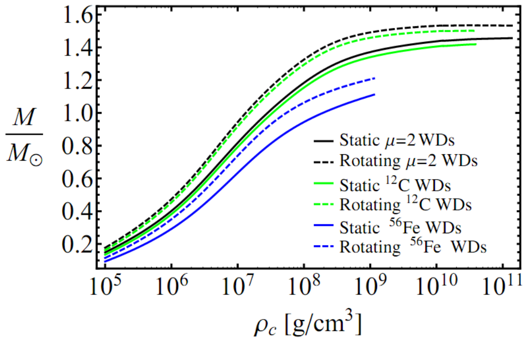

Figure 1 – Mass versus central density
(see the color version on the web)

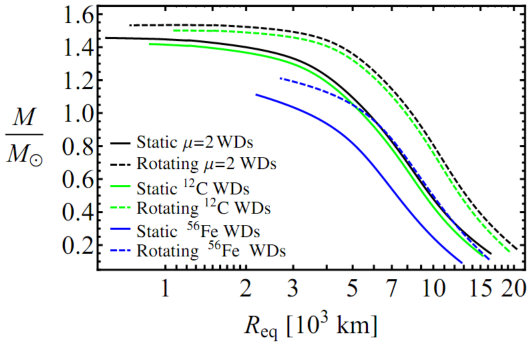

Figure 2 – Mass versus equatorial radius
(see the color version on the web)

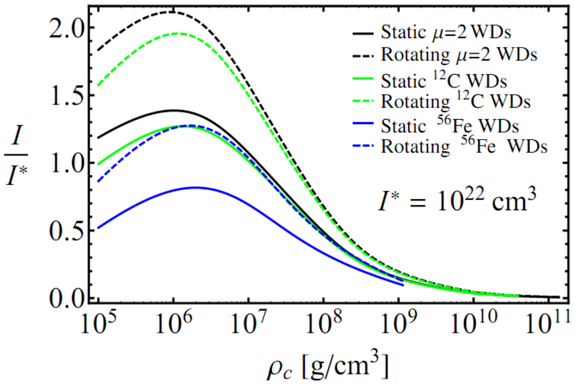

Figure 3 – Moment of inertia versus central density

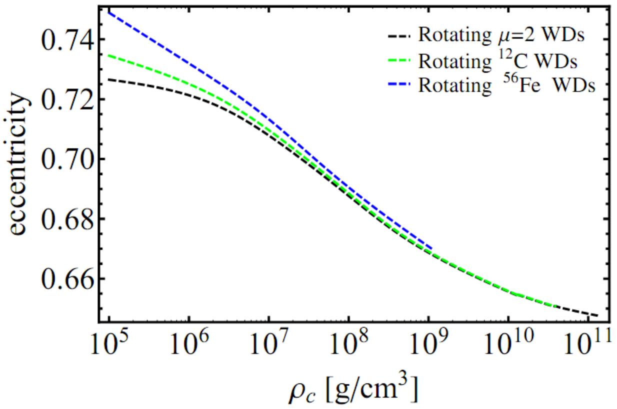

Figure 4 – Eccentricity versus central density

The eccentricity of rotating white dwarfs as a function of central density is shown in Fig. 4. For higher densities the eccentricity decreases and vice versa. Thus, white dwarfs in this case become more spherical as they approach their maximum mass.

The normalized mass quadrupole moment versus eccentricity is represented in Fig. 5. The legends are the same as in Fig. 1. Here one can see that for larger densities the eccentricity and quadrupole moment are correlated. The quadrupole moment decreases as well with increasing density. The system becomes more gravitationally bound.

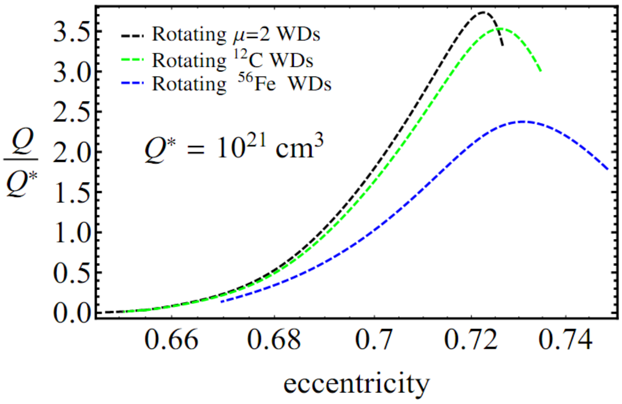

Figure 5 – Quadrupole moment versus eccentricity

4 Conclusion

The equations have been numerically integrated in order to calculate the structure of slowly rotating classical white dwarfs in hydrostatic equilibrium. In particular, the relation between mass and central density, the shapes of rotating stars have been calculated for the Chandrasekhar and Salpeter equations of state.

The equations which determine the moment of inertia and the quadrupole moment of the rotating star have also been integrated numerically. The product of the moment of inertia and the angular velocity determines the angular momentum of a star.

All these quantities play a fundamental role in describing the equilibrium configurations of uniformly rotating main sequence stars as well as planets. The results obtained in the work are in agreement with other work in the literature related to the rigidly rotating white dwarfs in the Newtonian physics [19-20].

Acknowledgements

This work was supported in part by grants No. 3101/GF4and F.0679 of the MES RK.

References

[1] V.S. Geroyannis, P.J. Papasotiriou. Spin-up and Spin-down of Rotating Magnetic White Dwarfs: A Straightforward Numerical Approach // ApJ. – 2000. – Vol. 534. – P. 359-366.

[2] S.L. Shapiro, S.A. Teukolsky. Black holes, white dwarfs, and neutron stars: The physics of compact objects. – New York: Wiley-Interscience, 1983. – P. 672.

[3] J.B. Hartle. Slowly Rotating Relativistic Stars. I. Equations of Structure // ApJ. – 1967. – Vol. 150. – P. 1005.

[4] J.B. Hartle, K.S. Thorne. Slowly Rotating Relativistic Stars. II. Models for Neutron Stars and Supermassive Stars // ApJ. – 1968. – Vol. 153. – P. 807.

[5] N. Stergioulas. Rotating Stars in Relativity // Living Rev. Relativity. – 2003. – Vol. 6. – P. 3.

[6] K. Boshkayev. Non-rotating and slowly rotating stars in classical physics // International Journal of mathematics and physics. – 2014. – Vol. 5. – № 1. – P. 69-80.

[7] G. Meynet, A. Maeder. Stellar evolution with rotation. V. Changes in all the outputs of massive star models // A&A. – 2000. – Vol.361. – P.101-120.

[8] G. Meynet, A. Maeder.Stellar evolution with rotation. X. Wolf-Rayet star populations at solar metallicity // A&A. – 2003. – Vol. 404. – P. 975-990.

[9] S. Ekstrom, G. Meynet, C. Chiappini, R. Hirschi, A. Maeder. Effects of rotation on the evolution of primordial stars // A&A. – 2008. – Vol. 489. – P. 685-698.

[10] S. Chandrasekhar. The Maximum Mass of Ideal White Dwarfs // ApJ. – 1931. – Vol. 74. – P. 81-82.

[11] E.E. Salpeter. Energy and Pressure of a Zero-Temperature Plasma // ApJ. – 1961. – Vol. 134. – P. 669.

[12] S. Chandrasekhar. Introduction to the Study of Stellar Structure. – Chicago: University of Chicago Press, 1939.

[13] M. Rotondo, J.A. Rueda, R. Ruffini, Xue S.-S. Relativistic Thomas-Fermi treatment of compressed atoms and compressed nuclear matter cores of stellar dimensions // Phys. Rev. C. – 2011. – Vol. 83. – P. 045805.

[14] M. Rotondo, J.A. Rueda, R. Ruffini, Xue S.-S. Relativistic Feynman-Metropolis-Teller theory for white dwarfs in general relativity // Phys. Rev. D. – 2011. – Vol. 84. – P. 084007.

[15] J.B. Hartle. Slowly Rotating Relativistic Stars. IX: Moments of Inertia of Rotationally Distorted Stars // Astrophysics and Space Science. – 1973. – Vol. 24. – P. 385-405.

[16] K. Boshkayev, J. Rueda, R. Ruffini, I. Siutsou. On General Relativistic Uniformly Rotating White Dwarfs // ApJ. – 2013. – Vol. 762. – P. 117.

[17] S.O. Kepler, S.J. Kleinman, A. Nitta, D. Koester, B.G. Castanheira, O. Giovannini, A.F.M. Costa, L Althaus. White dwarf mass distribution in the SDSS // Mon. Not. R. Astron. Soc. – 2007. – Vol. 375. – P. 1315-1324.

[18] P.E. Tremblay, P. Bergeron, and A. Gianninas. An Improved Spectroscopic Analysis of Da White Dwarfs from the Sloan Digital Sky Survey Data Release 4 // ApJ. – 2011. – Vol. 730. – P. 128.

[19] K. Boshkayev, J. Rueda, R. Ruffini. On the Maximum Mass of General Relativistic Uniformly Rotating White Dwarfs // International Journal of Modern Physics E. – 2011. – Vol. 20. – P. 136-140.

[20] Boshkayev K., Rueda J., Ruffini R., Siutsou I. General Relativistic and Newtonian White Dwarfs // Proceedings of the MG13 Meeting on General Relativity (in 3 Volumes) /ed. by Rosquist K. *et al.* – World Scientific Publishing Co. Pte. Ltd. 2015. – P. 2468-2474.